Transport processes regulating lowermost stratospheric ozone and their year-to-year variability

Frederik Harzer



München 2025

Transport processes regulating lowermost stratospheric ozone and their year-to-year variability

Frederik Harzer

Dissertation

der Fakultät für Physik

der Ludwig-Maximilians-Universität

München

vorgelegt von
Frederik Harzer
aus Bad Friedrichshall

Erstgutachter: Prof. Dr. Thomas Birner

Zweitgutachterin: PD Dr. Hella Garny

Tag der mündlichen Prüfung: 19. September 2025

Zusammenfassung

Die vorliegende Arbeit betrachtet die für atmosphärisches Ozon in der untersten Stratosphäre (engl. "lowermost stratosphere", "LMS") relevanten Transportprozesse. Die LMS markiert hierbei den Bereich zwischen der oberen Troposphäre und der unteren Stratosphäre in den Extratropen. Sie wird nach unten hin durch die Tropopause begrenzt und sowohl durch die troposphärische Dynamik als auch von der großräumigen stratosphärischen Zirkulation, insbesondere von der Brewer-Dobson-Zirkulation, stark beeinflusst. Mittels Reanalysen und Satelliten-Beobachtungsdaten werden zunächst die primären dynamischen Ursachen der Ozonvariabilität in der extratropischen Stratosphäre sowie deren Einfluss auf Ozon in der LMS untersucht. Der Schwerpunkt dieser Studie liegt auf der jährlichen Kovariablität von Ozon mit der Stärke des stratosphärischen Polarwirbels zur Winterzeit auf der nördlichen Hemisphäre. Das resultierende Muster der Ozonvariabilität weist robuste und komplexe Strukturen als Funktion von geographischer Breite und Druck auf. Ein Vergleich mit isentropen Koordinaten und die Analyse des Ozonbudgets zeigen, dass dieses Muster durch Kombination von adiabatischer Kovariabilität der Tropopause, meridionalen Eddy-Mischungsprozessen und sowohl adiabatischer als auch diabatischer Vertikaladvektion erklärt werden kann.

Eine zweite Studie befasst sich mit der charakteristischen Struktur der Ozonverteilung in der subtropischen LMS. Basierend auf den lokalen Ozon-Hintergrundgradienten werden Zirkulationsmetriken konstruiert, die mit der Stärke oder der meridionalen Position des subtropischen Jetstreams auf beiden Hemisphären zur Winterzeit korrelieren. Mithilfe dieser Metriken werden anschließend langjährige Trends der subtropischen Jetstreams aus Reanalysen, Ozon-Beobachtungsdaten und Chemie-Klimamodellen abgeleitet.

Zuletzt folgt eine detaillierte Analyse des Ozonbudgets der LMS der Nordhalbkugel in isentropen Koordinaten, um adiabatische und diabatische Transportbeiträge zu quantifizieren. Neben den primären Beiträgen durch diabatische Advektion und meridionale Mischungsprozesse wird die Bedeutung der Horizontaladvektion und des vertikalen Eddy-Transports beleuchtet. Letzterer ist insbesondere in der Tropopausenregion relevant, verstärkt dort teils die vertikalen Ozongradienten im Wesentlichen aufgrund langwelliger Strahlungsdämpfung und beeinflusst damit schließlich den meridionalen, diffusiven Eddy-Transport.

Summary

In this thesis, aspects of the transport processes regulating atmospheric ozone in the lowermost stratosphere (LMS) are considered, focusing on winter-mean climatologies and interannual variability. The LMS represents the intermediate domain between the upper troposphere and the lower stratosphere in the extratropics. It is bounded below by the tropopause and is strongly influenced by both tropospheric dynamics as well as by the large-scale stratospheric circulation, i. e., the Brewer-Dobson circulation.

First, using different reanalysis products and satellite observations, the dominant dynamical drivers of ozone variability in the extratropical stratosphere and their impact on LMS ozone are investigated. This study focuses on year-by-year, winter-mean ozone covariability associated with changes of the strength of the stratospheric polar vortex in the Northern Hemisphere. The resulting ozone response pattern shows robust and complex structures in the latitude-pressure plane. The comparison with an isentropic coordinate framework and results from an ozone budget analysis reveal that this response signature can be explained by a combination of strong adiabatic tropopause co-variability, horizontal eddy mixing as well as mean-flow vertical advection with both substantial adiabatic and diabatic contributions.

The second study refers to the characteristic structure of the LMS ozone distribution in the subtropics. Here, different circulation metrics are constructed based on the local ozone background gradients and are shown to strongly co-vary with either the strength or the latitudinal position of the subtropical jet stream for both hemispheres during winter. These ozone gradient metrics are then applied to observational total-column ozone data, constraining historical jet trends from reanalyses, and to chemistry-climate models.

Finally, a detailed analysis of the northern hemispheric LMS ozone budget in isentropic coordinates is conducted to distinguish adiabatic and diabatic transport processes. Besides the dominant contributions by diabatic downwelling and quasi-horizontal eddy mixing, horizontal advection and vertical eddy transport are also found to be relevant. The latter is shown to contribute substantially in the tropopause region, where up-gradient vertical eddy transport, mostly associated with long-wave radiative damping, partly strengthens the vertical ozone gradients and therefore impacts meridional, diffusive eddy mixing.

Contents

Zι	ısammenfassung	5
Sı	ımmary	7
1	Introduction 1.1 Prologue	13
2	Paper I	17
3	Paper II	35
4	Paper III	55
5	Discussion	79
\mathbf{R}	eferences	89
A	cknowledgments	95

Chapter 1

Introduction

1.1 Prologue

Ozone? – It sounds like a good idea to get to know the protagonist of this story before diving deeper into atmospheric science. Doing so, your first step could lead you to the World Meteorological Organization (WMO) to check out some basics:

"Ozone is a gas that is naturally present in our atmosphere. Ozone has the chemical formula O_3 because an ozone molecule contains three oxygen atoms [...]. The word ozone is derived from the Greek word $\delta \zeta \epsilon i \nu$ (ozein), meaning 'to smell.'" (Salawitch et al., 2023, p. 4)

Next, you may skim through some of ozone's specific properties and study the relevant safety recommendations, listed, e.g., in the GESTIS database by the Institute for Occupational Safety and Health (IFA):

```
"[...]

Properties

Gas, not commercially available in compressed gas cylinders colourless
in liquid state dark blue
disagreeably pungent odour, in higher concentrations like chlorine
[...]

Chemical characterisation
Oxidizing gas. [...]

Highly explosive in liquid and solid form.
Only slightly soluble in water.
Gas is heavier than air.
Chemically unstable.
[...]
```

1. Introduction

Physical and chemical properties [...]

```
Melting point: -192.5 °C [...]
Boiling point: -111.9 °C
```

[...]

Hazardous reactions [...]

Ozone is not stable and decomposes to oxygen. Its half-life is 20 to 100 hours at room temperature and just seconds at 300 °C. [...]" (IFA, 2025, slightly adapted)

Indeed, this sounds interesting, but lab experiments with ozone could be quite challenging under these conditions. You may therefore rather be interested to learn a bit more about history – your search engine likely will quickly point you to the famous "Montreal Protocol on Substances that Deplete the Ozone Layer" (UNEP, 2019), which was adopted on September 16, 1987 by the members of the United Nations,

"(m)indful of their obligation under that Convention to take appropriate measures to protect human health and the environment against adverse effects resulting or likely to result from human activities which modify or are likely to modify the ozone layer [...]" (ibid., p. 35).

You may then come across the good news that this international collaboration was quite successful, as recently stated by the United Nations Environment Programme (UNEP):

January 9, 2023

"Ozone layer recovery is on track, helping avoid global warming by 0.5°C [...]

The UN-backed Scientific Assessment Panel to the Montreal Protocol on Ozone Depleting Substances quadrennial assessment report, published every four years, confirms the phase out of nearly 99% of banned ozone-depleting substances. The Montreal Protocol has thus succeeded in safeguarding the ozone layer, leading to notable recovery of the ozone layer in the upper stratosphere and decreased human exposure to harmful ultraviolet (UV) rays from the sun." (UNEP, 2023)

Later, browsing online through your search results, you may take notice of more diverging headlines from recent years, however:

```
April 21, 2020

"Spring 2020 brings rare ozone 'hole' to the Arctic" (NOAA, 2020)

December 15, 2022

"Copernicus: Unusually persistent Antarctic ozone holes in 2020-2022" (CAMS, 2022)

October 4, 2023

"Ozone hole goes large again" (ESA, 2023)
```

```
July 30, 2024
```

"Copernicus: High temperatures trigger seasonal ozone pollution across Europe" (CAMS, 2024)

October 30, 2024

"2024 Antarctic ozone hole ranks 7th-smallest since recovery began" (NOAA, 2024)

March 18, 2025

"CAMS monitors unusually low Arctic ozone levels during 2025" (CAMS, 2025)

The ozone hole is growing? Arctic ozone depletion and increasing ozone concentrations at the earth's surface during recent years? Climate change? – How do all these observations fit to the world's efforts for several decades on protecting the ozone layer? What if this was all for nothing? How much do we really know about what's going on?

For sure, you were not the only one asking questions. – It is for science to take the floor and to tell the world more about the protagonist.

1.2 Ozone in the lowermost stratosphere

♦ This section provides a brief overview of general scientific knowledge relevant for this work. Therefore, only selected references to the related literature are provided and extensive citation is mostly omitted for better readability. The papers I–III in Chapters 2–4 of this thesis each include a more thorough introduction to the corresponding topics.

Atmospheric ozone is mainly generated through photolysis of oxygen in the stratosphere (Chapman, 1929), where the production rates are largest in lower latitudes due to continuously strong incoming solar radiation fluxes throughout the whole year (e.g., Salawitch et al., 2023). This is illustrated by the ozone mass mixing ratio (MMR) relative to air, maximizing in the tropics as shown for the Northern Hemisphere and winter time (December–February) by the black contour lines in Fig. 1.1a, based on ERA5 reanalysis data (2000–2019). The altitude of this MMR maximum is determined by the balance between oxygen concentration decreasing with height and optical absorption by the ozone molecules reducing the transmission of ultraviolet radiation (cf. Match et al., 2025).

Ozone is globally distributed by the large-scale atmospheric circulation, in particular by the Brewer–Dobson circulation (BDC) in the stratosphere (Dobson et al., 1929; Brewer, 1949; Butchart, 2014). The BDC is commonly explained to be driven by atmospheric waves of different scales, i. e., quasi-adiabatic perturbations of the atmospheric mean flow that usually propagate from tropospheric regions upwards into higher altitudes. These large-scale (planetary) or smaller-scale (synoptic) waves, both often associated with eddy

1. Introduction

dynamics, then mostly dissipate in the higher stratosphere or in the subtropical jet stream region and lower stratosphere, respectively, decreasing the momentum of the zonal mean flow as shown by the color map in Fig. 1.1b (e.g., Charney and Drazin, 1961; Plumb, 2002). In the Northern Hemisphere, this induces a counteracting, poleward mean flow and secondary circulation branches that emerge from the diabatic response of the system (Haynes et al., 1991). The black contour lines in Fig. 1.1b show the residual meridional mass streamfunction in the stratosphere, where the positive values indicate a clock-wise overturning circulation, i. e., upward transport of tropical air masses (and ozone) by the residual mean flow from the lower into the higher stratosphere and subsequent diabatic downwelling in polar latitudes, usually referred to as the deep branch of the BDC (e.g., Birner and Bönisch, 2011). In contrast, the so-called shallow branch of the BDC is limited to the lower stratosphere and features meridional ozone transport on shorter time scales, mostly through horizontal exchange of air masses induced by eddy activity (ibid.). This

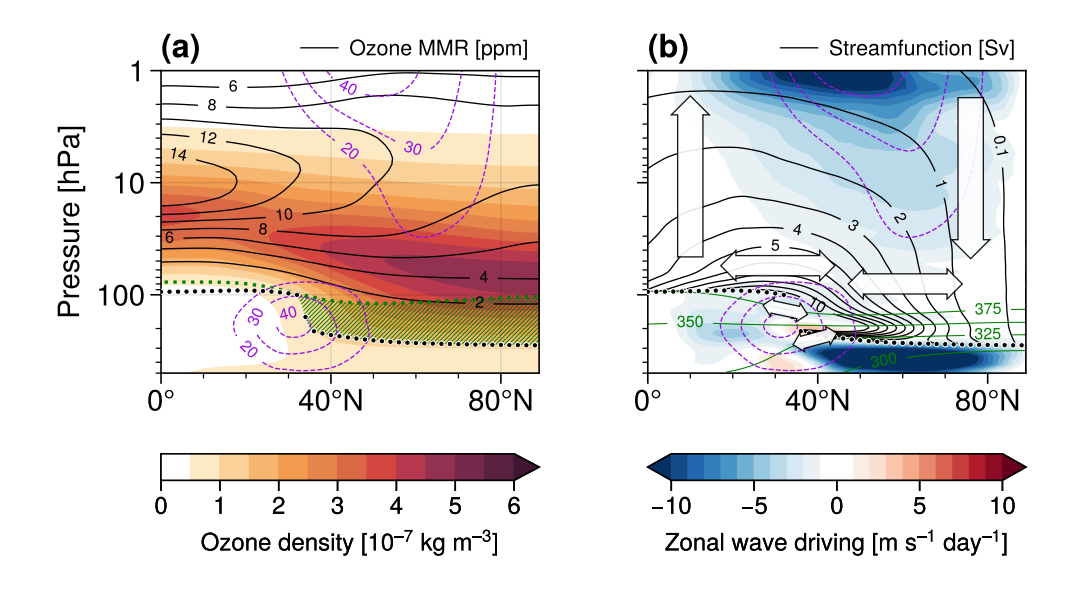


Figure 1.1: (a) Zonally averaged, winter-mean ozone density (color coding) and ozone mass mixing ratios (black contours) based on ERA5 reanalysis data (December–February, 2000–2019). The violet dashed contour lines illustrate the location of the subtropical jet stream and the stratospheric polar vortex, respectively (showing only positive zonal wind speeds, i. e., eastward zonal-mean zonal wind). The thick dotted line represents the mean thermal tropopause height¹. The green dotted line indicates the 380 K isentrope, usually defined as upper boundary of the extratropical lowermost stratosphere (LMS, visualized by the green hatches). (b) Effect of atmospheric waves on zonal momentum budget (color coding; following Andrews et al., 1983) and residual meridional mass streamfunction² (black contours, shown above tropopause only) in units of Sverdrups, 1 Sv = 10⁹ kg s⁻¹ (following definitions as in Mak, 2012; Adam et al., 2018). The green contour lines show selected isentropes in the LMS. The vertical arrows and horizontal double arrows illustrate diabatic advection and meridional eddy mixing, respectively. Other details as in (a). Figure inspired by Bönisch et al. (2011, Fig. 1) and Holton et al. (1995, Fig. 3).

meridional eddy mixing is visualized by double arrows in Fig. 1.1b. The vertical arrows illustrate the diabatic up- and downwelling associated with the deep circulation branch.

The northern hemispheric, extratropical lowermost stratosphere (LMS; cf. Fig. 1.1a) covers the lower stratospheric region just above the tropopause in middle and higher latitudes, equatorward of the subtropical jet stream that is located around 30°N during Boreal winter (e.g., Gettelman et al., 2011). The upper boundary of the LMS is usually set around the 380 K isoline of potential temperature: while this isentrope on average is always located at or above the thermal tropopause (green dotted contour in Fig. 1.1a), this is not the case for isentropes further below (cf. Fig. 1.1b) that are crossing the tropopause and therefore connecting the LMS and the (sub-)tropical troposphere (e.g., Holton et al., 1995). This allows for exchange of air masses between the upper troposphere and lower stratosphere through cross-tropopause, quasi-adiabatic eddy mixing, i.e., wave-driven tracer transport along these isolines of constant potential temperature, $d\theta/dt = Q \simeq 0$ (ibid.). The LMS is therefore often considered as intermediate domain between the upper troposphere and lower to middle stratosphere, featuring complex transport mechanisms that are influenced by both stratospheric and tropospheric dynamics on various scales in space and time (cf. Gettelman et al., 2011). The hemispheric maximum of winter-mean ozone density is located just above the upper boundary of the LMS in polar latitudes (cf. Fig. 1.1a), reflecting the strong equatorward and downward transport of ozone by the BDC during the winter months. As a result, the LMS features strong ozone background gradients in both the horizontal and vertical direction. The contrast between ozone-rich air masses in the lower stratosphere and substantially decreased ozone concentrations in the upper troposphere is reinforced along the tropopause and the tropopause break in the subtropics, where the tropopause and the subtropical jet stream due to their dynamical properties both strongly influence tropospheric wave propagation and tracer transport across the tropopause region. Previous research provided evidence that the LMS is crucial for understanding variability of harmful near-surface ozone that is influenced by crosstropopause ozone transport from the LMS into the troposphere (e.g., Albers et al., 2018).

Ozone is known to strongly interact with circulation dynamics due to its feedback to the local radiation budget. With that, ozone was shown to be associated with long-term circulation trends that partly even counteract those induced by increasing greenhouse gas concentrations in the atmosphere (e. g., Dietmüller et al., 2014; Chiodo et al., 2018; Chiodo and Polvani, 2019; Hufnagl et al., 2023). Extending the knowledge on stratospheric ozone

¹ Computation of thermal tropopause heights is based on the PyTropD package for Python (Adam et al., 2018; Ming, 2022) and Python code produced by P. Conrat Fuentes (LMU Munich).

² Meridional mass streamfunction calculated using PvTropD.

1. Introduction

and the transport processes involved therefore can help to improve climate modeling and reduce uncertainties in climate trend projections (e.g., Nowack et al., 2015). Recent studies showed that stratospheric ozone trends obtained from state-of-the-art climate simulations significantly differ from historical ozone measurements, which suggests that some of the relevant physical mechanisms may not have been fully resolved by modern climate models (e.g., Ball et al., 2020; Dietmüller et al., 2021; Benito-Barca et al., 2025). At the same time, the limited availability of observational data in the lower stratosphere complicates research on LMS ozone and calls for comprehensive and high-resolved model output that just started to become available during recent years.

1.3 Key questions

In the following, three papers are presented that study aspects of lower-stratospheric ozone transport, mostly in relation to the high relevance of dynamical variability in the Northern Hemisphere during winter time. Using tools of statistical data analysis and a broad range of long-term observational records, reanalysis data from various forecasting centers and a variety of modern chemistry-climate simulations, these studies aim to contribute to the understanding of the role of ozone, stratospheric transport and the related physical processes in our climate system. In particular, three key questions will be addressed:

- I. Which are the dominant dynamical drivers of ozone variability in the extratropical stratosphere during winter and how do they affect LMS ozone?
- II. How can we exploit the structural features of the LMS ozone distribution to track circulation variability?
- III. What are the relevant transport contributions to the LMS ozone budget?

Here, questions I. and II. refer to ozone variability and large-scale circulation changes on various time scales, representing both the intrinsic fluctuations of the atmospheric system as well as possible externally forced perturbations (cf. Leith, 1975). The detailed climatological aspects of stratospheric ozone transport are addressed in question III., focusing on the smaller-scale structures and complex mechanisms in the LMS region. Question II. is furthermore motivated by the unique linkage of manifold physical processes affecting ozone in the LMS and the question on potential applications resulting therefrom.

The papers I–III are included in Chapters 2, 3 and 4. Chapter 5 provides the summary and discussion of the results following the corresponding key question for each paper, together with an outlook on related applications and subsequent research questions.

Chapter 2

Paper I

Publication details

Title: On the pattern of interannual polar vortex-ozone

co-variability during northern hemispheric winter

Authors: Frederik Harzer, Hella Garny, Felix Ploeger,

Harald Bönisch, Peter Hoor and Thomas Birner

Journal: Atmospheric Chemistry and Physics

Publisher: Copernicus Publications

Publication date: September 26, 2023

DOI: https://doi.org/10.5194/acp-23-10661-2023

Author contributions

"FH performed the analyses, supervised by HG and TB. TB initiated the project and processed the ERA-Interim reanalyses. FP provided the MLS observational data. FH wrote the first draft of the paper. All authors contributed in interpreting the results and improving the paper." (Paper I, p. 10672)

Copyright information

This work was published under the Creative Commons Attribution 4.0 license (details on this license are available at https://creativecommons.org/licenses/by/4.0/).

17

Atmos. Chem. Phys., 23, 10661–10675, 2023 https://doi.org/10.5194/acp-23-10661-2023 © Author(s) 2023. This work is distributed under the Creative Commons Attribution 4.0 License.





On the pattern of interannual polar vortex-ozone co-variability during northern hemispheric winter

Frederik Harzer¹, Hella Garny^{2,1}, Felix Ploeger^{3,4}, Harald Bönisch⁵, Peter Hoor⁶, and Thomas Birner^{1,2}

¹Meteorological Institute, Ludwig-Maximilians-Universität München, Munich, Germany
 ²Institute of Atmospheric Physics, Deutsches Zentrum für Luft- und Raumfahrt, Oberpfaffenhofen, Germany
 ³Institute of Energy and Climate Research, Stratosphere (IEK-7),

Forschungszentrum Jülich, Jülich, Germany

⁴Institute for Atmospheric and Environmental Research, University of Wuppertal, Wuppertal, Germany
⁵Institute of Meteorology and Climate Research, Karlsruhe Institute of Technology, Karlsruhe, Germany
⁶Institute for Atmospheric Physics, Johannes Gutenberg University, Mainz, Germany

Correspondence: Frederik Harzer (frederik.harzer@physik.lmu.de)

Received: 20 January 2023 – Discussion started: 13 February 2023 Revised: 29 June 2023 – Accepted: 1 August 2023 – Published: 26 September 2023

Abstract. Stratospheric ozone is important for both stratospheric and surface climate. In the lower stratosphere during winter, its variability is governed primarily by transport dynamics induced by wave-mean flow interactions. In this work, we analyze interannual co-variations between the distribution of zonal-mean ozone and the strength of the polar vortex as a measure of dynamical activity during northern hemispheric winter. Specifically, we study co-variability between the seasonal means of the ozone field from modern reanalyses and polar-capaveraged temperature at 100 hPa, which represents a robust and well-defined index for polar vortex strength. We focus on the vertically resolved structure of the associated extratropical ozone anomalies relative to the winter climatology and shed light on the transport mechanisms that are responsible for this response pattern. In particular, regression analysis in pressure coordinates shows that anomalously weak polar vortex years are associated with three pronounced local ozone maxima just above the polar tropopause, in the lower to mid-stratosphere and near the stratopause. In contrast, in isentropic coordinates, using ERA-Interim reanalysis data, only the midto lower stratosphere shows increased ozone, while a small negative ozone anomaly appears in the lowermost stratosphere. These differences are related to contributions due to anomalous adiabatic vertical motion, which are implicit in potential temperature coordinates. Our analyses of the ozone budget in the extratropical middle stratosphere show that the polar ozone response maximum around 600 K and the negative anomalies around 450 K beneath both reflect the combined effects of anomalous diabatic downwelling and quasi-isentropic eddy mixing, which are associated with consecutive counteracting anomalous ozone tendencies on daily timescales. We find that approx. 71 % of the total variability in polar column ozone in the stratosphere is associated with year-by-year variations in polar vortex strength based on ERA5 reanalyses for the winter seasons 1980–2022. MLS observations for 2005-2020 show that around 86 % can be explained by these co-variations with the polar vortex.

1 Introduction

Atmospheric ozone has manifold effects on human health and ecosystems on Earth (e.g., Barnes et al., 2022). Furthermore, ozone is known to contribute to climate feedbacks due to its radiative properties (IPCC, 2023; WMO, 2022), emphasizing its relevance for atmospheric and climate sciences. For example, Arctic ozone variability was found to substantially impact tropospheric and surface climate (Smith and Polvani, 2014; Calvo et al., 2015; Ivy et al., 2017; Friedel et al., 2022a, b). Diagnostics based on Antarctic ozone depletion have been proposed to improve seasonal forecasts due to robust correlations with the southern annular mode (Son et al., 2013; Bandoro et al., 2014). Moreover, recent studies reported significant effects of CO2-induced ozone changes on climate sensitivity and on the tropospheric circulation based on models that include interactive ozone (Dietmüller et al., 2014; Nowack et al., 2015, 2018; Chiodo and Polvani, 2017, 2019; Chiodo et al., 2018).

Interannual variability, i.e., variability based on year-byyear anomalies, sheds light on the intrinsic climate fluctuations in the atmosphere and, hence, is essential for understanding long-term trends, e.g., due to external anthropogenic forcings. Several studies exist in the literature that address the relationship between ozone variability and stratospheric dynamics on this timescale. In particular, planetary waves in the stratosphere, resulting from tropospheric wave activity, have been shown to modulate transport and the zonal-mean distribution of ozone (Hartmann and Garcia, 1979; Garcia and Hartmann, 1980). Based on observational data, a case study by Leovy et al. (1985) demonstrated that the concept of wave breaking can be used to explain co-variability between ozone and potential vorticity in the polar vortex region. Kinnersley and Tung (1998) analyzed the impact of the quasi-biennial oscillation and planetary wave anomalies on global ozone. Detailed insights into yearby-year variability in atmospheric ozone from both models and observations were provided in subsequent work, mostly based on the upward Eliassen-Palm flux and meridional eddy heat transport at the 100 hPa level as the metrics for stratospheric wave driving (Fusco and Salby, 1999; Randel et al., 2002; Weber et al., 2003; Ma et al., 2004).

While previous studies primarily focused on variations in column ozone, in this work we draw attention to the vertically resolved pattern of year-by-year ozone variability. To start, consider Fig. 1, which shows maps of local sample standard deviations for zonal-mean ozone relative to the winter climatology, based on detrended seasonal-mean data for northern hemispheric winters (December–February, DJF) from two modern reanalyses (ERA-Interim and ERA5) and MLS satellite measurements. More details on the data used are provided in Sect. 2 below. Although these three datasets show considerable quantitative differences, the three maps consistently show a striking tripole structure over the polar cap with isolated variance maxima near the tropopause, in the

middle stratosphere and near the stratopause. In this study, we demonstrate that major parts of this variability structure are congruent with interannual co-variations with the stratospheric polar vortex. To do so, we apply a linear regression approach with the seasonal strength of the polar vortex as the predictor, which is characterized by a simple index time series based on polar-cap-averaged temperature at 100 hPa. We limit our analyses to the Northern Hemisphere since the polar vortex features substantially stronger dynamical variability compared to the Southern Hemisphere. This allows for stronger coupling to ozone transport there. Furthermore, we focus on variations in the polar stratosphere, which are expected to be governed mainly by the Brewer-Dobson circulation, coupled to the variability in polar vortex strength. We find that the resulting winter-mean ozone response pattern may be explained by the combined effects of mixing and residual circulation transport, consistent with previous work focusing on column ozone and the response to sudden stratospheric warmings (e.g., de la Cámara et al., 2018a, b; Hong and Reichler, 2021; Bahramvash Shams et al., 2022).

The paper is structured as follows. In Sect. 2, we list the data used for this study and discuss the setup for the linear regressions. The resulting ozone response patterns are documented in Sect. 3, where we combine regression maps for both pressure and potential temperature coordinates. This allows us to estimate the relative contributions linked to diabatic and adiabatic vertical transport of ozone in the lower polar stratosphere, respectively. In Sect. 4, an ozone budget analysis derived from daily ERA-Interim reanalysis data provides further details on how transport variations produce ozone anomalies at the different levels and regions in the latitude–height plane. Section 5 summarizes our results and provides a brief outlook.

2 Data and methods

For the main part of this study, we use model level output of ERA-Interim reanalyses (Dee et al., 2011) for 1979–2016, which we interpolated on pressure and potential temperature levels such that the full vertical resolution of the model was preserved. With that, we consider zonal-mean data on both pressure and isentropic levels on a vertical range roughly from 1000 to 1 hPa and 260 to 1800 K, respectively, with a meridional resolution of about 0.7°. Monthly means are derived from 6 h daily data and are combined for seasonally averaged fields for December–February (DJF) 1980–2016. Each DJF winter season is denoted with the year of the corresponding January month.

Detailed assessments show that ERA-Interim (ERAI) ozone in the lower stratosphere is in reasonable agreement with observations and other reanalysis products (Dragani, 2011; Albers et al., 2018; Davis et al., 2022). We intend to provide further validation by comparing our results obtained from ERAI on pressure levels with those based on the lat-

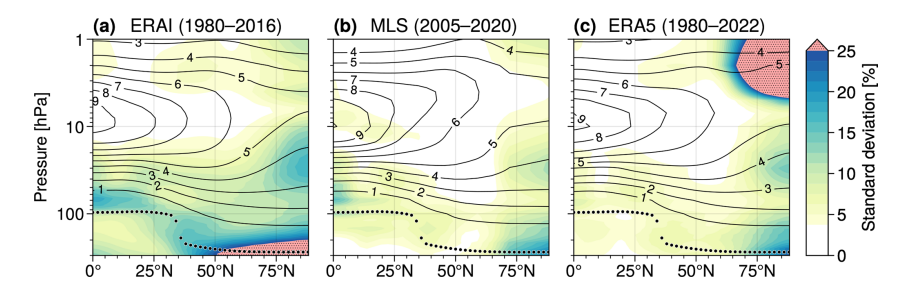


Figure 1. Maps of ozone variability (DJF), based on local sample standard deviations relative to the ozone DJF climatology (shown by the solid contour lines in units of parts per million by volume), for ERA-Interim (ERAI), MLS and ERA5. The thick dotted lines show the mean thermal tropopause derived from ERAI data. For ERAI and ERA5, extreme ozone variations (indicated by red shading and stippling) are caused by outliers. Note that throughout this study, thermal tropopause heights are calculated using PyTropD (Adam et al., 2018), following the definition by WMO (1957).

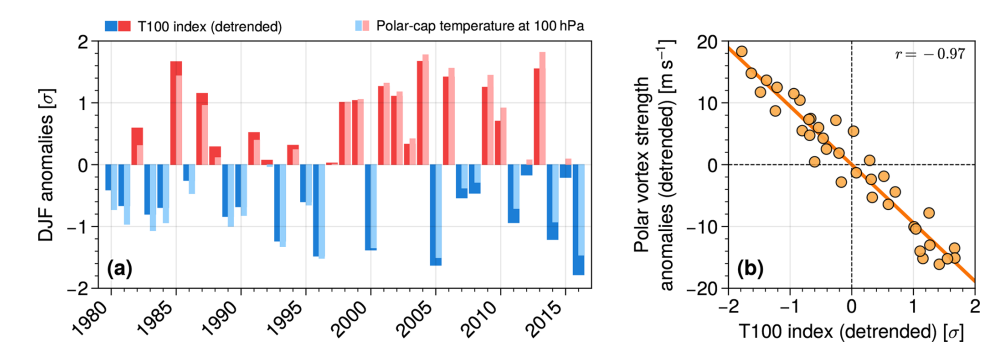


Figure 2. (a) T100 index obtained from ERAI reanalysis data, adjusted for a linear trend in time as required for the linear regression approach. The underlying polar-cap-averaged temperature anomalies at the 100 hPa level, without this trend removed, are shown by the thin bars. Both time series are standardized by the standard deviation of the T100 index, $\sigma = 2.6$ K. (b) Interannual anomalies of the zonal-mean zonal wind at the polar vortex around 60° N and 10 hPa, regressed on the T100 index with a regression coefficient b = -9.4 m s⁻¹ σ ⁻¹ and correlation r = -0.97. All results are for ERAI, DJF 1979/80–2015/16.

est ERA5 reanalyses for DJF 1960-2022 with regular 1.5° meridional grid spacing (Hersbach et al., 2019, 2020; Bell et al., 2021). ERA5 data for the pre-satellite era, covering DJF 1960-1980, will be evaluated separately. In addition, we use ozone observations from the Microwave Limb Sounder (MLS) instrument on board the Aura satellite, data version 5 (Waters et al., 2006; Livesey et al., 2022). The spatial sampling of MLS is comparatively high, with about 3500 profiles along about 15 orbits per day, covering the globe between about 82° S and 82° N. The MLS profile data have been interpolated on potential temperature levels, and monthly mean zonal-mean climatologies have been compiled for both pressure and potential temperature levels. In this paper, MLS data are considered on pressure levels for DJF 2005-2020 on a non-regular latitudinal grid with mean resolution of approx. 4.2°.

Throughout this study, correlations are measured by using local Pearson correlation coefficients r and p values are calculated using a two-sided Wald t test. Statistical significance is assumed if $p \le 0.05$. The correlation coefficients'

95 % confidence intervals are computed based on Fisher's z transformation.

Co-variability between stratospheric ozone and polar vortex strength is studied by using a simple linear least-squares regression model: first, we define an index time series that is derived from interannual zonal-mean temperature, interpolated at the 100 hPa pressure level and averaged over the Northern Hemisphere's polar cap,

$$\overline{T}_{100}(t) \equiv \langle \overline{T}(t, p = 100 \,\text{hPa}, \phi) \rangle_{\phi \ge 60^{\circ} \,\text{N}}, \tag{1}$$

which we will refer to as "T100 index" in the following. Here, overbars indicate the zonal mean and squared brackets denote meridional averaging. The relation between the T100 index and polar vortex strength variability is discussed below within the context of atmospheric dynamics. Then, for a given variable field \overline{y} , the corresponding anomalies $\delta \overline{y}$ are regressed on this index according to

$$\delta \overline{y}(t) = a + b \cdot \overline{T}_{100}(t) + \epsilon(t). \tag{2}$$

For both the index and the anomaly time series, potential linear trends across the whole time range under consideration

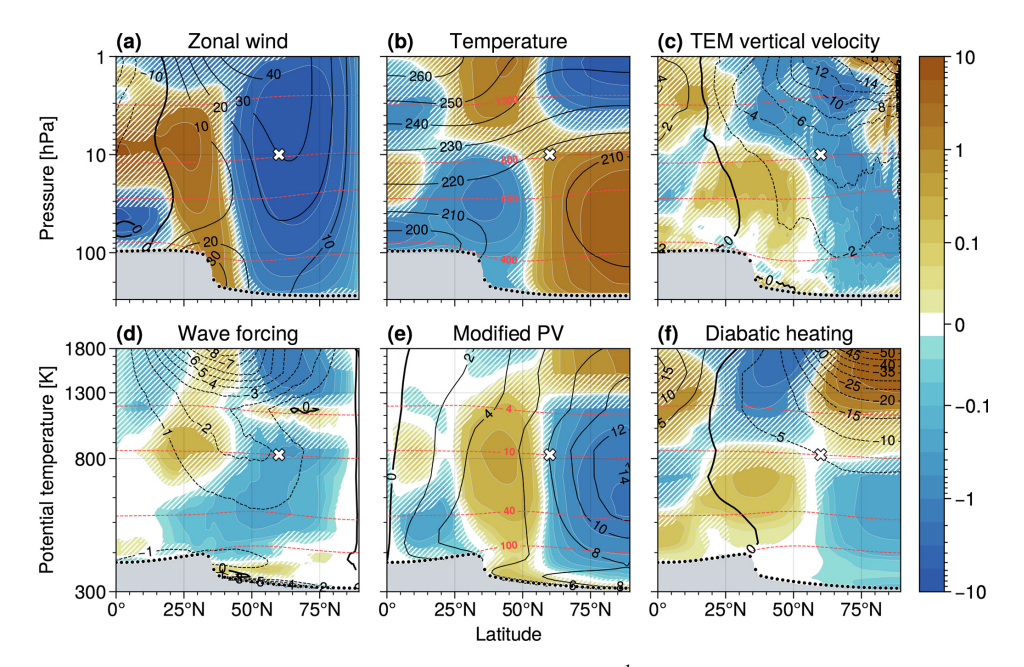


Figure 3. Interannual anomalies of the zonal-mean (a) zonal wind (in units of m s⁻¹), (b) temperature (K), (c) TEM vertical velocity in log-p coordinates (km month⁻¹), i.e., $W_r = -(H/p)\omega_r$ with scale height H = 7 km and ω_r from Eq. (3), (d) PV flux v flux v for v flux v flux v for v flux v

are identified through separate linear least-squares regressions and removed beforehand. Finally, the set of regression coefficients $b(p,\phi)$ yields a "T100 regression map" across the latitude—height plane that quantifies the statistical linear response of \overline{y} if polar stratospheric temperature, measured by the standardized T100 index, is varied by 1 standard deviation. In this work, this regression model is primarily applied to zonal-mean year-by-year anomalies covering DJF winter seasons on the Northern Hemisphere. When daily anomalies are considered, the procedure is similar except that in addition the time series are deseasonalized beforehand.

The detrended and standardized T100 index derived from ERAI reanalyses for DJF 1980–2016 is provided in Fig. 2a. Choosing this T100 predictor for studying polar vortex covariability is justified due to its strong dependence on variations in the zonal wind in the polar vortex region at 60° N and 10 hPa, as shown in Fig. 2b. We therefore obtained a well-defined and powerful proxy diagnostic for the strength of the polar vortex during northern hemispheric winters. Based on temperature as a fundamentally constrained variable instead

of zonal wind, this definition features a robust T100 time series across other selected reanalysis products and for moderate changes in the pressure level at which this index is evaluated (not shown).

The polar-cap lower-stratospheric temperature and the strength of the polar vortex are coupled via downward control (Haynes et al., 1991). Some important variable fields, which are intended to illustrate this mechanism, and their T100 regression maps are provided in Fig. 3. Briefly, starting with anomalously strong wave activity of tropospheric origin, westerly winds in the polar vortex region are reduced (as shown in Fig. 3a) upon enhanced wave dissipation, inducing a wave-driven poleward residual flow that counteracts the weakening of the background zonal wind due to the Coriolis effect. The wave forcing is indicated by enhanced equatorward potential vorticity (PV) fluxes around the 800 K isentrope in Fig. 3d, which reduce PV above the polar cap (Fig. 3e). The associated temperature response in Fig. 3b is consistent with thermal wind balance. Downwelling (upwelling) is associated with adiabatic warming (cooling), such

that by continuity this closes the anomalous residual circulation. This vertical motion (shown with log-*p* scaling in Fig. 3c) is captured in the transformed Eulerian mean (TEM) framework by (e.g., Andrews et al., 1987)

$$\overline{\omega}_{\rm r} = \overline{\omega} + \frac{1}{a\cos\phi\partial_p\overline{\theta}}\partial_\phi \left(\overline{v'\theta'}\cos\phi\right),\tag{3}$$

where $\overline{\omega} = \mathrm{d} p/\mathrm{d} t$ is the vertical velocity in pressure coordinates, $\overline{\theta}$ denotes zonal-mean potential temperature, $\overline{v'\theta'}$ indicates the meridional eddy heat transport and a is the Earth's radius. The change in potential temperature due to diabatic heating in Fig. 3f can be consistently explained to damp the wave-driven temperature perturbations through radiative cooling.

The underlying mechanism has been widely discussed in studies on stratosphere–troposphere coupling, where the T100 index described above has been introduced (Baldwin et al., 2019; Domeisen et al., 2020). On sub-seasonal timescales, similar effects are observed, e.g., during sudden stratospheric warmings (Butler et al., 2017; Baldwin et al., 2021).

Previous studies often referred to the meridional eddy heat transport at 100 hPa as an indicator for the total available wave driving of the stratosphere (e.g., Fusco and Salby, 1999; Randel et al., 2002; Ma et al., 2004; Weber et al., 2003, 2011; Strahan et al., 2016). However, it is unclear how this wave driving manifests in terms of its latitude-height structure. Furthermore, this metric is more complex than the T100 index, such that it may be less robust across different data products. Following Weber et al. (2011), we used the zonal-mean meridional eddy heat flux v'T' at 100 hPa averaged between 45 and 75° N ("VT100 index") from ERAI reanalyses and briefly assessed the resulting signature for ozone co-variability (DJF, 1980-2016). From a regression analysis, we found clear similarities in the response patterns obtained for the T100 DJF (discussed below) and the VT100 NDJ (November–January, see Appendix A) time series. This time lag between the T100 and VT100 predictors consistently supports the interpretation of anomalous eddy heat fluxes that precede wave-induced deceleration of the polar vortex by several weeks (Newman et al., 2001; Polvani and Waugh, 2004).

3 Polar vortex-ozone co-variability: T100 response patterns

In the lower stratosphere, it is mainly the Brewer–Dobson circulation (BDC) that captures ozone transport from the tropics towards higher latitudes (Gettelman et al., 2011; Butchart, 2014). Since wave forcing impacts the strength of both the polar vortex and the BDC, an anomalously weak polar vortex tends to be associated with enhanced poleward ozone transport and, hence, increased polar ozone amounts. Previous studies reported strong coupling between

the strength of the BDC and stratospheric temperature (Fu et al., 2010; Weber et al., 2011; Young et al., 2012), which suggests substantial interannual co-variability between the T100 diagnostic and stratospheric ozone. In this section, we aim to document this T100 ozone response pattern and provide a comparison based on two different perspectives, i.e., using pressure and potential temperature as the vertical coordinate, respectively.

First, Fig. 4 shows zonal-mean ozone volume mixing ratios $\overline{\chi}$ on pressure levels, from ERAI and ERA5 reanalysis data as well as from MLS observations, regressed on the standardized ERA5 T100 index. This index represents an extended (available for DJF 1980-2022) but essentially equivalent version of the ERAI T100 time series due to its outstanding high correlation, r > 0.99. The regression maps are provided in relative units, based on the corresponding ozone DJF climatology, and per standard deviation of the T100 time series. The stratospheric response signatures show very good agreement among the different datasets in Fig. 4. This is especially worth noting due to the substantial differences in the strength of general ozone variability in Fig. 1. From a more detailed analysis, robust results were found for other selected reanalysis products and for modern chemistry-climate models (not shown; see also von Heydebrand, 2022).

In general, Fig. 4 supports the idea that higher ozone amounts over the polar cap are related to anomalously strong poleward transport due to a stronger BDC during weak polar vortex years. This is consistent with the diabatic heating response in Fig. 3f that suggests anomalous upwelling (downwelling) in lower (higher) latitudes for ERAI and, hence, a stronger stratospheric residual circulation. Moreover, the results reflect the vertical structure of year-by-year ozone variability, featuring those three pronounced variance maxima above the polar cap previously discussed with Fig. 1. In addition, the T100 regression maps show another spot of enhanced ozone in the mid-latitudes slightly below the 100 hPa level, which is roughly between the two lowest polar response maxima.

To understand these features, we gain some first insights from just evaluating the differences among the response signatures obtained for pressure and potential temperature as the vertical coordinate. For this, consider Fig. 5, which shows the T100 regression maps for zonal-mean ozone $\overline{\chi}$ on pressure levels (top row) and density-weighted ozone, $\overline{\chi}^* = \overline{\rho_\theta \chi}/\overline{\rho_\theta}$ with isentropic density $\rho_\theta = g^{-1}\partial_\theta p$, for potential temperature coordinates (bottom row). Both computations were obtained from ERAI reanalysis data for DJF 1980–2016. For comparison, the response signatures are displayed not only in relative units (right column) but also as absolute anomalies in parts per million by volume (left column), 1 ppmv = 1×10^{-6} mol mol $^{-1}$.

The results show clear differences among the two coordinate frameworks, which shed light on some relevant transport processes that build up this ozone response signature. For example, consider the two upper polar response max-

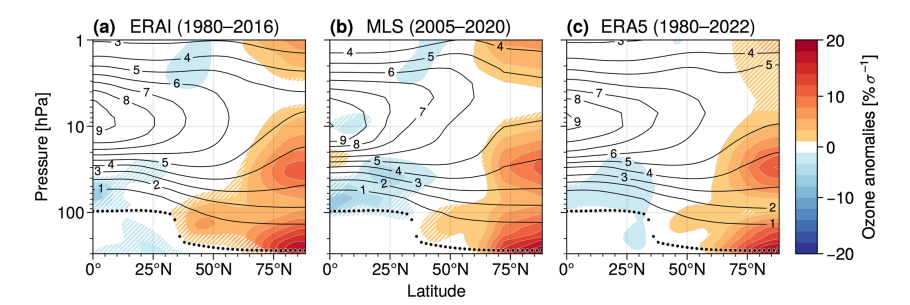


Figure 4. Interannual zonal-mean ozone on pressure levels from (a) ERAI (DJF 1980–2016), (b) MLS (2005–2020) and (c) ERA5 (1980–2022), regressed on the standardized ERA5 T100 index. The response signatures are provided as relative anomalies (in $\% \sigma^{-1}$) based on the respective ozone DJF climatology that is shown by the black contour lines each (in parts per million by volume). The thick dotted lines show the mean thermal tropopause for DJF, derived from ERAI. Other details as in Fig. 3.

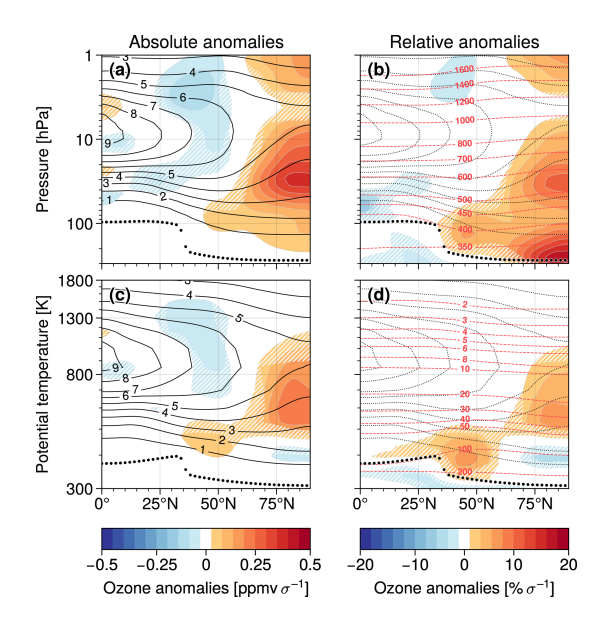


Figure 5. (a) T100 regression map for anomalous zonal-mean ozone $\overline{\chi}$ on pressure levels (ERAI, DJF 1980–2016). (b) Same as in (a) but the response signature is given by relative anomalies with respect to the DJF ozone climatology. (c and d) Corresponding T100 regression maps for density-weighted zonal-mean ozone on potential temperature levels, $\overline{\chi}^* = \overline{\rho_\theta \chi}/\overline{\rho_\theta}$, where ρ_θ is isentropic density. Details as in Fig. 4.

ima around 1 and 30 hPa, respectively, and the corresponding minima at similar altitudes around 40° N, more pronounced in the absolute anomalies (top row in Fig. 5). We expect them to arise due to the quadrupole-like response in temperature and TEM vertical velocity (Fig. 3b and c), associated with the anomalously weak polar vortex in Fig. 3a. The sign of the ozone response directly follows from the anomalous upand downwelling acting on the local vertical gradient of the background ozone distribution. In contrast, this response is much weaker in potential temperature coordinates (bottom

row in Fig. 5). This is because vertical ozone transport includes a component due to adiabatic motion, which satisfies ${\rm d}\theta/{\rm d}t=0$ and which can be thought of as shifting the isosurfaces of both ozone and potential temperature simultaneously. Thus, for vertical transport, unlike the diabatic part, the adiabatic proportion is implicitly accounted for in isentropic coordinates. Konopka et al. (2009) used similar arguments to explain differences in the amplitude of the seasonal cycle of tropical ozone when viewed in pressure and isentropic coordinates.

In the lowermost stratosphere just above the polar tropopause, we find the most remarkable differences among the results for the two coordinate systems used in Fig. 5. Regarding pressure levels, from Fig. 5b we find a pronounced ozone response maximum with relative anomalies of more than $15\%\sigma^{-1}$. Using potential temperature as the vertical coordinate, we instead obtain a decrease in ozone there in Fig. 5d, suggesting that anomalous downwelling (shown in Fig. 3c) contains a much larger adiabatic component there compared with higher stratospheric regions. This is consistent with smaller radiative damping rates that are observed in the lower polar stratosphere and that limit the effectiveness of diabatic cooling (Hitchcock et al., 2010).

The large differences between pressure and isentropic coordinates in the lowermost stratosphere are also apparent when considering variations in the polar-cap tropopause (Fig. 6): tropopause pressure shows a much larger response to T100 variability (by about a factor of 10) than potential temperature, indicating that polar tropopause height variability is mainly governed by adiabatic processes. Significantly enhanced ozone then is observed where the substantial lowering of the tropopause height allows for downward transport of stratospheric ozone into former tropospheric regions, which is the case for pressure rather than potential temperature coordinates. As a result, enhanced ozone is found at the polar tropopause in Fig. 5b, where relative anomalies occur that are large compared to the low ozone amounts usually expected in the upper troposphere.

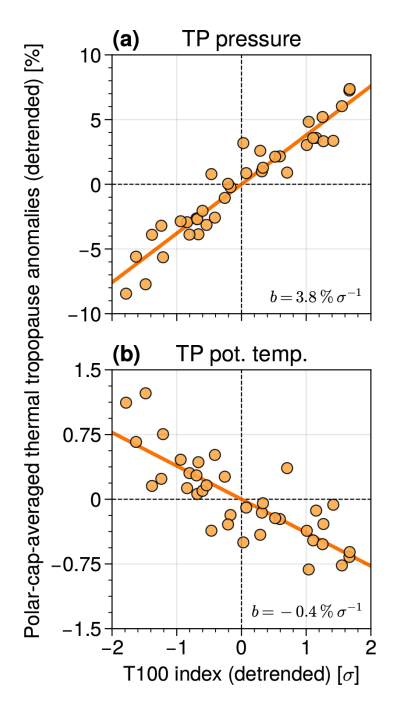


Figure 6. (a) Polar-cap-averaged thermal tropopause (TP) pressure regressed on the T100 index (ERAI, DJF 1980–2016), with slope $b = 3.8 \,\%\,\sigma^{-1}$ from a linear least-squares fit and correlation r = 0.95. Much less co-variability is found in (b) for polar-cap TP potential temperature (r = -0.80).

Taking into account comprehensive research by de la Cámara et al. (2018a, b) on anomalous stratospheric dynamics and Arctic ozone during sub-seasonal sudden stratospheric warming events, we hypothesize that the remaining T100 response signatures in Figs. 4 and 5 can be explained through variations in the BDC, combining the effects of residualmean (net mass) downwelling and quasi-isentropic eddy mixing, depending on the local gradients of stratospheric ozone. Within this context, analyzing the full ozone budget turned out to be appropriate for investigating the actual roles of these transport contributions.

4 Insights into polar vortex–ozone co-variability from the ozone budget

Using isentropic coordinates, the zonal-mean ozone budget reads (e.g., Andrews et al., 1987; Plumb, 2002)

$$\partial_{t} \overline{\chi}^{*} + \frac{\overline{v}^{*}}{a} \partial_{\phi} \overline{\chi}^{*} + \overline{Q}^{*} \partial_{\theta} \overline{\chi}^{*} = \\ -\overline{\rho_{\theta}}^{-1} \left[\frac{1}{a \cos \phi} \partial_{\phi} (\overline{\hat{v} \rho_{\theta} \hat{\chi}} \cos \phi) + \partial_{\theta} \overline{\hat{Q} \rho_{\theta} \hat{\chi}} \right] + \overline{S}^{*}. \tag{4}$$

Here, χ denotes the ozone volume mixing ratio, $Q = \mathrm{d}\theta/\mathrm{d}t$ is the change in potential temperature due to diabatic heating, $\rho_\theta = g^{-1}\partial_\theta p$ is isentropic density and S represents sources and sinks. We use a density-weighted zonal average, $\overline{\chi}^* \equiv \overline{\rho_\theta \chi}/\overline{\rho_\theta}$, with $\hat{\chi} = \overline{\chi} - \overline{\chi}^*$ indicating deviations therefrom and spherical coordinates with geographical latitude ϕ and Earth's radius a. The tendencies induced by mean flow advection and by eddy mixing are accounted for by the terms 0+20 and 3+40, respectively.

Figure 7 provides the T100 regression maps for the relevant dynamical fields and their associated ozone tendencies. We have neglected the contributions due to the mean meridional flow and due to vertical eddy ozone transport, numbered with ① and ④ in Eq. (4), since they are small compared to the other processes (not shown). We further omit contributions to ozone variability due to chemistry, i.e., $S \approx 0$ in Eq. (4), which is typically fulfilled in the lower stratosphere. Under very cold conditions, however, ozone depletion may still become important there (e.g., Brasseur and Solomon, 2005). Contributions due to chemistry cannot be neglected in the upper stratosphere; we therefore limit our budget analysis to lower-stratospheric regions, such that $\theta < 900 \, \text{K}$ in Fig. 7.

The results show that pronounced anomalous ozone tendencies are mainly found between 400 and 700 K, where anomalous diabatic vertical transport above the polar cap brings ozone-rich air to lower altitudes, whereas quasiisentropic eddy mixing counteracts this response by transporting ozone from the polar region to the mid-latitudes. Moreover, Fig. 7d and e show that these two leading contributions to ozone variability, 2 and 3 as labeled in Eq. (4), are largest around 500 K, reflecting the interplay between background ozone gradients and the circulation changes caused by anomalous wave forcing in the polar vortex region according to Fig. 7c. We furthermore note that, especially in higher latitudes, these anomalous contributions 2 and 3 largely compensate for each other. Indeed, the residual ozone tendency is expected to be small, since individual seasonal averages should be approximately in steady state. However, the polar-cap-averaged vertical profiles of the responses in Fig. 7f show clear differences in the absolute strength of these anomalies, suggesting an imbalance of the seasonalmean ozone budget instead, especially near 500 K, where the resulting net tendency is negative, $\partial_t \overline{\chi}^* \approx 2 + 3 < 0$. This may seem to contradict the enhanced seasonal-mean ozone that is found there during weak polar vortex years (e.g., compare Fig. 5c). However, a seasonal-mean net negative tendency would merely state that lower ozone values are found at the end compared to the beginning of the season, but this would still allow for strong positive ozone anomalies during the season. Moreover, the actual diagnosed seasonal-mean net ozone tendency is in fact slightly positive near 500 K (not shown), which indicates that the detailed quantitative balance of the contributions due to diabatic downwelling and quasi-isentropic eddy mixing is not accurately reproduced in ERAI. This is consistent with Fig. 4, which shows higher

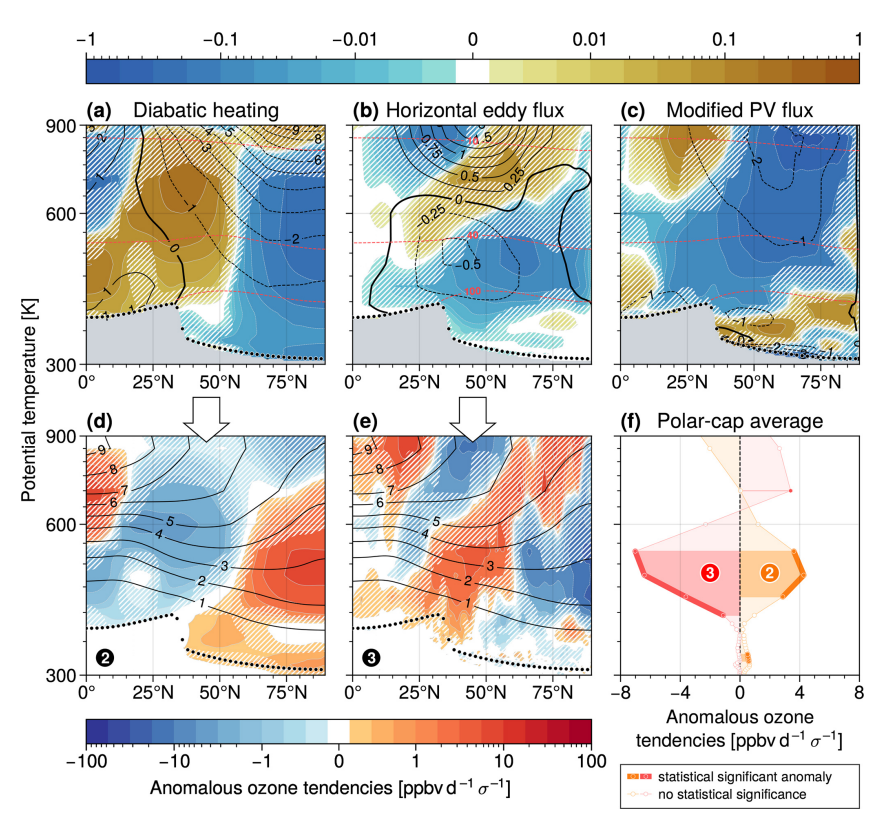


Figure 7. (a) Anomalous diabatic heating rates \overline{Q}^* (in K d⁻¹) and (b) horizontal eddy ozone transport $\overline{v}\rho_\theta\hat{\chi}/\overline{\rho_\theta}$ (in ppmv ms⁻¹) regressed on the T100 index (ERAI). (c) The corresponding regression map for the modified PV flux $\overline{v}\rho_\theta\hat{\Pi}/\overline{\rho_\theta}$ (in PVU ms⁻¹) is added for comparison. Details as in Fig. 3. (d and e) T100 regression maps for the anomalous tendencies @ and @ from Eq. (4). Here, the black contours show the ozone DJF climatology (in parts per million by volume). Note uneven color contour intervals with linear spacing for values within ± 0.01 (a-c) and ± 1 ppbv d⁻¹ σ^{-1} (d and e), respectively, and logarithmic spacing outside those ranges. The anomalous ozone tendencies seem to be weak in the lowermost stratosphere and increase strongly for altitudes higher than 400 K due to increased wave forcing above that isentrope as indicated by the anomalous equatorward PV fluxes in (c). Weak positive ozone tendencies due to enhanced diabatic cooling directly above the tropopause in (d) probably arise from an increase in static stability there, e.g., as observed for sudden stratospheric warmings (Grise et al., 2010; Son et al., 2011; Wargan and Coy, 2016) or can be explained as a second-order feedback reacting to changes in the vertical ozone gradients. (f) Polar-cap-averaged tendencies, $\langle \partial_t \overline{\chi}^* \rangle_{\phi}$ for $\phi \geq 60^\circ$ N, regressed on the ERAI T100 index. Thick solid lines mark isentropes with statistically significant anomalies. All results are for ERAI, DJF 1980–2016.

ozone anomalies in mid-latitudes in ERAI compared to MLS and ERA5, presumably due to excessive horizontal mixing.

These findings need to be treated with caution. In particular, uncertainties in the ERA-Interim reanalyses remain due to data assimilation and due to parameterization of interactive ozone and the associated feedbacks (Davis et al., 2022). Furthermore, diabatic heating rates are solely derived from the model forecasts without any additional constraints and, hence, can introduce additional budget inconsistencies (e.g., Abalos et al., 2015; Monge-Sanz et al., 2022). In conclusion, we do not expect the ozone budget to be closed in ERA-Interim. The cumulative nature and the smaller magnitudes of the winter-mean tendencies may be even more challenging in that respect. We therefore think that such uncertainties only allow for a rather qualitative estimate of the dif-

ferent ozone transport processes. Additional work is needed to compare these results with other reanalysis products, observational data and model simulations. Limited to the data available from ERA-Interim, we did not find a robust response profile for the resulting net tendency that follows from the anomalous tendencies ②+③ in Fig. 7f; i.e., statistical significance (if any) is sensitive to the latitude range chosen for polar-cap averaging (not shown). This suggests that the full seasonal-mean ozone budget may indeed be balanced, such that the T100 response of the net tendency $\partial_t \overline{\chi}^* \approx ② + ③$ in Eq. (4) vanishes for seasonal averages, assuming that ozone chemistry \overline{S}^* does not play a dominant role in the lower stratosphere.

At this point, the contrasting results presented above complicate reliable conclusions on the underlying transport dy-

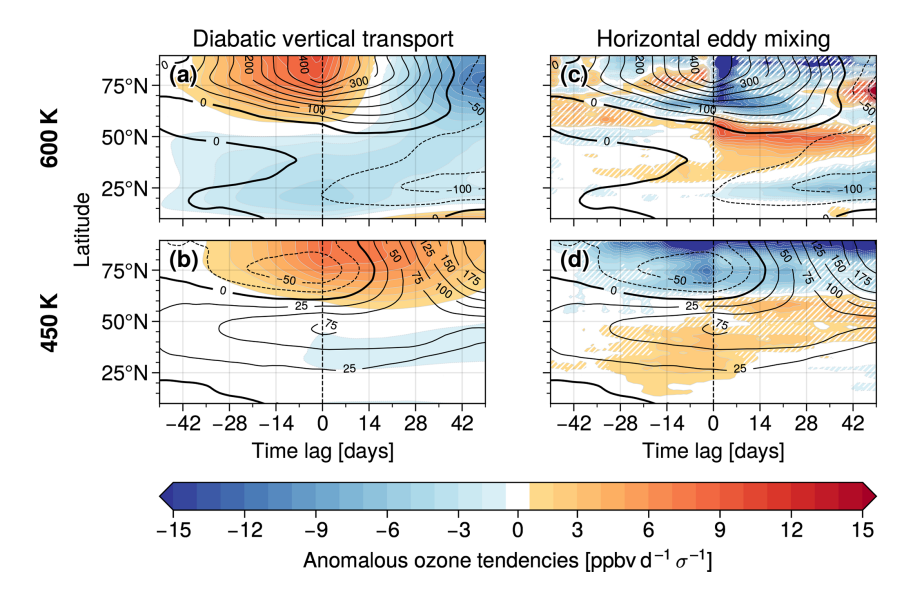


Figure 8. Anomalous ozone tendencies associated with (\mathbf{a} and \mathbf{b}) diabatic heating, @ in Eq. (4), and (\mathbf{c} and \mathbf{d}) horizontal eddy mixing @, respectively, regressed on daily T100 anomalies on the 600 K (\mathbf{a} and \mathbf{c}) and 450 K (\mathbf{b} and \mathbf{d}) isentropes. Evaluation of a robust positive response at 600 K associated with anomalous diabatic mean flow advection in the tropics (not shown), which occurred across all the lag times considered here and possibly includes the response of the quasi-biennial oscillation, remains for subsequent work. Positive (negative) lag times indicate that the field anomalies succeed (precede) the T100 index. Hatching indicates where co-variability is not statistically significant. Black contour lines illustrate T100 lag regressions for daily ozone anomalies $\overline{\chi}^*$ in parts per billion by volume per standard deviation of the daily T100 index. All results are for deseasonalized daily mean ERAI data, covering December, January and February months in 1979–2016.

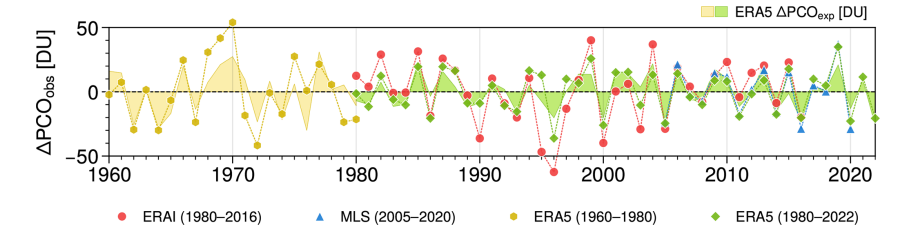


Figure 9. Observed polar-cap-averaged partial column ozone anomalies ΔPCO_{obs} per DJF winter season (line plots) for ERAI, MLS and ERA5 data and, for comparison, explained partial column ozone ΔPCO_{exp} for ERA5 (area plots). See the text for details on the computation.

namics based on winter-mean ozone tendencies. Instead, to reveal more insights into the drivers of the seasonal-mean ozone anomalies, it is useful to study daily variability where the relevant transport contributions may not fully compensate one another, leaving a net ozone tendency that allows for better distinguishing cause and effect. To do so, we perform a linear lag-regression analysis using daily averaged fields based on 6 h ERAI data for the December, January and February months in 1979–2016. We select two isentropes, 600 and 450 K, which represent the polar ozone response maximum and minimum, the latter located beneath the former in Fig. 5c, and assess T100 co-variability for daily ozone and the two relevant dynamical tendencies, ② and ③ in Eq. (4). The results for different lag times, covering 14 weeks in total centered around the T100 anomaly,

are shown in Fig. 8. They are consistent with ozone transport taking place, e.g., during sub-seasonal sudden stratospheric warming (SSW) events (de la Cámara et al., 2018a, b; Hong and Reichler, 2021), though here we present lag regressions for the more general case of daily T100 temperature anomalies, which allows for improved statistics and reduced sensitivity, e.g., on SSW definition thresholds. In Fig. 8, for the 600 K isentrope, we find that enhanced polar ozone is mainly induced by anomalous diabatic mean flow downwelling (for negative lag times in Fig. 8a). Subsequently, a reduction in polar ozone takes place due to increased quasi-horizontal eddy mixing in Fig. 8c out of the polar cap toward midlatitudes, which partly arises as feedback due to strengthened meridional ozone gradients. Concerning the 450 K level, it turns out that the temporal order of the tendencies involved

is now reversed: here, horizontal eddy mixing can be clearly identified to force the negative ozone response in the polar region. This also explains the positive ozone anomaly in the mid-latitudes shown in Fig. 5b and d. Figure 8a and b indicate the anomalies in diabatic mean flow advection propagating downward with time, where they counteract the eddy forcing in lower altitudes. A closer analysis of variations in the underlying wave driving giving rise to anomalous transport, including different contributions due to different parts of the wave spectrum, is beyond the scope of the current analyses and is left for future work.

Overall, our findings here confirm that the complex ozone response signature in the middle stratosphere introduced in Sect. 3 can be explained by the combined effects of horizontal eddy mixing and vertical mean flow advection. The T100 response on sub-seasonal timescales shows significant anomalous ozone tendencies, which consistently explain the variations in seasonal-mean stratospheric ozone but at the same time seem to not influence ozone net tendency on a seasonal scale. The key for this to happen is the two dominant mechanisms of ozone transport that induce competing response tendencies but occur with some temporal distance.

5 Discussion and conclusions

In this paper, we discussed interannual co-variability between the strength of the polar vortex, as indicated by the index time series of polar-cap-averaged temperature at 100 hPa, and zonal-mean ozone during northern hemispheric winters. We focused on the vertically resolved ozone response pattern in the latitude-height plane, which as far as we know has received only little attention in the literature. In particular, we assessed the intriguing ozone response structure in middle and high latitudes across different altitude levels from two different coordinate perspectives: in pressure coordinates, an anomalously weak vortex is associated with increased ozone volume mixing ratios throughout the stratosphere, showing relative maxima just above the polar tropopause, in the lower-to-middle stratosphere and near the stratopause. Using potential temperature as the vertical coordinate, increased ozone is only present in lower altitudes roughly below 900 K and above about 450 K, even showing weakly decreased values in the lowermost stratosphere beneath for ERAI data. We rationalize these disparate ozone variations by a combination of variability in wave-driven quasi-horizontal mixing and vertical advection by the residual circulation. In particular,

- wave-driven anomalous adiabatic up- and downwelling in the polar vortex region cause enhanced polar ozone around 1 and 30 hPa, as well as less ozone equatorwards,
- increased downwelling associated with an anomalously weak polar vortex includes a large adiabatic component and acts to simultaneously shift iso-surfaces of

- potential temperature and ozone also in the lowermost stratosphere, which furthermore results in a lowered tropopause and significantly increased ozone concentrations there, and
- the ozone response signature in the middle stratosphere can be explained by consecutive counteracting anomalous tendencies associated with diabatic downwelling and quasi-isentropic eddy mixing on daily timescales, with varying chronological order depending on altitude.

Our results consistently show that interannual ozone variations are governed by similar dynamical processes as subseasonal ozone variability (see, e.g., Lubis et al., 2017; de la Cámara et al., 2018a, b; Hong and Reichler, 2021; Bahramvash Shams et al., 2022). Moreover, the T100 ozone response pattern clearly reflects the underlying ozone transport anomalies when viewed in the latitude—height plane with a vertically resolved response structure. Similar anomaly signatures are observed during Eastern Pacific El Niño events (Benito-Barca et al., 2022, see, e.g., their Fig. 1g). They have furthermore been obtained from modern CMIP6 climate projections based on various climate forcing scenarios (Match and Gerber, 2022, e.g., their Fig. 1).

Finally, referring back to our initial motivation, we found clear similarities between polar vortex—ozone co-variability and year-by-year variability in zonal-mean ozone in general, as measured by the local sample standard deviation provided in Fig. 1. We may ask to what extent this allows us to constrain polar ozone anomalies during northern hemispheric winters. To do so, we consider seasonal-mean ozone for DJF from ERAI, MLS and ERA5, each interpolated on equidistant pressure levels between 1 and 300 hPa with 1 hPa vertical resolution and adjusted for linear trends across the corresponding time intervals. The observed variability in polarcap-averaged partial column ozone (PCO) then reads

$$\Delta PCO_{obs}(t) = \left\langle \int_{1 \text{ hPa}}^{300 \text{ hPa}} \delta \overline{\chi}(t, p, \phi) \, dp \right\rangle_{\phi > 60^{\circ} \text{ N}}.$$
 (5)

Based on the associated T100 regression map for ozone in the latitude-pressure plane, we reconstruct the variations that are explained by co-variability with the polar vortex,

$$\Delta PCO_{exp}(t) = \overline{T}_{100}(t) \cdot \left\langle \int_{1 \text{ hPa}}^{300 \text{ hPa}} b(p, \phi) \, dp \right\rangle_{\phi > 60^{\circ} \text{ N}}, \quad (6)$$

corresponding to the general T100 index time series modulated by a constant prefactor that depends on the individual model realization. Finally, the correlation between these two PCO anomaly time series provides a measure for the variance of ΔPCO_{obs} that is associated with seasonal polar vortex strength anomalies. The results obtained for ERAI, MLS and ERA5 are shown in Fig. 9 and Table 1, which are

Table 1. Variances of observed polar-cap-averaged partial column ozone, ΔPCO_{obs} , as defined in Eq. (5), explained by interannual variability in PCO_{exp} from Eq. (6) associated with T100 anomalies. This table extends the results presented in Fig. 9. Explained variances are provided as the squared correlation coefficients obtained from least-squares linear regressions, where minimum and maximum values were derived from the corresponding 95 % confidence intervals for the correlation coefficients based on Fisher's z transformation.

Dataset	Time range	Explained variance [%]		
		min	r^2	max
ERAI	1980–2016	28	53	72
ERA5		48	69	83
	1960–1980	21	55	79
	1980–2022	53	71	83
	2005–2020	47	78	92
MLS		63	86	95

based on the extended T100 index from ERA5. For a comprehensive analysis, we added separate computations for presatellite ERA5 data covering DJF 1960–1980.

Table 1 suggests that around 86% of polar-cap-averaged PCO variations from MLS are related to T100 co-variability. This significantly differs from ERAI, where only slightly more than half of the variability can be attributed. Explained variances for ERA5 starting from DJF 1980 turn out to be substantially higher compared with ERAI and furthermore approach the performance of MLS. The low value for the pre-satellite era in ERA5 suggests that more recent years in reanalyses are much better constrained by observational data. However, it is unclear whether the remaining differences only result from the individual model implementations, assimilation schemes and the quality of the measurements. Instead, e.g., given the growing explained variances for ERA5 with time, the findings may also suggest a much more fundamental change in the interactions between ozone and large-scale atmospheric dynamics. For example, Calvo et al. (2015) showed that stratospheric zonal wind and temperature anomalies during Arctic ozone extremes occurred mainly in recent decades due to substantial anthropogenic ozone-depleting substances, indicating that ozone chemistry has become increasingly important in governing climate vari-

To sum up, we showed that most of the interannual anomalies of polar column ozone in recent years can be attributed to wave-driven anomalous dynamics associated with the varying strength of the polar vortex. Knowledge on the mechanisms that constrain these leading modes of intrinsic ozone variability may help to understand long-term trends in response to external forcings, i.e., due to evolving concentra-

tions of ozone-depleting substances or increased greenhouse gas emissions (e.g., SPARC/IO3C/GAW, 2019). Moreover, feedbacks between anthropogenic climate change and stratospheric dynamics may cause modifications to these modes of variability. Exploring the extent to which ozone itself is involved here would be worth a closer look.

Appendix A: T100 and VT100 predictors for linear regressions

In this study, we used anomaly time series based on polar-cap-averaged zonal-mean temperature at $100\,\mathrm{hPa}$ ("T100 index") as the predictors for our linear regression analysis. In Sect. 2, we demonstrated that this index is a suitable measure for the strength of the stratospheric polar vortex. Previous literature on interannual ozone variability often focused on the zonal-mean meridional eddy heat flux $\overline{v'T'}$ at $100\,\mathrm{hPa}$ ("VT100 index") to quantify the total available wave driving of the stratosphere. For comparison, Fig. A1 provides additional regression maps for seasonal-mean temperature and ozone from ERA-Interim reanalysis data (December-February, DJF), regressed on both the T100 (DJF) and VT100 (November-January, NDJ) predictors. More details and a discussion of the results are included in Sect. 2.

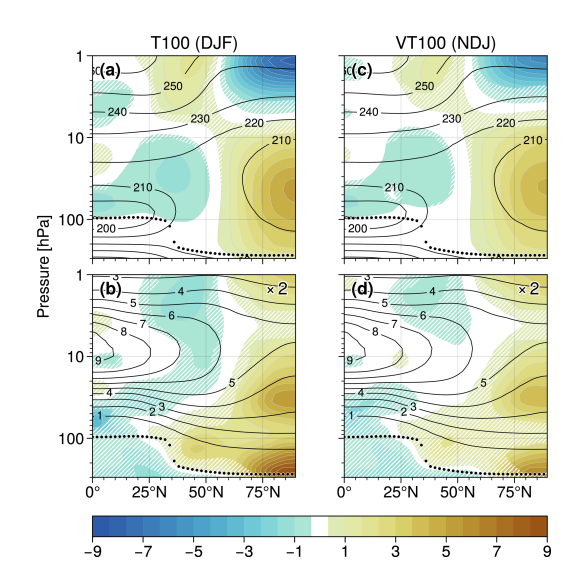


Figure A1. Interannual anomalies (seasonal means, DJF) of zonalmean temperature (in units of Kelvin, **a** and **c**) and ozone (**b** and **d**), regressed on the T100 index (DJF, **a** and **b**) and the VT100 predictor (NDJ, **c** and **d**), which are both described in Sect. 2. Note the time lag for the VT100 time series. The ozone responses (in percent) are provided relative to the DJF climatology and have been scaled by a factor of 0.5 before plotting. Black contour lines show the corresponding climatologies (in Kelvin and parts per million by volume for temperature and ozone, respectively) and hatches indicate where the regressions are not statistically significant. The thick dotted lines indicate the seasonal-mean thermal tropopause. All results were obtained from ERA-Interim reanalysis data.

Data availability. ERA-Interim data were provided by ECMWF through NCAR. They can also be downloaded from https://apps.ecmwf.int/archive-catalogue/?class=ei (ECMWF, 2023). Aura MLS version 5 data are available at https://disc.gsfc.nasa.gov (Livesey et al., 2022). Data from Hersbach et al. (2019) were downloaded from the Copernicus Climate Change Service (C3S) Climate Data Store. Our study contains modified Copernicus Climate Change Service information 2023. Neither the European Commission nor ECMWF is responsible for any use that may be made of the Copernicus information or data it contains.

Author contributions. FH performed the analyses, supervised by HG and TB. TB initiated the project and processed the ERA-Interim reanalyses. FP provided the MLS observational data. FH wrote the first draft of the paper. All authors contributed in interpreting the results and improving the paper.

Competing interests. The contact author has declared that none of the authors has any competing interests.

Disclaimer. Publisher's note: Copernicus Publications remains neutral with regard to jurisdictional claims in published maps and institutional affiliations.

Acknowledgements. We acknowledge valuable suggestions by two anonymous reviewers that significantly helped to improve this paper. We thank Y. Desille for research on polar vortex–ozone co-variability from modern reanalyses and H. von Heydebrand for extending these studies to chemistry–climate models. We further thank the MLS team for providing the ozone satellite observation data. FH appreciates helpful suggestions by E. Gerber. Throughout this study, we used color codings based on Color-Brewer 2.0 (Brewer, 2022) and Scientific Colour Maps (Crameri et al., 2020; Crameri, 2022). We appreciate the features provided by xarray (Hoyer and Hamman, 2017; Hoyer et al., 2022) and Pro-Plot (Davis, 2022).

Financial support. This research has been supported by the Deutsche Forschungsgemeinschaft (DFG, German Research Foundation) – TRR 301 – project ID 428312742 ("The tropopause region in a changing atmosphere").

This open-access publication was funded by Ludwig-Maximilians-Universität München.

Review statement. This paper was edited by Gabriele Stiller and reviewed by two anonymous referees.

References

- Abalos, M., Legras, B., Ploeger, F., and Randel, W. J.: Evaluating the advective Brewer-Dobson circulation in three reanalyses for the period 1979–2012, J. Geophys. Res.-Atmos., 120, 7534–7554, https://doi.org/10.1002/2015JD023182, 2015.
- Adam, O., Grise, K. M., Staten, P., Simpson, I. R., Davis, S. M., Davis, N. A., Waugh, D. W., Birner, T., and Ming, A.: The TropD software package (v1): standardized methods for calculating tropical-width diagnostics, Geosci. Model Dev., 11, 4339– 4357, https://doi.org/10.5194/gmd-11-4339-2018, 2018.
- Albers, J. R., Perlwitz, J., Butler, A. H., Birner, T., Kiladis, G. N., Lawrence, Z. D., Manney, G. L., Langford, A. O., and Dias, J.: Mechanisms governing interannual variability of stratosphere-totroposphere ozone transport, J. Geophys. Res.-Atmos., 123, 234– 260, https://doi.org/10.1002/2017JD026890, 2018.
- Andrews, D. G., Holton, J. R., and Leovy, C. B.: Middle atmosphere dynamics, International Geophysics, vol. 40, Academic Press, ISBN 9780120585762, 1987.
- Bahramvash Shams, S., Walden, V. P., Hannigan, J. W., Randel, W. J., Petropavlovskikh, I. V., Butler, A. H., and de la Cámara, A.: Analyzing ozone variations and uncertainties at high latitudes during sudden stratospheric warming events using MERRA-2, Atmos. Chem. Phys., 22, 5435–5458, https://doi.org/10.5194/acp-22-5435-2022, 2022.
- Baldwin, M. P., Birner, T., Brasseur, G., Burrows, J., Butchart, N., Garcia, R., Geller, M., Gray, L., Hamilton, K., Harnik, N., Hegglin, M. I., Langematz, U., Robock, A., Sato, K., and Scaife, A. A.: 100 years of progress in understanding the stratosphere and mesosphere, Meteor. Mon., 59, 27.1–27.62, https://doi.org/10.1175/AMSMONOGRAPHS-D-19-0003.1, 2019.
- Baldwin, M. P., Ayarzagüena, B., Birner, T., Butchart, N., Butler, A. H., Charlton-Perez, A. J., Domeisen, D. I. V., Garfinkel, C. I., Garny, H., Gerber, E. P., Hegglin, M. I., Langematz, U., and Pedatella, N. M.: Sudden stratospheric warmings, Rev. Geophys., 59, e2020RG000708, https://doi.org/10.1029/2020RG000708, 2021.
- Bandoro, J., Solomon, S., Donohoe, A., Thompson, D. W. J., and Santer, B. D.: Influences of the Antarctic ozone hole on southern hemispheric summer climate change, J. Climate, 27, 6245–6264, https://doi.org/10.1175/JCLI-D-13-00698.1, 2014.
- Barnes, P. W., Robson, T. M., Neale, P. J., Williamson, C. E., Zepp, R. G., Madronich, S., Wilson, S. R., Andrady, A. L., Heikkilä, A. M., Bernhard, G. H., Bais, A. F., Neale, R. E., Bornman, J. F., Jansen, M. A. K., Klekociuk, A. R., Martinez-Abaigar, J., Robinson, S. A., Wang, Q.-W., Banaszak, A. T., Häder, D.-P., Hylander, S., Rose, K. C., Wängberg, S.-Å., Foereid, B., Hou, W.-C., Ossola, R., Paul, N. D., Ukpebor, J. E., Andersen, M. P. S., Longstreth, J., Schikowski, T., Solomon, K. R., Sulzberger, B., Bruckman, L. S., Pandey, K. K., White, C. C., Zhu, L., Zhu, M., Aucamp, P. J., Liley, J. B., McKenzie, R. L., Berwick, M., Byrne, S. N., Hollestein, L. M., Lucas, R. M., Olsen, C. M., Rhodes, L. E., Yazar, S., and Young, A. R.: Environmental effects of stratospheric ozone depletion, UV radiation, and interactions with climate change: UNEP Environmental Effects Assessment Panel, Update 2021, Photochem. Photobiol. S., 21, 275-301, https://doi.org/10.1007/s43630-022-00176-5, 2022.

- Bell, B., Hersbach, H., Simmons, A., Berrisford, P., Dahlgren, P., Horányi, A., Muñoz-Sabater, J., Nicolas, J., Radu, R., Schepers, D., Soci, C., Villaume, S., Bidlot, J.-R., Haimberger, L., Woollen, J., Buontempo, C., and Thépaut, J.-N.: The ERA5 global reanalysis: preliminary extension to 1950, Q. J. Roy. Meteor. Soc., 147, 4186–4227, https://doi.org/10.1002/qj.4174, 2021.
- Benito-Barca, S., Calvo, N., and Abalos, M.: Driving mechanisms for the El Niño-Southern Oscillation impact on stratospheric ozone, Atmos. Chem. Phys., 22, 15729–15745, https://doi.org/10.5194/acp-22-15729-2022, 2022.
- Brasseur, G. P. and Solomon, S.: Aeronomy of the middle atmosphere. Chemistry and physics of the stratosphere and mesosphere, 3rd edn., Springer Dordrecht, https://doi.org/10.1007/1-4020-3824-0, 2005.
- Brewer, C. A.: ColorBrewer 2.0, https://colorbrewer2.org (last access: 6 September 2023), 2022.
- Butchart, N.: The Brewer-Dobson circulation, Rev. Geophys., 52, 157–184, https://doi.org/10.1002/2013RG000448, 2014.
- Butler, A. H., Sjoberg, J. P., Seidel, D. J., and Rosenlof, K. H.: A sudden stratospheric warming compendium, Earth Syst. Sci. Data, 9, 63–76, https://doi.org/10.5194/essd-9-63-2017, 2017.
- Calvo, N., Polvani, L. M., and Solomon, S.: On the surface impact of Arctic stratospheric ozone extremes, Environ. Res. Lett., 10, 094003, https://doi.org/10.1088/1748-9326/10/9/094003, 2015.
- Chiodo, G. and Polvani, L. M.: Reduced southern hemispheric circulation response to quadrupled CO₂ due to stratospheric ozone feedback, Geophys. Res. Lett., 44, 465–474, https://doi.org/10.1002/2016GL071011, 2017.
- Chiodo, G. and Polvani, L. M.: The response of the ozone layer to quadrupled CO₂ concentrations: implications for climate, J. Climate, 32, 7629–7642, https://doi.org/10.1175/JCLI-D-19-0086.1, 2019.
- Chiodo, G., Polvani, L. M., Marsh, D. R., Stenke, A., Ball, W., Rozanov, E., Muthers, S., and Tsigaridis, K.: The response of the ozone layer to quadrupled CO₂ concentrations, J. Climate, 31, 3893–3907, https://doi.org/10.1175/JCLI-D-17-0492.1, 2018.
- Crameri, F.: Scientific colour maps, Zenodo [code], https://doi.org/10.5281/zenodo.1243862, 2022.
- Crameri, F., Shephard, G. E., and Heron, P. J.: The misuse of colour in science communication, Nat. Commun., 11, 5444, https://doi.org/10.1038/s41467-020-19160-7, 2020.
- Davis, L. L. B.: ProPlot, Zenodo [code], https://doi.org/10.5281/zenodo.3873878, 2022.
- Davis, S. M., Hegglin, M. I., Dragani, R., Fujiwara, M., Harada, Y., Kobayashi, C., Long, C., Manney, G. L., Nash, E. R., Potter, G. L., Tegtmeier, S., Wang, T., Wargan, K., and Wright, J. S.: Overview of ozone and water vapour, in: SPARC Reanalysis Intercomparison Project (S-RIP) Final Report, edited by: Fujiwara, M., Manney, G. L., Gray, L. J., and Wright, J. S., SPARC Report No. 10, WCRP-6/2021, 123–164, https://doi.org/10.17874/800dee57d13, 2022.
- de la Cámara, A., Abalos, M., and Hitchcock, P.: Changes in stratospheric transport and mixing during sudden stratospheric warmings, J. Geophys. Res.-Atmos., 123, 3356–3373, https://doi.org/10.1002/2017JD028007, 2018a.
- de la Cámara, A., Abalos, M., Hitchcock, P., Calvo, N., and Garcia, R. R.: Response of Arctic ozone to sudden stratospheric warmings, Atmos. Chem. Phys., 18, 16499–16513, https://doi.org/10.5194/acp-18-16499-2018, 2018b.

- Dee, D. P., Uppala, S. M., Simmons, A. J., Berrisford, P., Poli, P., Kobayashi, S., Andrae, U., Balmaseda, M. A., Balsamo, G., Bauer, P., Bechtold, P., Beljaars, A. C. M., van de Berg, L., Bidlot, J., Bormann, N., Delsol, C., Dragani, R., Fuentes, M., Geer, A. J., Haimberger, L., Healy, S. B., Hersbach, H., Hólm, E. V., Isaksen, L., Kållberg, P., Köhler, M., Matricardi, M., McNally, A. P., Monge-Sanz, B. M., Morcrette, J.-J., Park, B.-K., Peubey, C., de Rosnay, P., Tavolato, C., Thépaut, J.-N., and Vitart, F.: The ERA-Interim reanalysis: configuration and performance of the data assimiliation system, Q. J. Roy. Meteor. Soc., 137, 553–597, https://doi.org/10.1002/qj.828, 2011.
- Dietmüller, S., Ponater, M., and Sausen, R.: Interactive ozone induces a negative feedback in CO₂-driven climate change simulations, J. Geophys. Res.-Atmos., 119, 1796–1805, https://doi.org/10.1002/2013JD020575, 2014.
- Domeisen, D. I. V., Butler, A. H., Charlton-Perez, A. J., Ayarzagüena, B., Baldwin, M. P., Dunn-Sigouin, E., Furtado, J. C., Garfinkel, C. I., Hitchcock, P., Karpechko, A. Y., Kim, H., Knight, J., Lang, A. L., Lim, E.-P., Marshall, A., Roff, G., Schwartz, C., Simpson, I. R., Son, S.-W., and Taguchi, M.: The role of the stratosphere in subseasonal to seasonal prediction: 2. Predictability arising from stratosphere-troposphere coupling, J. Geophys. Res.-Atmos., 125, e2019JD030923, https://doi.org/10.1029/2019JD030923, 2020.
- Dragani, R.: On the quality of the ERA-Interim ozone reanalyses: comparisons with satellite data, Q. J. Roy. Meteor. Soc., 137, 1312–1326, https://doi.org/10.1002/qj.821, 2011.
- ECMWF: Archive Catalogue, European Centre for Medium-Range Weather Forecasts [data set], https://apps.ecmwf.int/archive-catalogue/?class=ei (last access: 6 September 2023), 2023
- Friedel, M., Chiodo, G., Stenke, A., Domeisen, D. I. V., Fueglistaler, S., Anet, J. G., and Peter, T.: Springtime Arctic ozone depletion forces northern hemisphere climate anomalies, Nat. Geosci., 15, 541–547, https://doi.org/10.1038/s41561-022-00974-7, 2022a.
- Friedel, M., Chiodo, G., Stenke, A., Domeisen, D. I. V., and Peter, T.: Effects of Arctic ozone on the stratospheric spring onset and its surface impact, Atmos. Chem. Phys., 22, 13997–14017, https://doi.org/10.5194/acp-22-13997-2022, 2022b.
- Fu, Q., Solomon, S., and Lin, P.: On the seasonal dependence of tropical lower-stratospheric temperature trends, Atmos. Chem. Phys., 10, 2643–2653, https://doi.org/10.5194/acp-10-2643-2010, 2010.
- Fusco, A. C. and Salby, M. L.: Interannual variations of total ozone and their relationship to variations of planetary wave activity, J. Climate, 12, 1619–1629, https://doi.org/10.1175/1520-0442(1999)012<1619:IVOTOA>2.0.CO;2, 1999.
- Garcia, R. R. and Hartmann, D. L.: The role of planetary waves in the maintenance of the zonally averaged ozone distribution of the upper stratosphere, J. Atmos. Sci., 37, 2248–2264, https://doi.org/10.1175/1520-0469(1980)037<2248:TROPWI>2.0.CO;2, 1980.
- Gettelman, A., Hoor, P., Pan, L. L., Randel, W. J., Hegglin, M. I., and Birner, T.: The extratropical upper troposphere and lower stratosphere, Rev. Geophys., 49, RG3003, https://doi.org/10.1029/2011RG000355, 2011.
- Grise, K. M., Thompson, D. W. J., and Birner, T.: A global survey of static stability in the stratosphere and upper troposphere, J. Cli-

- mate, 23, 2275–2292, https://doi.org/10.1175/2009JCLI3369.1, 2010.
- Hartmann, D. L. and Garcia, R. R.: A mechanistic model of ozone transport by planetary waves in the stratosphere, J. Atmos. Sci., 36, 350–364, https://doi.org/10.1175/1520-0469(1979)036<0350:AMMOOT>2.0.CO:2, 1979.
- Haynes, P. H., McIntyre, M. E., Shepherd, T. G., Marks, C. J., and Shine, K. P.: On the "downward control" of extratropical diabatic circulations by eddy-induced mean zonal forces, J. Atmos. Sci., 48, 651–678, https://doi.org/10.1175/1520-0469(1991)048<0651:OTCOED>2.0.CO;2, 1991.
- Hersbach, H., Bell, B., Berrisford, P., Biavati, G., Horányi, A., Muñoz-Sabater, J., Nicolas, J., Peubey, C., Radu, R., Rozum, I., Schepers, D., Simmons, A., Soci, C., Dee, D., and Thépaut, J.-N.: ERA5 monthly averaged data on pressure levels from 1959 to present, Copernicus Climate Change Service (C3S) Climate Data Store (CDS), https://doi.org/10.24381/cds.6860a573, 2019.
- Hersbach, H., Bell, B., Berrisford, P., Hirahara, S., Horányi, A., Muñoz-Sabater, J., Nicolas, J., Peubey, C., Radu, R., Schepers, D., Simmons, A., Soci, C., Abdalla, S., Abellan, X., Balsamo, G., Bechtold, P., Biavati, G., Bidlot, J., Bonavita, M., de Chiara, G., Dahlgren, P., Dee, D., Diamantakis, M., Dragani, R., Flemming, J., Forbes, R., Fuentes, M., Geer, A., Haimberger, L., Healy, S., Hogan, R. J., Hólm, E., Janisková, M., Keeley, S., Laloyaux, P., Lopez, P., Lupu, C., Radnoti, G., de Rosnay, P., Rozum, I., Vamborg, F., Villaume, S., and Thépaut, J.-N.: The ERA5 global reanalysis, Q. J. Roy. Meteor. Soc., 146, 1999–2049, https://doi.org/10.1002/qj.3803, 2020.
- Hitchcock, P., Shepherd, T. G., and Yoden, S.: On the approximation of local and linear radiative damping in the middle atmosphere, J. Atmos. Sci., 67, 2070–2085, https://doi.org/10.1175/2009JAS3286.1, 2010.
- Hong, H.-J. and Reichler, T.: Local and remote response of ozone to Arctic stratospheric circulation extremes, Atmos. Chem. Phys., 21, 1159–1171, https://doi.org/10.5194/acp-21-1159-2021, 2021.
- Hoyer, S. and Hamman, J. J.: xarray: N-D labeled arrays and datasets in Python, Journal of Open Research Software, 5, 10, https://doi.org/10.5334/jors.148, 2017.
- Hoyer, S., Roos, M., Hamman, J., Magin, J., Cherian, D., Fitzgerald, C., Hauser, M., Fujii, K., Maussion, F., Imperiale, G., Clark, S., Kleeman, A., Nicholas, T., Kluyver, T., Westling, J., Munroe, J., Amici, A., Barghini, A., Banihirwe, A., Bell, R., Hatfield-Dodds, Z., Abernathey, R., Bovy, B., Omotani, J., Mühlbauer, K., Roszko, M. K., and Wolfram, P. J.: xarray, Zenodo [code], https://doi.org/10.5281/zenodo.598201, 2022.
- IPCC: Climate change 2021: The physical science basis: Contribution of working group I to the sixth assessment report of the Intergovernmental Panel on Climate Change, Cambridge University Press, https://doi.org/10.1017/9781009157896, 2021.
- Ivy, D. J., Solomon, S., Calvo, N., and Thompson, D. W. J.: Observed connections of Arctic stratospheric ozone extremes to northern hemisphere surface climate, Environ. Res. Lett., 12, 024004, https://doi.org/10.1088/1748-9326/aa57a4, 2017.
- Kinnersley, J. S. and Tung, K.-K.: Modeling the global interannual variability of ozone due to the equatorial QBO and to extratropical planetary wave variability, J. Atmos. Sci., 55, 1417–1428, https://doi.org/10.1175/1520-0469(1998)055<1417:MTGIVO>2.0.CO;2, 1998.

- Konopka, P., Grooß, J.-U., Plöger, F., and Müller, R.: Annual cycle of horizontal in-mixing into the lower tropical stratosphere, J. Geophys. Res., 114, D19111, https://doi.org/10.1029/2009JD011955, 2009.
- Lait, L. R.: An alternative form for potential vorticity, J. Atmos. Sci., 51, 1754–1759, https://doi.org/10.1175/1520-0469(1994)051<1754:AAFFPV>2.0.CO;2, 1994.
- Leovy, C. B., Sun, C.-R., Hitchman, M. H., Remsberg, E. E., Russell III, J. M., Gordley, L. L., Gille, J. C., and Lyjak, L. V.: Transport of ozone in the middle stratosphere: evidence for planetary wave breaking, J. Atmos. Sci., 42, 230–244, https://doi.org/10.1175/1520-0469(1985)042<0230:TOOITM>2.0.CO;2, 1985.
- Livesey, N. J., Read, W. G., Wagner, P. A., Froidevaux, L., Santee, M. L., Schwartz, M. J., Lambert, A., Millán Valle, L. F., Pumphrey, H. C., Manney, G. L., Fuller, R. A., Jarnot, R. F., Knosp, B. W., and Lay, R. R.: Earth Observing System (EOS) Aura Microwave Limb Sounder (MLS) version 5.0x level 2 and 3 data quality and description document, Version 5.0–1.1a, JPL D-105336 Rev. B, https://disc.gsfc.nasa.gov (last access: 6 September 2023), 2022.
- Lubis, S. W., Silverman, V., Matthes, K., Harnik, N., Omrani, N.-E., and Wahl, S.: How does downward planetary wave coupling affect polar stratospheric ozone in the Arctic winter stratosphere?, Atmos. Chem. Phys., 17, 2437–2458, https://doi.org/10.5194/acp-17-2437-2017, 2017.
- Ma, J., Waugh, D. W., Douglass, A. R., Kawa, S. R., Newman, P. A., Pawson, S., Stolarski, R., and Lin, S. J.: Interannual variability of stratospheric trace gases: the role of extratropical wave driving, Q. J. Roy. Meteor. Soc., 130, 2459–2474, https://doi.org/10.1256/qj.04.28, 2004.
- Match, A. and Gerber, E. P.: Tropospheric expansion under global warming reduces tropical lower stratospheric ozone, Geophys. Res. Lett., 49, e2022GL099463, https://doi.org/10.1029/2022GL099463, 2022.
- Monge-Sanz, B. M., Birner, T., Chabrillat, S., Diallo, M., Haenel, F., Konopka, P., Legras, B., Ploeger, F., Reddmann, T., Stiller, G., Wright, J. S., Abalos, M., Boenisch, H., Davis, S., Garny, H., Hitchcock, P., Miyazaki, K., Roscoe, H. K., Sato, K., Tao, M., and Waugh, D.: Brewer-Dobson circulation, in: SPARC Reanalysis Intercomparison Project (S-RIP) Final Report, edited by: Fujiwara, M., Manney, G. L., Gray, L. J., and Wright, J. S., SPARC Report No. 10, WCRP-6/2021, 165–220, https://doi.org/10.17874/800dee57d13, 2022.
- Newman, P. A., Nash, E. R., and Rosenfield, J. E.: What controls the temperature of the Arctic stratosphere during the spring?, J. Geophys. Res.-Atmos., 106, 19999–20010, https://doi.org/10.1029/2000JD000061, 2001.
- Nowack, P. J., Abraham, N. L., Maycock, A. C., Braesicke, P., Gregory, J. M., Joshi, M. M., Osprey, A., and Pyle, J. A.: A large ozone-circulation feedback and its implications for global warming assessments, Nat. Clim. Change, 5, 41–45, https://doi.org/10.1038/nclimate2451, 2015.
- Nowack, P. J., Abraham, N. L., Braesicke, P., and Pyle, J. A.: The impact of stratospheric ozone feedbacks on climate sensitivity estimates, J. Geophys. Res.-Atmos., 123, 4630–4641, https://doi.org/10.1002/2017JD027943, 2018.
- Plumb, R. A.: Stratospheric transport, J. Meteorol. Soc. Jpn. Ser. II, 80, 793–809, https://doi.org/10.2151/jmsj.80.793, 2002.

- Polvani, L. M. and Waugh, D. W.: Upward wave activity flux as a precursor to extreme stratospheric events and subsequent anomalous surface weather regimes, J. Climate, 17, 3548–3554, https://doi.org/10.1175/1520-0442(2004)017<3548:UWAFAA>2.0.CO;2, 2004.
- Randel, W. J., Wu, F., and Stolarski, R.: Changes in column ozone correlated with the stratospheric EP flux, J. Meteorol. Soc. Jpn., 80, 849–862, https://doi.org/10.2151/jmsj.80.849, 2002.
- Smith, K. L. and Polvani, L. M.: The surface impacts of Arctic stratospheric ozone anomalies, Environ. Res. Lett., 9, 074015, https://doi.org/10.1088/1748-9326/9/7/074015, 2014.
- Son, S.-W., Tandon, N. F., and Polvani, L. M.: The fine-scale structure of the global tropopause derived from COSMIC GPS radio occultation measurements, J. Geophys. Res.-Atmos., 116, D20113, https://doi.org/10.1029/2011JD016030, 2011.
- Son, S.-W., Purich, A., Hendon, H. H., Kim, B.-M., and Polvani, L. M.: Improved seasonal forecast using ozone hole variability?, Geophys. Res. Lett., 40, 6231–6235, https://doi.org/10.1002/2013GL057731, 2013.
- SPARC/IO3C/GAW: SPARC/IO3/GAW report on long-term ozone trends and uncertainties in the stratosphere: SPARC Report No. 9, GAW Report No. 241, WCRP-17/2018, https://doi.org/10.17874/f899e57a20b, 2019.
- Strahan, S. E., Douglass, A. R., and Steenrod, S. D.: Chemical and dynamical impacts of stratospheric sudden warmings on Arctic ozone variability, J. Geophys. Res.-Atmos., 121, 11836–11851, https://doi.org/10.1002/2016JD025128, 2016.
- Tung, K. K.: Nongeostrophic theory of zonally averaged circulation. Part I: Formulation, J. Atmos. Sci., 43, 2600–2618, https://doi.org/10.1175/1520-0469(1986)043<2600:NTOZAC>2.0.CO;2, 1986.
- von Heydebrand, H.: Interannual ozone variability in the Northern Hemisphere from coupled chemistry-climate models, Bachelor's thesis, Faculty of Physics, Ludwig-Maximilians-Universität München, Munich, Germany, 2022.
- Wargan, K. and Coy, L.: Strengthening of the tropopause inversion layer during the 2009 sudden stratospheric warming: a MERRA-2 study, J. Atmos. Sci., 73, 1871–1887, https://doi.org/10.1175/JAS-D-15-0333.1, 2016.

- Waters, J. W., Froidevaux, L., Harwood, R. S., Jarnot, R. F., Pickett, H. M., Read, W. G., Siegel, P. H., Cofield, R. E., Filipiak, M. J., Flower, D. A., Holden, J. R., Lau, G. K., Livesey, N. J., Manney, G. L., Pumphrey, H. C., Santee, M. L., Wu, D. L., Cuddy, D. T., Lay, R. R., Loo, M. S., Perun, V. S., Schwartz, M. J., Stek, P. C., Thurstans, R. P., Boyles, M. A., Chandra, K. M., Chavez, M. C., Chen, G.-S., Chudasama, B. V., Dodge, R., Fuller, R. A., Girard, M. A., Jiang, J. H., Jiang, Y., Knosp, B. W., LaBelle, R. C., Lam, J. C., Lee, K. A., Miller, D., Oswald, J. E., Patel, N. C., Pukala, D. M., Quintero, O., Scaff, D. M., van Snyder, W., Tope, M. C., Wagner, P. A., and Walch, M. J.: The Earth observing system microwave limb sounder (EOS MLS) on the aura satellite, IEEE T. Geosci. Remote, 44, 1075–1092, https://doi.org/10.1109/TGRS.2006.873771, 2006.
- Weber, M., Dhomse, S., Wittrock, F., Richter, A., Sinnhuber, B.-M., and Burrows, J. P.: Dynamical control of NH and SH winter/spring total ozone from GOME observations in 1995–2002, Geophys. Res. Lett., 30, 1583, https://doi.org/10.1029/2002GL016799, 2003.
- Weber, M., Dikty, S., Burrows, J. P., Garny, H., Dameris, M., Kubin, A., Abalichin, J., and Langematz, U.: The Brewer-Dobson circulation and total ozone from seasonal to decadal time scales, Atmos. Chem. Phys., 11, 11221–11235, https://doi.org/10.5194/acp-11-11221-2011, 2011.
- WMO: Meteorology a three-dimensional science: Second session of the Commission for Aerology, WMO Bulletin, 6, 134–138, 1957.
- WMO: Scientific assessment of ozone depletion: 2022, GAW Report No. 278, Geneva, https://ozone.unep.org (last access: 6 September 2023), 2022.
- Young, P. J., Rosenlof, K. H., Solomon, S., Sherwood, S. C., Fu, Q., and Lamarque, J.-F.: Changes in stratospheric temperatures and their implications for changes in the Brewer-Dobson circulation, 1979–2005, J. Climate, 25, 1759–1772, https://doi.org/10.1175/2011JCLI4048.1, 2012.

Chapter 3

Paper II

Publication details

Title: Probing the Suitability of Meridional Stratospheric Ozone

Gradients for Inferring Interannual Variability and Trends

of the Subtropical Jet Stream

Authors: Frederik Harzer, Hella Garny, Sean Davis and Thomas Birner

Journal: Journal of Climate

Publisher: American Meteorological Society

Publication date: May 20, 2025 (online)

DOI: https://doi.org/10.1175/JCLI-D-24-0530.1

Author contributions

FH performed the analyses and wrote the first draft of the paper. He was supervised by HG and TB. SD provided the SWOOSH dataset and the post-processed CCMI climate model output. All authors contributed to the interpretation of the results and helped to improve the paper.

Copyright information

F. Harzer et al. (2025). "Probing the Suitability of Meridional Stratospheric Ozone Gradients for Inferring Interannual Variability and Trends of the Subtropical Jet Stream". In: J. Climate 38, pp. 2571–2588. DOI: 10.1175/JCLI-D-24-0530.1

© American Meteorological Society. Used with permission.

36 3. Paper II

The copyright information printed below is available at https://www.ametsoc.org/ams/publications/ethical-guidelines-and-ams-policies/ams-copyright-policy/ and is hereby pointed to:

"© Copyright [2025] American Meteorological Society (AMS). For permission to reuse any portion of this Work, please contact permissions@ametsoc.org. Any use of material in this Work that is determined to be 'fair use' under Section 107 of the U.S. Copyright Act (17 U.S. Code § 107) or that satisfies the conditions specified in Section 108 of the U.S. Copyright Act (17 USC § 108) does not require the AMS's permission. Republication, systematic reproduction, posting in electronic form, such as on a website or in a searchable database, or other uses of this material, except as exempted by the above statement, requires written permission or a license from the AMS. All AMS journals and monograph publications are registered with the Copyright Clearance Center (https://www.copyright.com). Additional details are provided in the AMS Copyright Policy statement, available on the AMS website (https://www.ametsoc.org/PUBSCopyrightPolicy)."

Frederik Harzer, a Hella Garny, b,a Sean Davis, and Thomas Birner, blank birner, b,a sean Davis, and Thomas Birner, b,a sean Davis, b,a sean D

^a Meteorological Institute, Ludwig-Maximilians-Universität München, Munich, Germany ^b Institute of Atmospheric Physics, Deutsches Zentrum für Luft- und Raumfahrt, Oberpfaffenhofen, Germany ^c NOAA/Chemical Sciences Laboratory, Boulder, Colorado

(Manuscript received 17 September 2024, in final form 31 January 2025, accepted 18 February 2025)

ABSTRACT: Atmospheric jet streams belong to the most fundamental elements of the global general circulation system and are susceptible to climate change. Jet stream variability in our present climate is usually studied from modern reanalysis products, although uncertainties arise due to insufficiently strong constraints of the underlying global wind field by the available observational records, especially concerning their long-term trends. This motivates the use of observation-based metrics to track dynamical variability and historical trends. Here, we investigate how the zonal-mean ozone structure can be used to indirectly infer changes in the strength and latitudinal position of the subtropical jet streams (STJs). We mainly consider the winter-mean ozone distribution and analyze different diagnostics that track anomalies of the sharp ozone gradients near the subtropical tropopause, based on either vertically resolved or total-column ozone (TCO) fields. Using ERA5 reanalysis output, we find significant correspondence of these sharp ozone gradients with the STJ's strength and location, with the jet acting as a tracer transport barrier and, hence, governing wave-induced horizontal ozone transport across the jet core. The ozone gradient metrics obtained from vertically resolved ozone observations agree well with ERA5 in more recent years when densely sampled satellite measurements were included. We furthermore obtain mostly consistent historical trend signals from both conventional STJ metrics from reanalyses and more independent TCO records. Chemistry–Climate Model Initiative phase 1 (CCMI-1) and CMIP6 climate simulations suggest a strong correspondence between changes in subtropical ozone gradient maxima and projected STJ trends under different climate forcing scenarios.

KEYWORDS: Atmospheric circulation; Jets; Ozone; Interannual variability; Trends

1. Introduction

Climate research has provided evidence for robust climate change signatures of the large-scale atmospheric general circulation as the response to increasing levels of greenhouse gas concentrations (e.g., Shaw et al. 2024; Lee et al. 2021; Schneider 2006). In particular, generations of climate projections suggest a robust strengthening of the strong eastward winds located along the subtropical tropopause break in both hemispheres, usually referred to as the subtropical jet streams (STJs), which is consistent with enhanced meridional temperature gradients in the subtropical upper troposphere and lower stratosphere (UTLS) under climate change (e.g., Vallis et al. 2015; Shaw and Miyawaki 2024). Changes in the STJ strength and position further play a key role to drive changes in the (lower) stratospheric circulation, e.g., via regulating wave driving of the shallow branch of the stratospheric Brewer-Dobson circulation and quasihorizontal transport

Openotes content that is immediately available upon publication as open access.

© Supplemental information related to this paper is available at the Journals Online website: https://doi.org/10.1175/JCLI-D-24-0530.s1.

 ${\it Corresponding \ author.} \ {\it Frederik \ Harzer, frederik.harzer@physik.lmu.de}$

in the UTLS region (Shepherd and McLandress 2011; Abalos and de la Cámara 2020).

The STJs also have been discussed to provide a measure of the latitudinal extent of the tropical belt, albeit their covariability with the tropical overturning Hadley circulation turned out to be rather limited (Staten et al. 2018; Menzel et al. 2019, 2024). Furthermore, the STJ is known to be dynamically linked with the eddy-driven jet (EDJ) stream in the midlatitudes in both hemispheres (e.g., Lee and Kim 2003). This correspondence is clearly reflected, e.g., by the leading mode of intrinsic extratropical variability, which corresponds to latitudinal shifts in the location of the EDJ that project onto the strength of the STJ (Thompson and Wallace 1998, 2000; Limpasuvan and Hartmann 1999). Consistent with the STJ response, robust evidence was found for the poleward shifting of the EDJ in both hemispheres and the strengthening of the Austral midlatitude jet under climate change, with potential implications on the hemispheric storm tracks and extreme synoptic weather events (e.g., Woollings 2016; Shaw 2019; Zappa 2019).

Climate change signals, spanning the last few decades, have started to emerge from historical climate variability (e.g., Totz et al. 2018; Chemke and Yuval 2023; Woollings et al. 2023). The associated wind field variations characterizing the large-scale circulation patterns are often studied using recent reanalysis products that provide highly resolved geophysical model data and that benefit from assimilation through meteorological observations. These wind field components are effectively constrained by temperature through the thermal wind relation, but this constraint may not be sufficiently

DOI: 10.1175/JCLI-D-24-0530.1

© 2025 American Meteorological Society. This published article is licensed under the terms of the default AMS reuse license. For information regarding reuse of this content and general copyright information, consult the AMS Copyright Policy (www.ametsoc.org/PUBSReuseLicenses).

strong for long-term trends and the lack of broadly distributed and regular wind measurements prevents more accurate wind assimilation. Long et al. (2017, 2022) assessed this zonal wind and temperature output from reanalyses and especially for the more recent reanalysis products found overall good agreement, with substantial improvements due to new observational data and advanced measurement systems that became available over time. However, the authors pointed out considerable uncertainties in long-term trend evaluation from reanalyses due to changing observational constraints over time and different procedures to assimilate the observational data. Examining historical Hadley circulation trends, Grise et al. (2019) further emphasized that substantial trend uncertainties are caused by large intrinsic variability in combination with the still rather narrow time frame considered for historical trend analyses. In contrast, interannual atmospheric variability commonly features more consistent signals across datasets and therefore should be less affected by systematic biases in the reanalysis data. This highlights the relevance of modern reanalyses for understanding the atmosphere's internal mechanisms and interconnections from the perspective of both state-of-the-art atmospheric modeling and various types of global observations.

Additional observation-based metrics of jet stream variability may account for some of the above issues and may help to improve the evaluation of relevant general circulation features from reanalysis data. In particular, trend uncertainties may be reduced by choosing indirect metrics that feature reduced intrinsic variability and by using high-quality observational data that minimize inconsistencies due to the measurement setup and during data processing. Here, we propose exploiting atmospheric trace gas distributions to derive tracerbased diagnostics of variability and long-term circulation change. In particular, we consider the ozone distribution in the UTLS region, which is known to be shaped by the transport barrier associated with the STJ and has been found to not be affected much by chemistry in the UTLS. Hudson et al. (2003, 2006) and Hudson (2012) previously used the correspondence between characteristics in the structure of total-column ozone (TCO) and the locations of the atmospheric jets in the Northern Hemisphere to indirectly detect circulation trends. Davis et al. (2018) discussed the limitations of TCO as a tropical width metric due to the generally weak meridional TCO gradients, although they did not examine vertically resolved ozone metrics or TCO-based metrics during seasons with the strongest gradients (e.g., boreal winter).

In this study, we present a class of ozone metrics intended for investigations of jet stream variability in the past climate based on observational data but also applicable to future climate projections by climate models. These metrics are derived from the strong meridional gradients of the zonal-mean ozone distribution in the STJ regions and can be used with both vertically resolved ozone fields as well as TCO profiles. Section 2 lists the data and methods used in this work, and section 3 describes the methodology for computing the ozone-based diagnostics. In section 4, we use data from the fifth major global reanalysis produced by ECMWF (ERA5) to discuss the physical background of the statistical

correspondence between zonal-mean ozone and STJ variability. The features and limitations of applying the proposed ozone gradient metrics to observational data are explored in section 5 using vertically resolved ozone observations and TCO records. Finally, in section 6, we compare trend projections for STJ and ozone variability based on the Chemistry–Climate Model Initiative phase 1 (CCMI-1) and phase 6 of the Coupled Model Intercomparison Project (CMIP6) climate simulations. Section 7 contains the summary and discussion of our results.

2. Data and methods

a. Data

We use monthly averaged, zonal-mean ERA5 atmospheric reanalysis data for the years 1979–2023, which was provided on 37 pressure levels between 1 and 1000 hPa with 1° meridional resolution (Hersbach et al. 2020, 2023a,b). In ERA5, a linear ozone parameterization scheme by Cariolle and Teyssèdre (2007) is implemented (ECMWF 2016). Despite the known limitations due to modeling and data assimilation, which require a careful evaluation of the reanalysis output, ERA5 was shown to perform reasonably well in reproducing the observed variability in the vertically resolved ozone distribution (Davis et al. 2022).

For comparing historical STJ and EDJ trends, we also use monthly mean data from three additional reanalyses: combined CFSR (through 2010) and CFSv2 (from 2010), Japanese Reanalysis for three quarters of a century (JRA-3Q), and MERRA-2, each for the time period 1980–2019 with 2.5° meridional resolution, which all were provided through the "Reanalysis Intercomparison Dataset" (RID) prepared by the SPARC Reanalysis Intercomparison Project (S-RIP; using updated data by Martineau et al. 2018). Note that here, for consistent zonal averaging of the 850-hPa zonal wind field, we masked out all data in these three reanalyses that correspond to data points below ground in MERRA-2 and therefore were missing in the MERRA-2 output, mainly located in the American and Asian high mountain regions and covering most parts of Greenland and the Antarctic continent.

In section 5, we evaluate "Stratospheric Water and Ozone Satellite Homogenized" ("SWOOSH") version 2.6 data produced by Davis et al. (2016). Starting in 1984, this dataset provides monthly averaged zonal-mean ozone distributions, merged from different observational instruments and interpolated on 31 pressure levels between 1 and 316 hPa with 2.5° meridional resolution. Furthermore, we consider zonally averaged TCO data from the ESA Climate Change Initiative (CCI) multisensor reanalysis (MSR), covering the years 1970–2022 with 0.5° meridional resolution (Copernicus Climate Change Service 2020; Van Roozendael et al. 2021a,b). We compare them with the "BS Filled Total Column Ozone Database" version 3.4.1 (monthly means, 1978–2019, 1° meridional resolution) by Bodeker et al. (2021, 2022).

We also consider zonal-mean, monthly averaged model output from 18 CCMI-1 climate simulations (Eyring et al. 2013; Hegglin et al. 2015) listed in Table 1. With two exceptions,

TABLE 1. CCMI-1 and CMIP6 simulations together with the number of ensemble members considered in this work.

CCMI-1	REF-C1	REF-C2
ACCESS CCM	1	2
CCSRNIES MIROC3.2	3	2
CESM1 CAM4-chem	3	3
CESM1(WACCM)	3	3
CHASER (MIROC-ESM)		1
CMAM	3	1
CNRM-CM5-3	1	1
EMAC (L47MA)	1	3
EMAC (L90MA)	1	1
GEOSCCM	1	1
GFDL-CM3	5	1
GRIMs-CCM	1	
MOCAGE	1	1
MRI-ESM1r1	1	1
NIWA-UKCA	3	5
SOCOL	3	1
UMSLIMCAT	1	1
UMUKCA-UCAM	1	2
CMIP6	SSP2-4.5	SSP5-8.5
CESM2(WACCM) ^a	3	3
CNRM-ESM2-1	3	3
GFDL-ESM4	1	1
MRI-ESM2.0	1	1

^aNo TCO data available.

UKESM1.0-LL

all of these models provided data for both a free-running hind-cast simulation ("REF-C1," 1960–2010) using historical observations, as well as for a projection run "REF-C2" (1960–2100) that is based on the WMO A1 scenario on ozone-depleting substances from 2011 combined with the CMIP5 representative concentration pathway (RCP) 6.0 (Eyring et al. 2013; Morgenstern et al. 2017; WMO 2011). Here, the RCP6.0 scenario assumes an increase of 6 W m⁻² in the global radiative forcing by the end of the twenty-first century compared to the preindustrial period (Taylor et al. 2012). We follow the naming convention by Morgenstern et al. (2017) for the CCMI-1 models and refer to this study for a comprehensive description of each model's individual setup.

3

3

In addition, we compare five models that are part of CMIP6 (Eyring et al. 2016) and that include interactive chemistry schemes [cf. Table 1, following the assessment by Keeble et al. (2021)]. Here, we limit our analysis to the CMIP6 shared so-cioeconomic pathway (SSP) 2-4.5 and SSP5-8.5 projections,

which simulate an increase of 4.5 and 8.5 W m⁻² in the radiative forcing by 2100, respectively, and additionally, each includes the global impacts of a possible SSP, that is, SSP2 (usually entitled as the "Middle of the road" scenario in the existing literature) and SSP5 ("Fossil-fueled development"), respectively (O'Neill et al. 2016; Riahi et al. 2017; Meinshausen et al. 2020). We use each model's first three ensemble runs, except for GFDL-ESM4 and MRI-ESM2.0 where at the time of this analysis the required model data were provided only for one ensemble member. For CESM2 (WACCM), no total-column ozone data were available.

We consider the CCMI-1 (CMIP6) data on 27 (19) pressure levels between 1 and 1000 hPa, which we interpolated on a meridional grid with 2.5° resolution. MOCAGE and UMSLIMCAT only provided output below 10 hPa and above 250 hPa, respectively. We furthermore limit the time range of our analysis to maximize the number of models for which the corresponding data are available, i.e., 1979–2008 for CCMI-1 REF-C1 and 2015–98 for CCMI-1 REF-C2 and the CMIP6 projections. We use ensemble-mean data for each individual model if more than one run is available (cf. Table 1).

b. Jet stream variability

In this work, we consider the year-by-year variability of the STJ in both hemispheres by assessing changes in the magnitude and the meridional location of zonal-mean maximum zonal wind speeds in the STJ regions. We follow the method by Davis and Birner (2013, 2017) and consider the maximum zonal wind vertical shear (relative to the 850-hPa zonal wind) as a function of latitude, where only data points up to 50 hPa above the thermal tropopause are included. The hemispheric maximum of this meridional profile of zonal wind shear maxima defines the strength of the STJ (STJ MAX), and the STJ's latitudinal position (STJ LAT) is obtained from the zero crossing of the associated meridional derivative profile (Davis and Birner 2013, 2017). To link our results to previous work and explore linkages between the STJ and the EDJ stream, we also diagnose the EDJ. In particular, we define the EDJ's magnitude (EDJ MAX) as the maximum of the zonalmean zonal wind at 850 hPa, with EDJ's meridional location (EDJ LAT). Table 2 provides an overview of the jet stream metrics considered in this study.

Previous studies also referred to the STJ as an indicator of tropical circulation changes, in particular of variations in the meridional extent of the overturning Hadley cell (e.g., Davis and Birner 2017; Staten et al. 2018; Waugh et al. 2018). Here,

TABLE 2. Overview of jet stream diagnostics used in this analysis.

Label	Description
STJ MAX	Maximum strength of the vertical shear of the zonal-mean zonal wind between 850 hPa and any given higher level; altitudes higher than 50 hPa above the thermal tropopause are excluded in the data (Davis and Birner 2013, 2017)
STJ LAT	Following Davis and Birner (2013, 2017), latitude of STJ MAX, derived from the zero crossing of the meridional derivative profile of maximum zonal wind vertical shear as a function of latitude
EDJ LAT	Latitude of maximum zonal-mean zonal wind at 850 hPa in the midlatitudes (e.g., Waugh et al. 2018; Adam et al. 2018a)
EDJ MAX	Zonal-mean zonal wind interpolated at EDJ LAT

in the interest of clarity, we will limit our analysis to the correspondence between (direct) wind field-related and (indirect) ozone-based metrics of STJ and EDJ variability. In some cases, we will point to extended results that are provided in the supplemental material.

In general, we quantify statistical jet stream covariability by computing Pearson correlation coefficients, where the linear trends of the anomaly time series, as obtained from least squares linear regressions, are removed beforehand. The correlation coefficients' confidence intervals are calculated using Fisher's z transformation. Similarly, we derive regression maps in the latitude—height plane pointwise by regressing the anomaly time series of the given data field (the predictand) at each grid point on a one-dimensional predictor index, after subtracting linear trends.

For calculating the jet stream diagnostics described above and tropical width metrics, we partially make use of "PyTropD" (Ming 2022), which is the Python edition of the "Tropical-Width Diagnostics" ("TropD") software developed by Adam et al. (2018a,b). We also use various helper functions that are available from PyTropD. Furthermore, if not stated otherwise, we refer to the WMO (1957) thermal tropopause in this paper, which we calculate from a modified version of PyTropD's internal routine <code>TropD_Calculate_TropopauseHeight</code>. The modification was necessary because the implemented criterion for the lapse rate tropopause definition in PyTropD turned out to be too strong.

3. Definition of ozone gradient diagnostics

The ozone metrics proposed in this work aim to detect STJ changes by measuring the variations of monthly mean, zonal-mean ozone near the STJ in each hemisphere. The climatological ozone distribution features well-pronounced gradients in the UTLS region (cf. Fig. 1) where the tropopause and the STJ act as tracer transport barriers. This motivates the different ozone gradient definitions discussed in this section, which are also listed in Table 3. We probe three different methods for diagnosing proxies of the STJ based on the meridional ozone gradients. Two of them require vertically resolved ozone data, while the third approach uses TCO profiles, which may be useful for application due to the availability of long-term TCO observational records (cf. section 5b). Two additional methods testing minor modifications of the setup are shown in the supplemental material.

The first diagnostic in Table 3 is based on the field of the meridional ozone gradient with respect to geographical latitude ϕ :

O3GRAD
$$(t, p, \phi) \equiv \frac{\partial_{\phi} \overline{\chi}}{\langle \overline{\chi} \rangle_{t}},$$
 (1)

which is derived from the ozone distribution in the latitude-pressure plane $\overline{\chi}(t,p,\phi)$, where the overbars in our notation denote zonal-mean quantities. The gradient field is weighted by the zonal-mean ozone climatology $\langle \overline{\chi} \rangle_t \equiv \langle \overline{\chi}(t,p,\phi) \rangle_t$, such that O3GRAD provides a relative measure of changes in

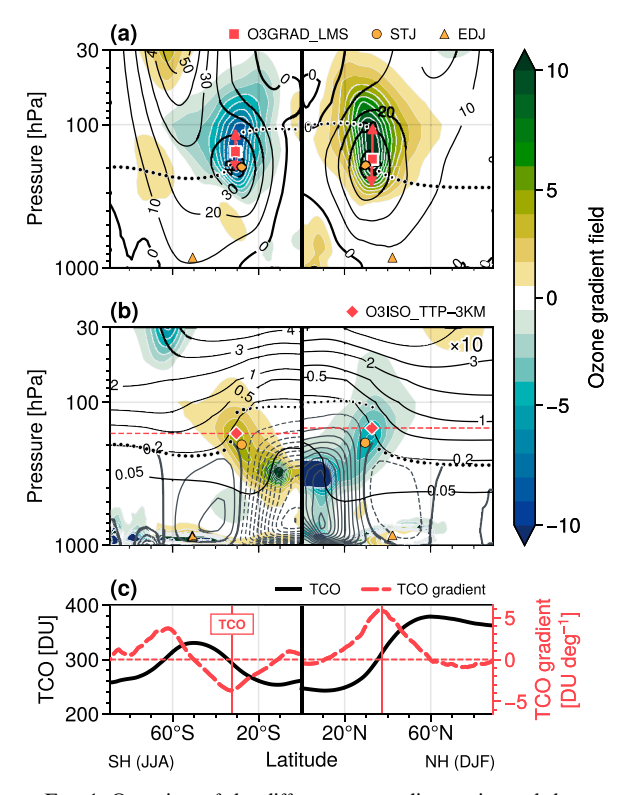


FIG. 1. Overview of the different ozone diagnostics and the underlying ozone gradient fields considered in this work. All panels show winter-mean climatologies derived from ERA5 reanalysis data 1979-2023 (NH DJF and SH JJA, respectively). The color codings provide (a) the meridional ozone gradient field (% deg⁻¹) and (b) the ozone isoline gradient field (km deg-1, scaled by a factor of 10), both computed from winter-mean climatological ozone. Contour lines show (a) the zonal-mean zonal wind (m s⁻¹) and (b) the zonal-mean ozone distribution (ppmv, black contours) as well as the mean meridional mass streamfunction [gray contour lines with intervals of 2×10^{10} kg s⁻¹, displayed below the tropopause only; computed using PyTropD by Adam et al. (2018a)]. The thick dotted lines in (a) and (b) show the mean thermal tropopause. The orange and red markers in (a) and (b) show the meridional locations of the jet stream cores and ozone gradient maxima, respectively. In (a), red vertical arrows illustrate the altitude range for vertical averaging of the ozone gradient profiles, as defined for the O3GRAD_LMS metric in Table 3. The reference level Z_{ref} for the O3ISO_TTP-3KM diagnostic in (b) is marked by the red dashed lines. (c) Winter-mean TCO in Dobson units (DUs; solid lines) and the corresponding meridional gradient profile (DU deg⁻¹, dashed lines), with the locations of the subtropical gradient maxima indicated by vertical red lines.

zonal-mean ozone and therefore is insensitive to the background ozone mixing ratios that usually vary strongly with altitude.

The isolines of zonal-mean ozone in the UTLS closely follow the tropopause, in particular the tropopause break in the STJ region is closely aligned with a strong slope in ozone isolines (see Fig. 1b). This motivates to use a second metric that is derived from the meridional gradients of the height of

TABLE 3. Classification of ozone gradient metrics. See the main text for a detailed description.	TABLE 3.	Classification	of ozone	gradient metrics	 See the main 	text for a	detailed description.
--	----------	----------------	----------	------------------	----------------------------------	------------	-----------------------

Label	Gradient (unit)	Required data	Profile	Definition ^a
O3GRAD_LMS	Meridional (% °N ⁻¹)	Vertically resolved ozone field	Vertical averaging with $N = 10$ levels	$\sum_{i=0}^{N-1} \text{O3GRAD}[t, Z = Z_{\text{TTP}}(t) + i\delta Z, \phi]/N$ with $\delta Z = [Z_{\text{PTP}}(t) - Z_{\text{TTP}}(t)]/(N-1)$
O3ISO_TTP-3KM	I Isoline (km °N ⁻¹)	Vertically resolved ozone field	3 km below tropical tropopause height	$O3ISO[t, p = p_{ref}(t), \phi]$
TCO	Meridional (DU °N ⁻¹) ^b	TCO	_	$\partial_{\phi} TCO(t, \phi)$

^aDefinitions of O3GRAD and O3ISO as in Eqs. (1) and (2) in the main text, respectively.

zonal-mean ozone isolines (referred to as "ozone isoline gradient field" in the following):

O3ISO
$$(t, p, \phi) \equiv \frac{dZ(p)}{d\phi} \Big|_{\overline{\chi} = \text{const.}} = -\frac{\partial_{\phi} \overline{\chi}}{\partial_{Z} \overline{\chi}} (t, Z, \phi)$$
$$= \frac{H^{\partial_{\phi} \overline{\chi}}}{p \frac{\partial_{\phi} \overline{\chi}}{\partial_{p} \overline{\chi}}} (t, p, \phi), \tag{2}$$

where $Z(p) \equiv H \log(p_0/p)$ denotes log-pressure height with scale height H = 7 km and surface pressure $p_0 = 1000$ hPa.

Figure 1 provides the winter-mean climatologies of these ozone gradient fields computed from monthly mean ERA5 reanalysis data for 1979–2023 [Northern Hemisphere (NH) DJF and Southern Hemisphere (SH) JJA]. The meridional ozone gradient field in Fig. 1a clearly shows one subtropical extremum in each hemisphere. These extrema are vertically stretched, roughly following the tropopause break, and peak around the STJ core. The ozone isoline gradient field peaks in the tropics around 300 hPa, expanding across the tropopause break into the lowermost stratosphere (Fig. 1b). Here, the high tropospheric gradients correspond to steep isoline curvatures, which are formed by both up- and downward ozone transport through the overturning Hadley circulation in the tropics (illustrated by the $\overline{\chi}=50$ ppbv ozone isoline and the mean meridional mass streamfunction in Fig. 1b).

Except for the TCO gradient metric, it is necessary to apply vertical averaging or level selection to gain latitudinal profiles from the two-dimensional gradient fields, which the metric can be based upon. We tested different procedures to perform the vertical selection (see also supplemental material) and settled on the following:

- 1) Due to the vertically coherent structure of the subtropical O3GRAD extrema (Fig. 1a), we average vertically across N=10 equidistant log-pressure height levels, equally distributed between the mean tropical tropopause (TTP; $\phi < 20^{\circ}$) and the mean polar tropopause (PTP; $\phi > 60^{\circ}$). To capture vertical shifts and fluctuations of the lowermost stratosphere (LMS) over time, we allow both TTP and PTP to be a function of time (at monthly resolution as with other diagnostics). We refer to the resulting ozone gradient metric as "O3GRAD_LMS" (cf. Table 3).
- We select fixed reference levels Z_{ref} = H log(p₀/p_{ref}) onto which the ozone isoline gradient field (O3ISO) is interpolated (cf. Fig. 1b). Again, to account for vertical shifts and

fluctuations, this level is adapted monthly. Here, we link this reference level to the mean tropical tropopause height, i.e.,

$$Z_{\text{ref}}(t) \equiv Z_{\text{TTP}}(t) + \Delta Z,$$
 (3)

where ΔZ denotes a constant offset. We set $\Delta Z = -3$ km in the following, representing an isobar that is located below the TTP and that approaches the altitude of the STJ core to maximize STJ covariability. Note, however, that biases in observational ozone data due to measurement limitations occur especially at lower altitudes (cf. section 5), which effectively narrows the range of suitable offset values ΔZ . The corresponding metric is called "O3ISO_TTP-3KM" in Table 3 and aims to track changes associated with STJ dynamics across the set of isolines featuring strong curvatures along the tropopause break.

Figure 1 shows that all these ozone gradient definitions, O3GRAD_LMS, O3ISO_TTP-3KM, and TCO, feature well-pronounced subtropical extrema for both hemispheres on a climatological average. As a final step, we derive two types of key parameters for each profile. Given multiple time steps, they form two index time series:

- The absolute magnitude of the subtropical extremum, searched
 for among all data points across latitude and for each month
 and each hemisphere separately, referred to by adding a suffix
 "MAX" behind each definition's label. Accordingly, accounting for the sign convention in our gradient definitions, from
 now on we will always refer to absolute subtropical gradient
 maxima for both hemispheres.
- The latitude of that maximum, applying the smoothing approach with strength parameter n=6 introduced by Adam et al. (2018a), where we use PyTropD's TropD_Calculate_MaxLat routine, labeled by adding a suffix "LAT."

The climatological location (LAT) of each ozone gradient maximum is illustrated in Fig. 1. During our analysis, we found substantial differences in the gradient maxima's average strength throughout the year due to the seasonal cycle. In the appendix, we provide a qualitative estimate on their variable peak sharpness, which turned out to be significantly reduced especially during summer, causing issues in identifying these maxima. We therefore limit our analysis to hemispheric winters in the following and add the results for annual-mean data where appropriate to allow for a comparison with the results from the existing literature.

^bDU = Dobson unit.

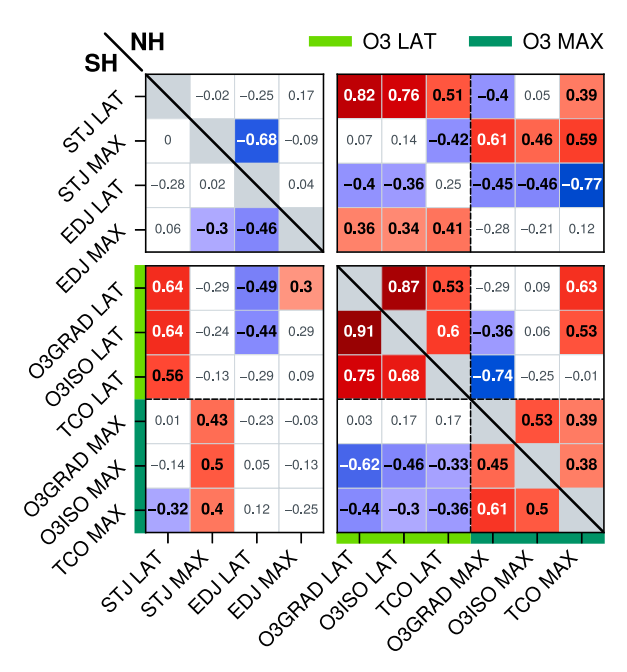


FIG. 2. Pearson's correlation coefficients, based on interannual variability, for all combinations of detrended jet stream and gradient-based ozone diagnostics listed in Tables 2 and 3, respectively. The results were computed separately for the NH (upper-right area) and SH (lower-left area), based on winter-mean ERA5 data (1979–2023, NH DJF, and SH JJA). For better readability, the ozone gradient diagnostics are divided into two groups of "O3 LAT" and "O3 MAX" time series, which are marked by the light and dark green panel shading, respectively. In addition, the O3GRAD_LMS metric from Table 3 here is abbreviated as "O3GRAD" and similar for O3ISO_TTP-3KM which is denoted as "O3ISO." Statistical significance at the 95% level was found where color coding and bold type are applied to the corresponding entries in this table. Plot design inspired by Waugh et al. (2018, their Fig. 5).

4. Ozone gradient metrics in ERA5 reanalyses

In this section, we evaluate the statistical relation of interannual variability between the jet stream diagnostics from Table 2 and the ozone gradient metrics defined in Table 3 and try to shed light on the physical mechanism behind their correspondence.

Figure 2 provides the associated correlation coefficients based on winter-mean ERA5 reanalysis data for 1979–2023, combining the results for the NH and SH (based on DJF and JJA winter seasons, respectively). Here, the individual entries in the correlation table are color coded if the statistical significance of the associated correlation was found at the 95% level. We note that, overall, the different ozone gradient definitions mostly agree well in measuring interannual variations in the location and strength of the subtropical gradient maxima, as indicated by the strong correlations within the two sets of LAT and MAX ozone indices, respectively (lower-right panel of Fig. 2). In particular, we find the most robust correlations among the LAT-type metrics ("O3 LAT") in

both hemispheres. In the NH, TCO MAX is significantly coupled with the LAT time series of the two other ozone gradient metrics, and TCO LAT is strongly anticorrelated with the O3_GRAD_LMS maxima. TCO LAT and TCO MAX themselves, however, turn out to be decoupled and similar for the LAT and MAX of the O3GRAD_LMS and O3ISO_TTP-3KM diagnostics, indicating that they represent distinct variability modes. In the SH, this only holds for the O3GRAD_LMS definition, and we find significant anticorrelations among the LAT and MAX metrics based on TCO and isoline gradients.

Across all ozone-based metrics, we find robust correlations with the STJ properties; i.e., the latitudinal positions of the ozone gradients (O3 LAT class of indices) vary with the STJ latitude and are similar for the gradients' magnitudes (O3 MAX) and the strength of the STJ in both hemispheres (lower-left and upper-right panels in Fig. 2). This relation is strongest between STJ LAT and the LAT-type gradient metrics in the NH. Here, we also find substantial anticorrelations between the MAX-type metrics and the EDJ LAT, which is likely due to the dynamical coupling between EDJ LAT and the strength of the STJ (r = -0.68 for NH in the upper-left panel of Fig. 2). Similarly, EDJ MAX is robustly coupled with the O3 LAT time series in the NH, although STJ LAT and EDJ MAX are not directly linked in ERA5 (r = 0.17).

Overall, we find high consistency between ozone-based metrics of the strength and latitude of the subtropical maximum and a high correlation to the respective STJ properties. An extended version of Fig. 2 is provided as Fig. S1 in the online supplemental material, showing also correlations between two slightly modified versions of the above introduced ozone gradient diagnostics, as well as common metrics of tropical width associated with the tropospheric meridional mass streamfunction, the subtropical tropopause break, and near-surface zonal winds.

For understanding the covariability with the STJ, consider Fig. 3 which shows the responses of the underlying ozone gradients to variations of STJ strength and position. These are computed by regressing the winter-mean ozone gradient anomalies on the standardized index time series STJ MAX and STJ LAT, respectively (ERA5, 1979–2023, NH DJF, and SH JJA). In addition, we consider the meridional gradient field of modified potential vorticity (Lait 1994):

$$\partial_{\phi} \overline{\Pi} \equiv \partial_{\phi} [\overline{P}(\overline{\theta}/\theta_0)^{-9/2}], \tag{4}$$

where \overline{P} denotes the zonal-mean potential vorticity (PV) and $\overline{\theta}$ is the zonal-mean potential temperature with reference level $\theta_0 \equiv 300$ K. We find that the subtropical gradient maxima in the O3GRAD, O3ISO, and PV fields simultaneously follow the changes in the latitudinal position of the STJ, as indicated by the dipole-like response signatures in Figs. 3a–c. Likewise, in all cases, we clearly observe sharper gradients when the STJ strengthens (Figs. 3e–g). This is consistent with the meridional PV gradient acting as a tracer transport barrier in the STJ region, regulating the amount and the equatorward extent of quasi-isentropic ozone transport by eddy mixing across the subtropical tropopause. Figure 3 also shows that

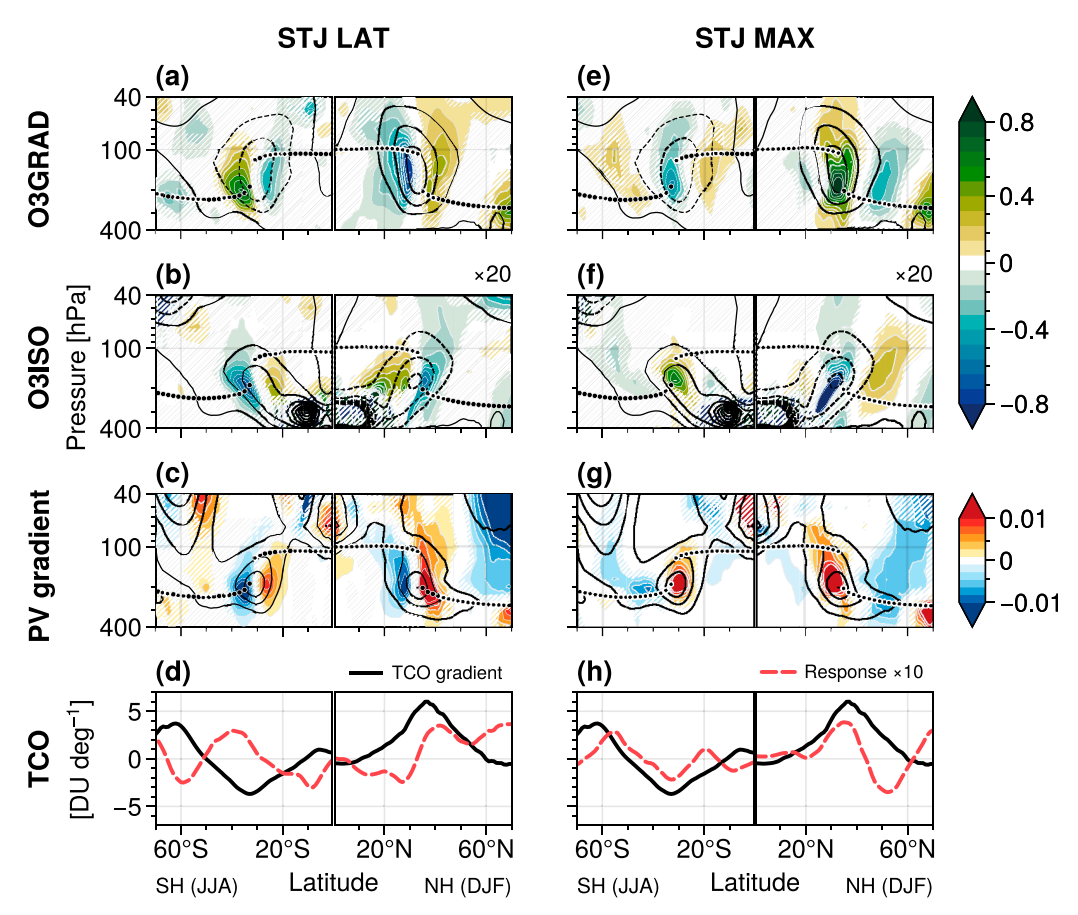


FIG. 3. Meridional ozone gradient field (O3GRAD), ozone isoline gradient field (O3ISO, scaled by an additional factor of 20 for plotting), and meridional gradient field of modified PV (Lait 1994) regressed on the standardized (a)–(c) STJ LAT and (e)–(g) STJ MAX index time series, respectively. The regression maps are shown in units of percent per degree (% deg⁻¹), kilometers per degree (km deg⁻¹), and PV units per degree (PVU deg⁻¹), respectively, per standard deviation of the STJ predictors. Black contours show the structures of the gradient field climatologies (dashed lines indicate negative values). The thick dotted lines represent the mean thermal tropopause. (d),(h) As before, but for the response (red dashed lines) of the TCO meridional gradient profiles (DU deg⁻¹; black lines show climatology), obtained by linear regression on the standardized STJ diagnostics. All results were calculated from wintermean ERA5 reanalysis data (1979–2023). Hatches indicate where the regression maps are not statistically significant at the 95% level.

the response signals in the SH are less pronounced and more confined to narrow altitude ranges compared to the NH, which may be associated with the weaker correlation coefficients during austral winter found in Fig. 2 (lower-left panel). We hypothesize that the limited contribution of planetary-scale atmospheric waves in the SH may play a role here, but analyzing the local ozone budget as a function of zonal wavenumber is left for future work. Note that the regression maps in Fig. 3 show the response relative to the ozone gradient climatology (illustrated by the black contour lines), which partially feature subtropical gradient *minima* (i.e., negative meridional gradients). However, the associated correlation coefficients are always positive in Fig. 2 as we consider *absolute* gradient magnitudes.

In addition, Figs. 3d and 3h provide further evidence that STJ covariability is also reflected by the meridional TCO

gradients similar to the vertically resolved ozone gradients but with some deviations from the simple response signatures characterizing the shifting and strengthening of the gradient maxima upon changes in STJ LAT and STJ MAX, respectively. These differences are consistent with the significant amount of cross correlations with the TCO metrics identified in Fig. 2. Note that especially in the NH, we also expect some impact on tropospheric ozone due to meridional fluctuations of the midlatitude jet (EDJ LAT) where we found a strong anticorrelation with the TCO MAX diagnostic r = -0.77 according to Fig. 2.

The results from this section show that the gradient-based ozone metrics primarily measure variations of the STJ, which appeared to be consistent with our knowledge on the jet working as a dynamically fluctuating ozone transport barrier in the subtropics. We found a clear dichotomous behavior

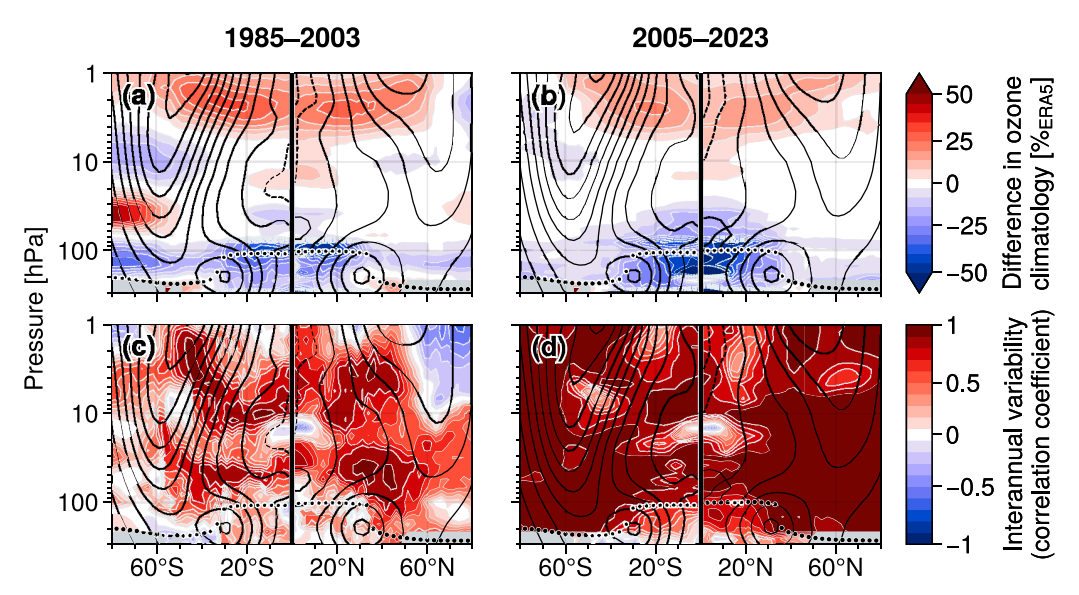


FIG. 4. (a),(b) Differences in climatological zonal-mean ozone during winter (NH DJF and SH JJA) between ERA5 and SWOOSH relative to ERA5 ozone. (c),(d) Correlation coefficients for interannual zonal-mean ozone variability derived from SWOOSH compared to ERA5. Contour lines show the corresponding zonal-mean zonal wind climatologies. The thick dotted lines illustrate the winter-mean tropopause. The left and right columns of this figure provide the results for the time periods until 2003 and starting 2005, respectively.

among these ozone metrics, i.e., statistically significant correspondence of the index time series with either the varying zonal-mean zonal wind strength in the STJ region (subset of MAX-type indices) or with the jet's meridional position (LAT). In the NH, the metrics measuring fluctuations in the strength (or meridional position) of the STJ are also coupled to the shifting (or strengthening) of the EDJ (cf. Lorenz and Hartmann 2001, 2003).

5. Comparison with observational data

After constructing tracer-based diagnostics for STJ variability, we now make use of observational records in two ways: First, we evaluate the ozone index time series obtained from ERA5 reanalysis data by comparing them with ozone measurements. Second, we derive trends across the historical time period and evaluate the trend uncertainties of this observation-based approach.

a. Comparison with SWOOSH ozone data

We use the SWOOSH dataset described in section 2 to evaluate the ozone gradient definitions from Table 3 that are based on the vertically resolved distribution of zonal-mean ozone. As indicated by Figs. 4a and 4b, especially in the middle stratosphere, winter-mean ERA5 ozone agrees well with SWOOSH ozone across two predefined time intervals of equal length ranging 1985–2003 and 2005–23, respectively. The biases in the climatological ozone distribution mainly occur in the tropical UTLS region and in the upper stratosphere. We find substantial differences in ERA5 and SWOOSH interannual ozone covariability between these two time intervals,

as measured by pointwise Pearson correlation coefficients in the latitude-pressure plane: Figs. 4c and 4d show a less homogeneous and rather modest correlation between ERA5 and SWOOSH year-by-year ozone anomalies prior to 2005 and strongly increased correlation values across almost the entire meridional plane after that date. This is presumably due to the availability of global, densely sampled Aura MLS measurements (Waters et al. 2006), which entered both the SWOOSH data processing and ERA5 data assimilation in more recent years. Overall, although differences between ERA5 and SWOOSH ozone are still substantial for 2005-23 around the STJ in both hemispheres, winter-mean ozone anomalies, which play a key role in defining ozone-based metrics of atmospheric variability, seem to agree much better in more recent years (as seen by the high correlation values in Fig. 4d).

Intercomparisons between the ERA5 and SWOOSH ozone gradient metrics turned out to be challenging due to the substantial differences in interannual ozone variability between the earlier and later parts of the available time period. In particular, artifacts in the SWOOSH ozone gradient profiles prior to 2005 resulting from missing and noisy data in the UTLS caused problems when applying our computation routines (not shown). During this time period, SWOOSH is dominated by data from solar occultation sensors that provide around two orders of magnitude less data than Aura MLS and are subject to cloud and aerosol interference (e.g., due to Mount Pinatubo) that results in very sparse sampling in the UTLS. As a consequence, we found poor correlations between the ERA5 and SWOOSH ozone metrics for the time period up to 2005 and mostly very good agreement for the recent years

(not shown). The O3ISO_TTP-3KM definition represents the only exception with no statistically significant correlations during 2005–23. This is probably due to the underlying isoline height gradient fields, which are based on both meridional and vertical ozone gradients [cf. Eq. (2)] and therefore may be much more sensitive to biases in the ERA5 and SWOOSH ozone data. We obtained much better agreement between the ERA5 and SWOOSH O3ISO metrics when we shifted the reference level $Z_{\rm ref}$ for evaluating the gradient profiles upward (not shown), i.e., if ΔZ was increased in Eq. (3). This is because the relative differences between the reanalysis data and the ozone measurements decrease at higher altitudes. However, we found that modification of ΔZ can also lead to reduced covariability of the ozone gradient metrics with the STJ, indicating an important trade-off in the parameter setup.

b. Historical trends from TCO observations

Our analysis showed that observational, vertically resolved ozone data are not yet available in sufficient quality and for a long enough time period to allow an assessment of trends based on the two-dimensional, zonal-mean ozone gradient fields O3GRAD and O3ISO. We therefore apply the two total-column ozone gradient metrics, TCO LAT and TCO MAX, where we compare TCO from ERA5 and the ESA CCI MSR. Since the underlying model for the ESA MSR uses ECMWF meteorological data (Van Roozendael et al. 2021a), we examine zonal-mean "BS Filled" TCO data by Bodeker et al. (2021) as an additional, and perhaps more independent, reference. Using these datasets, we compare historical trends in the TCO-based metrics with the trends found in the strength and location of the jet streams, which we derive directly from global zonal-mean zonal wind data from the ERA5, CFSR/CFSv2, JRA-3Q, and MERRA-2 reanalyses (S-RIP RID; Martineau et al. 2018). It is not clear a priori whether and how variations in TCO, indicating variability of vertically accumulated ozone, allow for a precise quantification of local covariability between the jet stream and ozone in the STJ regions. The TCO gradient metrics may still represent indirect but meaningful indicators of jet stream variability if they are sufficiently well related to the jet stream properties under consideration, i.e., significant correlations between these TCO-based diagnostics and the STJ are essential for the subsequent interpretation of the results.

Figure 5 provides the results for the years 1980–2019, where we computed linear trends from annually resolved data based on both winter-mean and annual-mean anomalies and for both hemispheres separately. Here, we estimated the trend uncertainties from a bootstrapping approach, each based on 1000 randomly sampled time series containing 30 out of the 40 index time steps. All reanalyses indicate a poleward movement of the STJ in both hemispheres and for both winter mean and annual mean (Figs. 5a,d,g,j), albeit not all of these trends are statistically significant. However, the high correlations and mostly similar trend magnitudes across these four reanalyses suggest that these trends may be robust. We find that, if the correlation with STJ LAT is significantly strong (i.e., as given in Figs. 5a,d,g but not Fig. 5j, as indicated by the

colored boxes at the bottom of each panel), then indeed the TCO LAT metric qualitatively reproduces this poleward shifting of the STJ for all three TCO datasets (ERA5, MSR, and BS; red bars in Fig. 5). We find larger trends in the TCO metrics than for the STJ, which is consistent with stronger interannual variability in TCO LAT compared to STJ LAT (not shown). This may be due to chemical and nonlinear effects and due to advective ozone transport beyond the STJ core, which is not governed by the strength of the subtropical mixing barriers. In general, based on the TCO LAT trend $\Delta\phi_{\rm TCO}$, the trend in jet latitude may be indirectly estimated from TCO covariability as

$$\Delta \phi_{\text{STJ}} \simeq b[\text{TCO, STJ}] \cdot \Delta \phi_{\text{TCO}},$$
 (5)

where *b*[TCO, STJ] is the linear regression coefficient of the multireanalysis STJ anomaly time series regressed on the TCO index. This indirect estimate assumes that the system dynamics giving rise to the trend behave the same as those giving rise to intrinsic, interannual variability. This is somewhat akin to the fluctuation–dissipation theorem (e.g., Leith 1975). We find that the magnitudes of poleward STJ movement inferred from the TCO scale well with the direct reanalysis STJ LAT trends for winter-mean NH variability (orange bars in Fig. 5a) but are substantially reduced for the SH compared to the wind field–related STJ metric in Fig. 5g. In contrast, enhanced trend values are found for NH annual-mean data, where now the TCO trends show statistical significance, whereas STJ LAT trends from the reanalysis data do not (Fig. 5d).

For the NH during winter, Figs. 5b and 5c furthermore show that the trends in the STJ's strength (STJ MAX) and the location of the midlatitude jet (EDJ LAT) are not statistically significant, and neither are the trends in TCO MAX. For annual-mean data, TCO MAX trends suggest a robust weakening of the STJ and a poleward shift of the EDJ during the historical time period, which qualitatively agrees with the (nonsignificant) STJ MAX and EDJ LAT reanalysis trends (Figs. 5e,f). In particular, Fig. 5e provides an example where the statistically significant trend estimates from the observation-based TCO MAX metric may help to constrain the diverging results on STJ MAX trends from the different reanalyses.

Finally, Figs. 5g-l suggest that constraining jet variability from our TCO gradient metrics is rather challenging in the SH. In particular, the TCO LAT trend magnitudes in Fig. 5g roughly compare with the NH results (Fig. 5a), but we find much larger confidence intervals, presumably due to the limited availability of observational data during Austral winter and weaker TCO gradients in the subtropics compared to the NH. Further conclusions, e.g., on covariability with STJ MAX and EDJ LAT in the SH, turn out to be difficult due to the insufficient statistical correlations with the TCO diagnostics (cf. white boxes indicating weak correlations in Figs. 5h,i). Finally, the statistically significant annual-mean TCO MAX trends suggest poleward movement of the EDJ (orange bars in Fig. 5l) and weakening of the STJ (orange bars in Fig. 5k), but the latter contradicts the robust STJ MAX trends from the

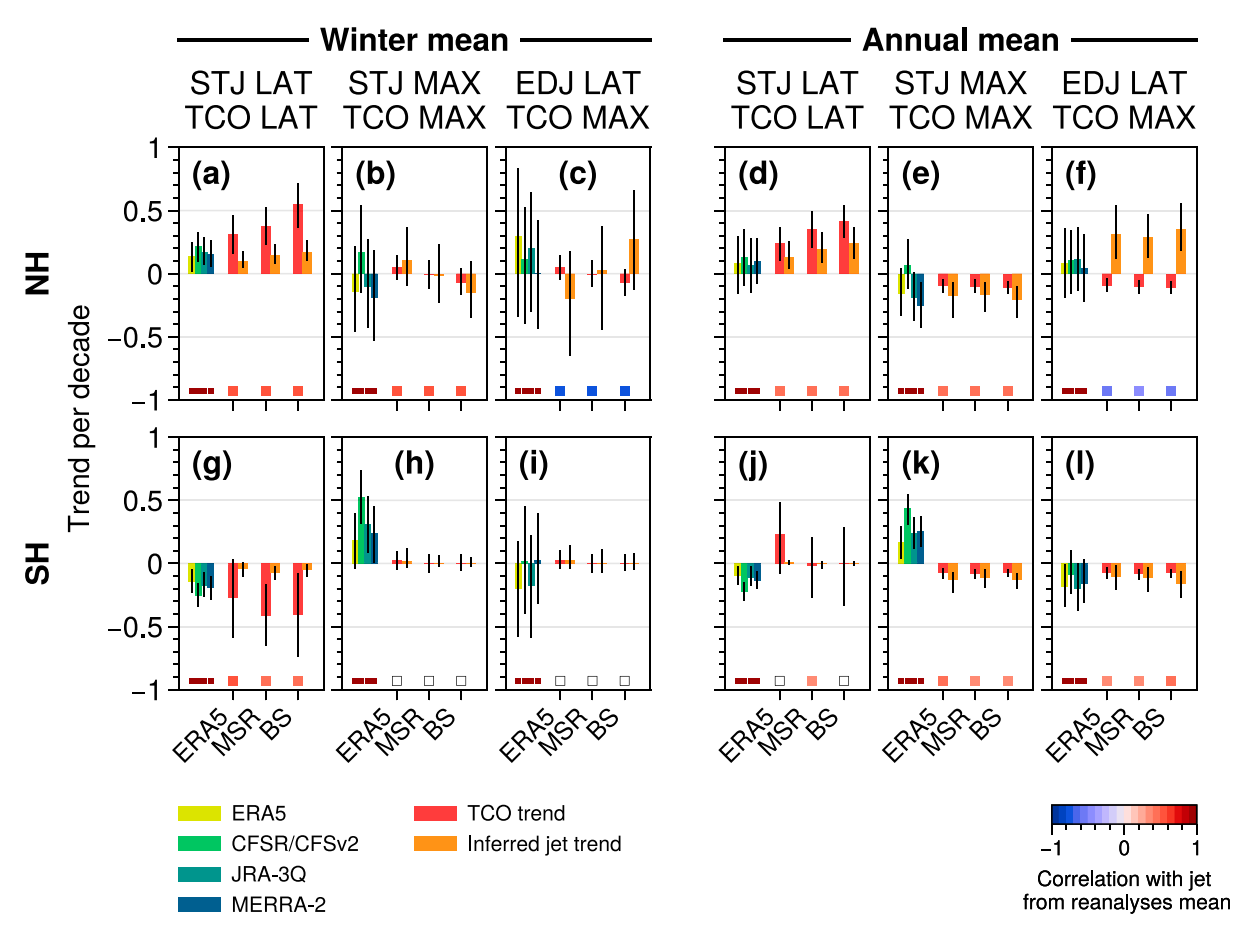


FIG. 5. Historical (1980–2019) STJ and EDJ trends from reanalyses (green bars on the left side of each panel) and TCO trends (red bars) from ERA5, MSR, and BS TCO data. TCO trends are compared to the TCO LAT time series for STJ LAT, and TCO MAX otherwise, following the correlation table in Fig. 2. The unit of all LAT trends is degrees per decade (deg decade⁻¹), where positive values indicate a northward shift. STJ MAX and TCO MAX trends are provided in units of m s⁻¹ decade⁻¹ and DU deg⁻¹ decade⁻¹, respectively. Correlation coefficients with the multireanalysis mean jet variability are provided by the color-coded boxes at the lower end of each panel, where white boxes indicate that no significant correlation was found at the 95% level. The orange bars provide estimates on the jet trend magnitudes obtained from TCO variability according to Eq. (5). Error bars provide 95% confidence intervals derived from a bootstrapping approach each based on 1000 randomly sampled 30-yr time series.

reanalyses. Note that in Figs. 5k and 5l, correlations between TCO MAX and the two jet stream metrics are statistically significant but rather weak, which complicates interpretations. In addition, substantial ozone depletion in the SH higher latitudes may impact the subtropical TCO gradients, which may weaken the relation between jet stream variability and ozone gradient changes.

6. Ozone gradient metrics from climate simulations

In this section, we first assess how the relation between jet stream variability and ozone gradients is represented in CCMI-1 climate models as compared to ERA5 reanalysis data. Figure 6 shows the multimodel averaged correlation coefficients similar to the ERA5 correlations shown in Fig. 2, where we used winter-mean 1979–2008 model output from 17 CCMI-1 REF-C1 hindcast simulations listed in Table 1. The

corresponding correlation table for each individual model is available in the supplemental material. Statistical robustness is assumed where at least 80% of the models agree on the sign of covariability and provide a statistically significant correlation at the 95% level (indicated by colors). Additionally, agreement in terms of the spread of the correlations between models, as measured by cross-model standard deviations, is indicated by bold numbers as an indication of robustness, in the case of significant correlations with a threshold of 25% of the multimodel mean (MMM) and 50% for the nonsignificant correlation values.

Figure 6 (lower-right panel) shows that the CCMI models provide some robust correlations within the two groups of O3 MAX and O3 LAT ozone metrics, respectively, which is mostly consistent with ERA5 except for the correlations related to TCO LAT where the models simulate weaker correlations. Furthermore, the models do not reproduce the ERA5

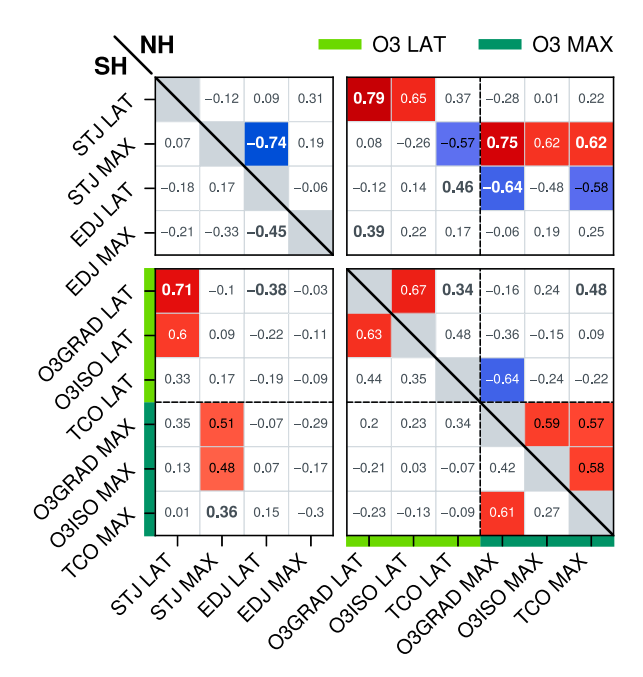


FIG. 6. Table of correlation coefficients for winter-mean jet stream and ozone gradient metrics obtained from 17 CCMI-1 REF-C1 hindcast simulations listed in Table 1 (1979–2008). The color coding provides an estimate on the statistical robustness of each correlation; i.e., at least 80% of the models agree on the sign of the correlation coefficient and show statistical significance at the 95% level. Bold type numbers indicate that the cross-model standard deviation of the correlations is below 25% (50%) of the MMM for the (non)significant correlation values. Other details are as in Fig. 2.

anticorrelations between O3 MAX and O3 LAT metrics in the SH, and the substantial model spreads there (>50% according to the formatting criterion described above) suggest that the strength of this coupling is influenced by the different modeling schemes. In contrast, the robust anticorrelation between O3GRAD_LMS MAX and TCO LAT in the NH agrees quite well with ERA5. Overall, the CCMI models clearly reflect the two-mode behavior of the ozone gradient diagnostics, where we found that O3 LAT metrics strongly correlate with the STJ's meridional position (STJ LAT) in both hemispheres and are similar for O3 MAX and STJ MAX (lower-left and upper-right panels in Fig. 6). Substantially reduced correlations are only found for TCO LAT. In some cases, the high correlation magnitudes and reduced model spreads provide evidence that STJ-ozone covariability in part is even more pronounced than in ERA5 (cf. individual models in the supplemental material). We hypothesize that the inconsistencies in the reanalysis output due to data assimilation may play a role here. The simulations also reproduce the significant anticorrelation between the strength of the STJ (STJ MAX) and the EDJ LAT in the NH (r = -0.74, upperleft panel in Fig. 6) and, as a consequence, robust anticorrelations between O3 MAX metrics and EDJ LAT.

As a second step, we analyze the projected trends for the twenty-first century in the zonal-mean ozone gradient structure in the subtropics, in particular associated with variations in the strength and location of the STJ in both hemispheres. To do so, we use monthly averaged model output from the CCMI-1 REF-C2 climate projections (17 models; cf. Table 1). We compare them with simulations from the CMIP6 using two different SSP climate forcing scenarios, where we select five CMIP6 models that use an interactive chemistry scheme [following Keeble et al. (2021)]. Figure 7 provides the linear trends found in the STJ metrics and in the ozone gradient time series defined in Table 3, as obtained from winter-mean projections for the years 2015–98.

Figures 7b and 7d show that the O3GRAD_LMS MAX and TCO MAX time series feature positive multimodel mean trends (illustrated by the vertical bars) for all three scenarios (REF-C2, SSP2-4.5, and SSP5-8.5), indicating a strengthening of the meridional ozone gradients in the STJ region in both hemispheres. This is consistent with the projected increase in STJ zonal wind speeds, which act to strengthen the effective dynamical transport barrier for wave-induced ozone mixing. For O3ISO_TTP-3KM, we find similar results except for CCMI-1 REF-C2 where some model outliers cause rather extreme multimodel mean trends.

Direct comparison of the CCMI-1 and CMIP6 groups of simulations needs to be treated with caution due to the substantial differences in the scenario setup and the small subset of CMIP6 models analyzed here. However, comparing the underlying RCP (Taylor et al. 2012; cf. section 2a), Figs. 7b and 7d suggest that the multimodel mean STJ MAX trends from the CCMI-1 REF-C2 runs (RCP6.0) indeed range between the two CMIP6 SSP2-4.5 and SSP5-8.5 projections, which assumed a slightly lower (RCP4.5) and larger (RCP8.5) future increase in global radiative forcing, respectively. Both CMIP6 scenarios project a robust strengthening of the STJ in both hemispheres, with at least doubled trend magnitudes for the extreme SSP5-8.5 setup compared to SSP2-4.5.

Figure 7c shows that, for the multimodel average, the simulations project a robust poleward movement of the subtropical ozone gradient maxima along with the STJ in the SH, again in agreement with our understanding of the underlying ozone transport mechanisms discussed in section 4. The CMIP6 SSP5-8.5 runs show that this shifting becomes stronger upon increased release of greenhouse gases into the atmosphere. In contrast, for the NH, the trends in STJ LAT are less clear among CCMI-1 and CMIP6 (Fig. 7a), and neither are the projected changes in O3GRAD LMS LAT and TCO LAT, which suggest a robust strengthening and no significant changes in the subtropical ozone gradients, respectively. The latter may be consistent with the significant anticorrelation of TCO LAT with STJ MAX on interannual time scales in ERA5 (cf. Fig. 2), which is indeed reproduced by most of the CCMI-1 models (cf. Fig. 6 and supplemental material), such that TCO LAT would track the counteracting effects of both STJ strengthening and latitudinal jet shifting in the NH.

From the trend analysis of the O3ISO_TTP-3KM metric in Fig. 7, we obtain more divergent results, with some CCMI-1 models showing extreme, rather unrealistic changes in the subtropical ozone gradient magnitudes compared to others and CMIP6. In contrast, trends in O3ISO_TTP-3KM LAT

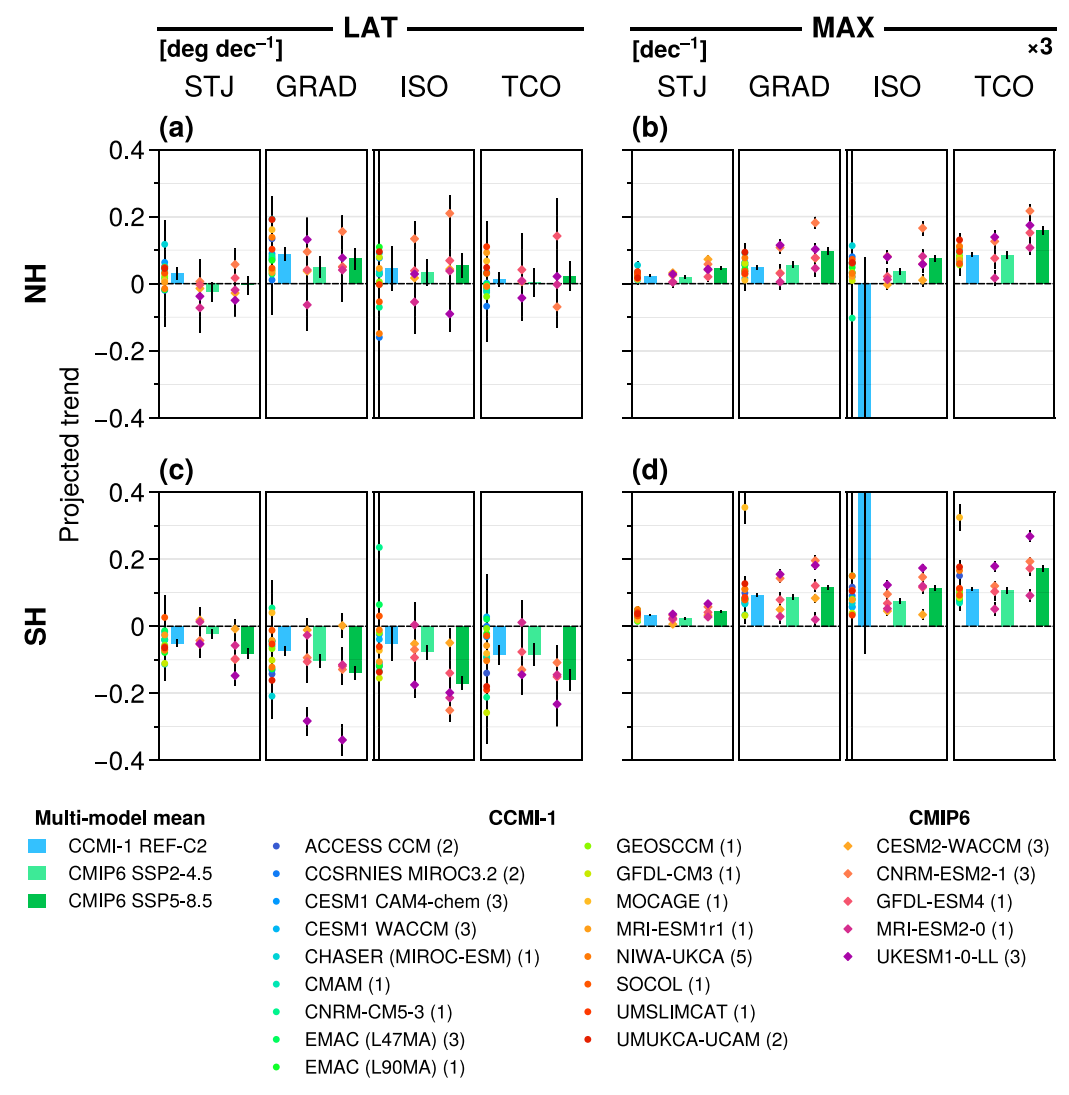


FIG. 7. Projected STJ and ozone gradient trends based on winter-mean data from CCMI-1 (REF-C2) and CMIP6 (SSP2-4.5 and SSP5-8.5) simulations for 2015–98 (NH DJF and SH JJA). Here, the O3GRAD_LMS metric from Table 3 is denoted as "GRAD" and O3ISO_TTP–3KM is abbreviated as "ISO." The models are listed in the legend together with the number of model runs used for computing ensemble-mean linear trends (shown in parentheses each). MMM trends are provided by the vertical bars right next to the individual model markers. Note that the large CCMI-1 MMM trends for ISO MAX are due to outliers that are not fully displayed within (b) and (d). Error bars show 95% confidence intervals for the linear trend regressions. All LAT trends are given in units of "N decade⁻¹, and MAX trends were normalized relative to climatology (1 decade⁻¹, scaled by a factor of 3 for plotting).

turn out to agree better with those derived for O3GRAD_LMS LAT (Figs. 7a,c) and are mostly consistent with the projected changes in the STJ. We assume that the poor performance of the isoline-based metric may sometimes be caused by the limited vertical resolution of the model output (cf. similar issues in analysis with SWOOSH observational data reported in section 5a), indicating potential practical limitations when applying this vertically resolved ozone gradient diagnostic.

Overall, we conclude that CCMI-1 and CMIP6 projections mostly provide evidence for robust coupling of the subtropical

jet stream and meridional ozone gradient mean states in extended climate simulations under different external forcing scenarios. While this analysis was based on a multimodel mean framework, Fig. 8 provides an example on STJ-ozone covariability across the individual models considered in this section. In particular, we find robust correlations between the relative strengthening of the STJ and the relative increase in ozone gradient magnitudes in the STJ region in both hemispheres (based on the O3GRAD_LMS ozone gradient metric) across CCMI-1 REF-C2 and the two CMIP6 scenarios. This relationship seems to be slightly weaker in the NH

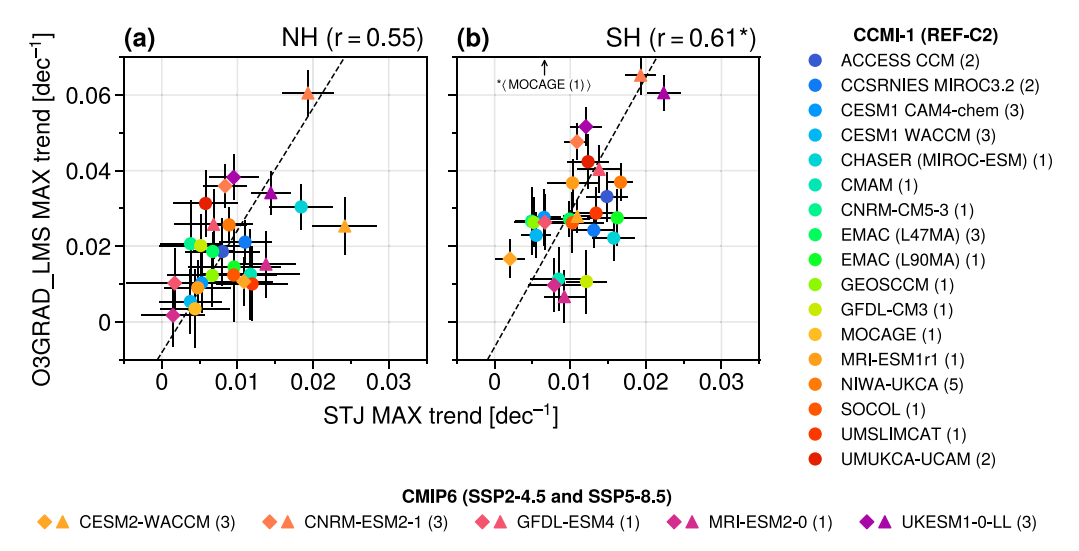


FIG. 8. O3GRAD_LMS MAX ozone gradient trends from CCMI-1 and CMIP6 simulations (NH DJF and SH JJA, 2015–98) plotted against the projected STJ strengthening (STJ MAX), each shown relative to climatology (1 decade⁻¹). Diamond (triangle) markers show the results for the CMIP6 SSP2-4.5 (SSP5-8.5) runs. Note that for the SH, trends obtained from the MOCAGE model projecting an ozone gradient strengthening of approximately 0.12 decade⁻¹ (cf. Fig. 7d) are located outside of the figure's panel and therefore are not shown. Cross-model correlation coefficients with p values p < 0.01 are provided at the upper-right corner of each panel, where MOCAGE has not been used for the calculation in the SH (correlation coefficient drops to r = 0.24 with p = 0.22 if this outlier is included). The black dashed lines illustrate orthogonal distance regressions [ODRs; implementation based on scipy.odr by Virtanen et al. (2020)] that account for the trend uncertainties in both the predictand and the predictor. Error bars at each model marker show 95% confidence intervals for the trend regressions.

compared to the SH, but overall scales reasonably well with the degree of correlation found for interannual covariability from ERA5 reanalysis data in both hemispheres (cf. Fig. 2). The correlations mainly stem from the correlation across scenarios (i.e., different forcing strength), while the correlation between STJ MAX and O3GRAD_LMS MAX trends across the subset of 17 CCMI-1 models is not statistically significant (not shown). This suggests that the cross-model spread in the CCMI-1 trend projections may be associated with differences in model representations of the STJ-ozone covariability, likely linked to differences in the representation of transport processes.

In general, it is not a priori clear whether a linear relation between the response of the jet stream and meridional ozone gradients in the STJ region holds in a changing climate, in particular for strong climate forcing scenarios where large deviations from the historical mean state of the system are expected. Specifically, in addition to the contribution of horizontal mixing to subtropical ozone variability, indirect effects from other transport processes might amplify or dampen the ozone gradient response to STJ changes. For example, the STJ strength is closely linked to changes in wave driving, which influences both horizontal mixing and the advective transport circulation.

7. Summary and conclusions

In this paper, we investigated whether the distribution of monthly mean zonal-mean ozone in the upper troposphere and lower stratosphere (UTLS) can be used as an indicator of the dynamical variability of large-scale general circulation features. We presented different options for defining ozone-based diagnostics, which each measure the magnitude and meridional position of the maximum zonal-mean ozone gradients located near the subtropical tropopause of both hemispheres.

Using winter-mean ERA5 reanalysis data, we show that this approach yields a robust ozone gradient index, based on either the vertically resolved ozone structure or total-column ozone (TCO) profiles, and is fairly independent of the exact configuration setup. For both hemispheres, we find a close correspondence in interannual variability between the meridional location of the subtropical jet stream (STJ) and the latitude of the maximum ozone gradient in the UTLS region and similar for the jet's zonal wind speed and the sharpness of these gradients. This is consistent with the jet core acting as a barrier for ozone transport governed primarily by waveinduced, quasi-isentropic mixing. Consistently, our results confirm that anomalies in STJ strength and position are coupled with modulations in the meridional gradients of both ozone and potential vorticity. However, advective ozone transport by the mean residual circulation may also indirectly change the magnitude of the ozone gradients as a response to anomalous wave driving (e.g., Abalos et al. 2017, 2020).

Our comparison with vertically resolved ozone observations from the SWOOSH dataset shows good agreement of the results derived from ozone measurements and ERA5 especially in more recent years, when densely sampled satellite observations allow accurate characterization of the global structure of vertically resolved ozone. Using 40 years of TCO records and the corresponding column ozone metrics, we demonstrate that historical STJ trends may indeed be constrained by observational tracer data and that this indirect approach may allow for further reduction in uncertainties arising from a multireanalysis assessment, provided that long-term and high-quality, global tracer measurements are available. For example, evidence is provided that nonsignificant or diverging results from reanalyses on the historical changes of the NH STJ can be narrowed down by robust trends in the observation-based TCO gradients; i.e., from TCO variations, we infer an annual-mean poleward jet shift of about 0.2° per decade and robust STJ weakening around -0.2 m s^{-1} decade⁻¹.

Finally, from our evaluation of CCMI-1 and selected CMIP6 climate models, we find that recent climate simulations properly reproduce the mode-like correlation signature found in ERA5, i.e., significant covariability within the two groups of diagnostics measuring either the magnitude or latitudinal movement of the STJ core, respectively, and the peak ozone gradients. This is also reflected by mostly consistent STJ and ozone gradient trend signatures obtained from CCMI-1 and CMIP6 climate projections based on different external forcing scenarios.

In conclusion, we showed that changes in zonal-mean ozone in the UTLS can be used to track interannual STJ variability from an atmospheric trace gas distribution in both hemispheres during winter and in the annual mean. Covariability between the STJ and the strong meridional ozone gradients in the STJ region is overall well captured by the two vertically resolved ozone gradient fields analyzed in this work, albeit this approach still suffers from the limited availability of observational ozone data. Additionally, some diverging results from observational records and recent climate simulations, potentially due to the limited vertical resolution of the data used, need to be treated with caution. The underlying metrics, however, are rather intuitive and can be easily brought together with our current understanding of STJ-ozone covariability. In contrast, the usage of TCO-based diagnostics a priori is less clear but indeed allows to constrain historical STJ trends from a much broader range of (observational) datasets. In this sense, potential users of the ozone gradient metrics may apply a combined approach whenever possible and carefully evaluate the underlying STJ-ozone correlations for each individual case.

Since the midlatitude eddy-driven jet (EDJ) is known to be coupled to the STJ through wave-driven dynamics, especially in the NH, this may allow to indirectly estimate EDJ variability from subtropical UTLS ozone. Figure 9 shows the anticorrelation between the STJ magnitude (STJ MAX) and the EDJ's latitudinal position (EDJ LAT) for 1980–2019, which is strong especially during NH winter (DJF) across four different reanalyses (cf. Fig. 2 for ERA5). Likewise, the covariability of EDJ LAT and the ozone gradient strength in the STJ region, as indicated by O3GRAD_LMS, O3ISO_TTP–3KM, and TCO (cf. Table 3), is significant during that time (based on ERA5 data). This could help to constrain interannual EDJ variability from ozone observations and may be compared,

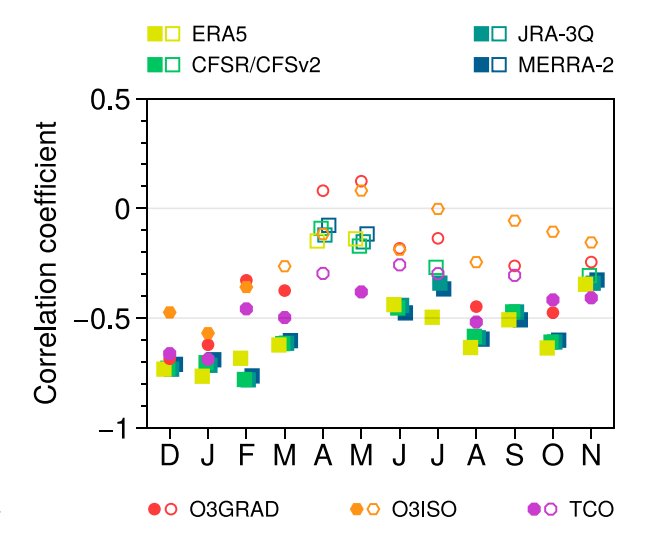


FIG. 9. Seasonal variability of NH correlation between STJ strength (STJ MAX) and EDJ position (EDJ LAT), derived from reanalysis data [1980–2019; S-RIP RID data by Martineau et al. (2018)] and shown by square markers, and ERA5 correlation between EDJ LAT and subtropical ozone gradient magnitudes, as measured by O3GRAD_LMS MAX (round markers), O3ISO_TTP–3KM (hexagons), and TCO MAX (octagons). The filled (open) markers indicate (non)significant correlation values at the 95% level.

e.g., to near-surface zonal wind measurements. We expect the weaker correlations during the summer months in Fig. 9 to arise from both the reduced coupling between the STJ and EDJ as well as from less unique, rather poorly pronounced meridional gradients in the STJ region (cf. appendix). In addition, the EDJ was found to feature a substantial correlation with the meridional mass streamfunction in the troposphere as a relevant metric of tropical width, which was not the case for the STJ (e.g., Davis and Birner 2017; Waugh et al. 2018). This correspondence with the EDJ may be used to further constrain historical tropical expansion trends from observational, ozone-based diagnostics.

We presented a new proxy diagnostic for STJ variability that can be constrained by ozone observations and that serves as a complementary metric of zonal-wind-based metrics from reanalyses, providing support to improve the quantification of essential climate trend signals. Our analysis requires sufficiently strong meridional ozone gradients, which currently limits the application of the ozone gradient metrics to wintermean and annual-mean data. Climate models show, however, that the underlying subtropical ozone gradients become more pronounced in a future climate, since changes in the STJ wind speeds and midlatitude wave activity can substantially influence UTLS ozone. Future work may also assess other atmospheric trace gases for constructing observation-based metrics of dynamical variability. In particular, long-lived trace species without considerable chemical sources or sinks in the UTLS may be suitable if a sufficient amount of observational data is available and the tracer's distribution features some characteristic

structure that can be continuously linked to the relevant mechanisms of the large-scale general circulation.

Acknowledgments. We thank Molly Menzel and one anonymous reviewer for their comments which significantly helped to improve this paper. We further thank P. Martineau for his support with the S-RIP RID data archive. FH acknowledges helpful discussions with J. Kim (Kongju National University) and P. Rupp (LMU Munich). This research has been supported by the Deutsche Forschungsgemeinschaft (DFG, German Research Foundation)—TRR 301—Project ID 428312742 ("The tropopause region in a changing atmosphere") and by the International Space Science Institute (ISSI) in Bern, Switzerland, through ISSI International Team project No. 460 ("Tropical Width Impacts on the Stratosphere"). We acknowledge the Chemistry-Climate Model Initiative (CCMI) modeling groups for making their simulations available for this analysis, the joint WCRP SPARC/ IGAC CCMI for organizing and coordinating the model data analysis activity, and the British Atmospheric Data Centre (BADC) for collecting and archiving the CCMI model output. We further acknowledge the World Climate Research Programme, which, through its Working Group on Coupled Modelling, coordinated and promoted CMIP6. We thank the climate modeling groups for producing and making available their model output, Earth System Grid Federation (ESGF) for archiving the data and providing access, and the multiple funding agencies who support CMIP6 and ESGF. We acknowledge the Python programming language and several additional software extensions therein that were used for computation. Figures have been created using Matplotlib (Hunter 2007), Pro-Plot (Davis 2021), and various additional color schemes distributed with these packages. We furthermore acknowledge the work by P. Conrat Fuentes (LMU Munich) on Python code for computing thermal tropopause heights that were partially used within this study.

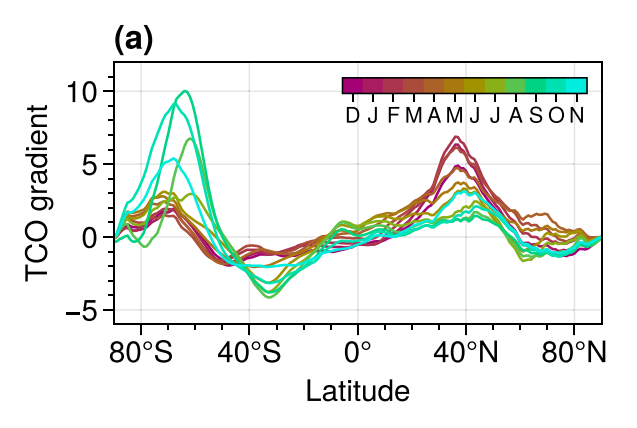
Data availability statement. Hersbach et al. (2023a,b) were downloaded from the Copernicus Climate Change Service (C3S) Climate Data Store (CDS). Additional reanalysis output was obtained from the S-RIP Reanalysis Intercomparison Dataset (RID) at https://www.jamstec.go.jp/ridinfo/, which is an updated version of the data published by Martineau et al. (2018). SWOOSH ozone data by Davis et al. (2016) can be accessed via https://csl.noaa.gov/groups/csl8/swoosh/. ESA Climate Change Initiative MSR data were downloaded from the C3S CDS. TCO data by Bodeker et al. (2021) are available from Bodeker et al. (2022). CCMI-1 model output was published by Hegglin et al. (2015). CMIP6 data were downloaded from the ESGF data network. This work contains modified Copernicus Climate Change Service information. Neither the European Commission nor ECMWF is responsible for any use that may be made of the Copernicus information or data it contains.

APPENDIX

Notes on the Seasonal Cycle

The ozone metrics discussed in section 2 have been constructed such that the subtropical maxima of the underlying

ozone gradient fields are clearly pronounced in the resulting latitudinal profiles. From Fig. 1, we find that this works well for all definitions when evaluating their long-term climatology limited to hemispheric winters. However, analyzing full monthly mean data requires to account for the substantial variability induced by the seasonal cycle. As an example, Fig. A1a shows monthly climatologies for the TCO meridional gradient profiles (ERA5, 1979–2023), illustrating regular fluctuations in the locations and strengths of the subtropical gradient maxima throughout the year. In particular, computing the ozone gradient diagnostics turned out to be challenging where unique maxima are missing.



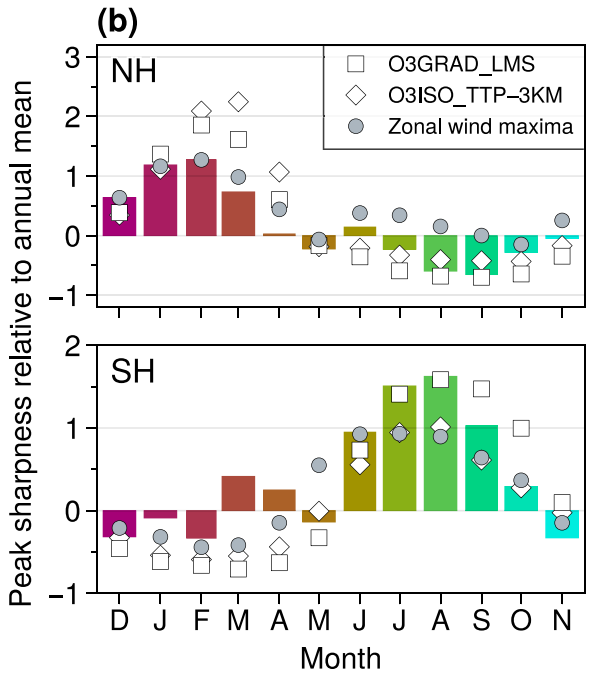


FIG. A1. (a) TCO meridional gradient climatologies (DU deg⁻¹) and as a function of month, based on ERA5 data (1979–2023). (b) Vertical bars illustrate seasonal fluctuations in the subtropical peak shape of the TCO profiles shown in (a) according to the peak sharpness measure defined in Eq. (1), calculated for each hemisphere separately. The white and gray markers show this cycle for the remaining two ozone gradient definitions and for the STJs' zonal-mean zonal wind vertical shear maxima, respectively.

We may quantify this finding by defining a "peak sharpness" P(m) as the ratio between the absolute magnitude of the subtropical gradient maximum and its full width at half maximum for a given monthly climatology $m=1, 2, \ldots, 12$. Then, the dimensionless measure,

$$\frac{P(m)}{P_{\text{clim}}} - 1, \tag{A1}$$

gives an estimate of the seasonal variation of the peak sharpness relative to the annual-mean climatology P_{clim} . For example, if $P(m) > P_{\text{clim}}$, the subtropical ozone maximum is better pronounced during month m than for the annual mean, and thus, peak-based metrics may be more robust during this month. Figure A1b provides this peak sharpness measure defined in Eq. (A1) for the different ozone gradient profiles as a function of month m. We note a clear seasonal cycle for all ozone-based metrics, suggesting enhanced "performance" during winter and early spring on each hemisphere. Furthermore, it turns out that the zonal-mean zonal wind vertical shear maxima, as constructed for the STJ LAT metric described in Table 2, show a similar, albeit less strongly pronounced, behavior. The peak sharpness may be additionally weakened by local monsoon effects during summer on the NH. This suggests that in general our findings need to be treated with caution if they potentially result from less unique structures of the zonal-mean variable fields.

REFERENCES

- Abalos, M., and A. de la Cámara, 2020: Twenty-first century trends in mixing barriers and eddy transport in the lower stratosphere. *Geophys. Res. Lett.*, **47**, e2020GL089548, https://doi.org/10.1029/2020GL089548.
- —, W. J. Randel, D. E. Kinnison, and R. R. Garcia, 2017: Using the artificial tracer e90 to examine present and future UTLS tracer transport in WACCM. *J. Atmos. Sci.*, 74, 3383–3403, https://doi.org/10.1175/JAS-D-17-0135.1.
- ——, and Coauthors, 2020: Future trends in stratosphere-to-troposphere transport in CCMI models. *Atmos. Chem. Phys.*, 20, 6883–6901, https://doi.org/10.5194/acp-20-6883-2020.
- Adam, O., and Coauthors, 2018a: The TropD software package (v1): Standardized methods for calculating tropical-width diagnostics. *Geosci. Model Dev.*, 11, 4339–4357, https://doi.org/ 10.5194/gmd-11-4339-2018.
- —, and Coauthors, 2018b: TropD: Tropical width diagnostics software package. Zenodo, https://doi.org/10.5281/zenodo.
- Bodeker, G. E., J. Nitzbon, J. S. Tradowsky, S. Kremser, A. Schwertheim, and J. Lewis, 2021: A global total column ozone climate data record. *Earth Syst. Sci. Data*, 13, 3885–3906. https://doi.org/10.5194/essd-13-3885-2021.
- —, S. Kremser, and J. S. Tradowsky, 2022: BS filled total column ozone database V3.4.1. Zenodo, accessed 10 January 2024, https://doi.org/10.5281/zenodo.7447757.
- Cariolle, D., and H. Teyssèdre, 2007: A revised linear ozone photochemistry parameterization for use in transport and general circulation models: Multi-annual simulations. *Atmos. Chem. Phys.*, 7, 2183–2196, https://doi.org/10.5194/acp-7-2183-2007.

- Chemke, R., and J. Yuval, 2023: Human-induced weakening of the Northern Hemisphere tropical circulation. *Nature*, **617**, 529–532, https://doi.org/10.1038/s41586-023-05903-1.
- Copernicus Climate Change Service, 2020: Ozone monthly gridded data from 1970 to present derived from satellite observations. Copernicus Climate Change Service (C3S) Climate Data Store (CDS), accessed 8 January 2024, https://doi.org/10.24381/cds.4ebfe4eb
- Davis, L. L. B., 2021: ProPlot Version v0.9.5. Zenodo, https://doi. org/10.5281/zenodo.3873878.
- Davis, N., and T. Birner, 2017: On the discrepancies in tropical belt expansion between reanalyses and climate models and among tropical belt width metrics. J. Climate, 30, 1211–1231, https://doi.org/10.1175/JCLI-D-16-0371.1.
- Davis, N. A., and T. Birner, 2013: Seasonal to multidecadal variability of the width of the tropical belt. J. Geophys. Res. Atmos., 118, 7773–7787, https://doi.org/10.1002/jgrd.50610.
- Davis, S. M., and Coauthors, 2016: The Stratospheric Water and Ozone Satellite Homogenized (SWOOSH) database: A longterm database for climate studies. *Earth Syst. Sci. Data*, 8, 461–490, https://doi.org/10.5194/essd-8-461-2016.
- ——, B. Hassler, and K. H. Rosenlof, 2018: Revisiting ozone measurements as an indicator of tropical width. *Prog. Earth Planet. Sci.*, 5, 56, https://doi.org/10.1186/s40645-018-0214-5.
- —, and Coauthors, 2022: Overview of ozone and water vapour. SPARC Reanalysis Intercomparison Project (S-RIP) Final Rep. SPARC Rep. 10, WCRP-17/2020, 123–164, https://doi. org/10.17874/800dee57d13.
- ECMWF, 2016: Part IV: Physical processes. IFS Documentation CY41R2, ECMWF, 213 pp., https://doi.org/10.21957/tr5rv27xu.
- Eyring, V., and Coauthors, 2013: Overview of IGAC/SPARC Chemistry-Climate Model Initiative (CCMI) community simulations in support of upcoming ozone and climate assessments. SPARC Newsletter, No. 40, SPARC Office, Toronto, Ontario, Canada, 48–66, https://www.aparc-climate.org/publications/newsletter/.
- —, S. Bony, G. A. Meehl, C. A. Senior, B. Stevens, R. J. Stouffer, and K. E. Taylor, 2016: Overview of the Coupled Model Intercomparison Project Phase 6 (CMIP6) experimental design and organization. *Geosci. Model Dev.*, 9, 1937–1958, https://doi.org/10.5194/gmd-9-1937-2016.
- Grise, K. M., and Coauthors, 2019: Recent tropical expansion: Natural variability or forced response? *J. Climate*, 32, 1551–1571, https://doi.org/10.1175/JCLI-D-18-0444.1.
- Hegglin, M. I., J. F. Lamarque, and V. Eyring, 2015: The IGAC/ SPARC Chemistry-Climate Model Initiative Phase-1 (CCMI-1) model data output. NCAS British Atmospheric Data Centre, accessed 30 January 2025, https://catalogue.ceda.ac.uk/uuid/9cc 6b94df0f4469d8066d69b5df879d5.
- Hersbach, H., and Coauthors, 2020: The ERA5 global reanalysis. *Quart. J. Roy. Meteor. Soc.*, **146**, 1999–2049, https://doi.org/10.1002/qj.3803.
- —, and Coauthors, 2023a: ERA5 monthly averaged data on pressure levels from 1940 to present. Copernicus Climate Change Service (C3S) Climate Data Store (CDS), accessed 24 April 2024, https://doi.org/10.24381/cds.6860a573.
- —, and Coauthors, 2023b: ERA5 monthly averaged data on single levels from 1940 to present. Copernicus Climate Change Service (C3S) Climate Data Store (CDS), accessed 25 April 2024, https://doi.org/10.24381/cds.f17050d7.
- Hudson, R. D., 2012: Measurements of the movement of the jet streams at mid-latitudes, in the Northern and Southern

- Hemispheres, 1979 to 2010. *Atmos. Chem. Phys.*, **12**, 7797–7808, https://doi.org/10.5194/acp-12-7797-2012.
- —, A. D. Frolov, M. F. Andrade, and M. B. Follette, 2003: The total ozone field separated into meteorological regimes. Part I: Defining the regimes. *J. Atmos. Sci.*, **60**, 1669–1677, https://doi.org/10.1175/1520-0469(2003)060<1669:TTOFSI>2.0.CO;2.
- —, M. F. Andrade, M. B. Follette, and A. D. Frolov, 2006: The total ozone field separated into meteorological regimes—Part II: Northern Hemisphere mid-latitude total ozone trends. *Atmos. Chem. Phys.*, 6, 5183–5191, https://doi.org/10.5194/acp-6-5183-2006.
- Hunter, J. D., 2007: Matplotlib: A 2D graphics environment. Comput. Sci. Eng., 9, 90–95, https://doi.org/10.1109/MCSE. 2007.55
- Keeble, J., and Coauthors, 2021: Evaluating stratospheric ozone and water vapour changes in CMIP6 models from 1850 to 2100. Atmos. Chem. Phys., 21, 5015–5061, https://doi.org/10. 5194/acp-21-5015-2021.
- Lait, L. R., 1994: An alternative form for potential vorticity. J. Atmos. Sci., 51, 1754–1759, https://doi.org/10.1175/1520-0469 (1994)051<1754:AAFFPV>2.0.CO;2.
- Lee, J.-Y., and Coauthors, 2021: Future global climate: Scenario-based projections and near-term information. *Climate Change 2021: The Physical Science Basis*, V. Masson-Delmotte et al., Eds., Cambridge University Press, 553–672, https://doi.org/10.1017/9781009157896.006.
- Lee, S., and H.-K. Kim, 2003: The dynamical relationship between subtropical and eddy-driven jets. *J. Atmos. Sci.*, **60**, 1490–1503, https://doi.org/10.1175/1520-0469(2003)060<1490:TDRB SA>2.0.CO;2.
- Leith, C. E., 1975: Climate response and fluctuation dissipation. *J. Atmos. Sci.*, **32**, 2022–2026, https://doi.org/10.1175/1520-0469(1975)032<2022:CRAFD>2.0.CO;2.
- Limpasuvan, V., and D. L. Hartmann, 1999: Eddies and the annular modes of climate variability. *Geophys. Res. Lett.*, 26, 3133–3136, https://doi.org/10.1029/1999GL010478.
- Long, C., M. Fujiwara, S. Davis, D. Mitchell, and C. Wright, 2022: Overview of temperature and winds. SPARC Reanalysis Intercomparison Project (S-RIP) Final Rep. SPARC Rep. 10, WCRP-17/2020, 81–122, https://doi.org/10.17874/800dee57d13.
- Long, C. S., M. Fujiwara, S. Davis, D. M. Mitchell, and C. J. Wright, 2017: Climatology and interannual variability of dynamic variables in multiple reanalyses evaluated by the SPARC Reanalysis Intercomparison Project (S-RIP). Atmos. Chem. Phys., 17, 14593–14629, https://doi.org/10.5194/acp-17-14593-2017.
- Lorenz, D. J., and D. L. Hartmann, 2001: Eddy–zonal flow feed-back in the Southern Hemisphere. J. Atmos. Sci., 58, 3312–3327, https://doi.org/10.1175/1520-0469(2001)058<3312:EZFF IT>2.0.CO:2.
- —, and —, 2003: Eddy-zonal flow feedback in the Northern Hemisphere winter. J. Climate, 16, 1212–1227, https://doi.org/ 10.1175/1520-0442(2003)16<1212:EFFITN>2.0.CO;2.
- Martineau, P., J. S. Wright, N. Zhu, and M. Fujiwara, 2018: Zonal-mean data set of global atmospheric reanalyses on pressure levels. *Earth Syst. Sci. Data*, 10, 1925–1941, https://doi.org/10.5194/essd-10-1925-2018.
- Meinshausen, M., and Coauthors, 2020: The shared socioeconomic pathway (SSP) greenhouse gas concentrations and their extensions to 2500. *Geosci. Model Dev.*, **13**, 3571–3605, https://doi.org/10.5194/gmd-13-3571-2020.
- Menzel, M. E., D. Waugh, and K. Grise, 2019: Disconnect between Hadley cell and subtropical jet variability and response

- to increased CO₂. *Geophys. Res. Lett.*, **46**, 7045–7053, https://doi.org/10.1029/2019GL083345.
- —, D. W. Waugh, Z. Wu, and T. Reichler, 2024: Replicating the Hadley cell edge and subtropical jet latitude disconnect in idealized atmospheric models. *Wea. Climate Dyn.*, 5, 251–261, https://doi.org/10.5194/wcd-5-251-2024.
- Ming, A., 2022: PyTropD version 2.12. GitHub, accessed 6 February 2024, https://github.com/TropD/pytropd.
- Morgenstern, O., and Coauthors, 2017: Review of the global models used within phase 1 of the Chemistry–Climate Model Initiative (CCMI). *Geosci. Model Dev.*, **10**, 639–671, https://doi.org/10.5194/gmd-10-639-2017.
- O'Neill, B. C., and Coauthors, 2016: The Scenario Model Intercomparison Project (ScenarioMIP) for CMIP6. *Geosci. Model Dev.*, 9, 3461–3482, https://doi.org/10.5194/gmd-9-3461-2016.
- Riahi, K., and Coauthors, 2017: The Shared Socioeconomic Pathways and their energy, land use, and greenhouse gas emissions implications: An overview. *Global Environ. Change*, **42**, 153–168, https://doi.org/10.1016/j.gloenvcha.2016.05.009.
- Schneider, T., 2006: The general circulation of the atmosphere. *Annu. Rev. Earth Planet. Sci.*, **34**, 655–688, https://doi.org/10.1146/annurev.earth.34.031405.125144.
- Shaw, T. A., 2019: Mechanisms of future predicted changes in the zonal mean mid-latitude circulation. *Curr. Climate Change Rep.*, 5, 345–357, https://doi.org/10.1007/s40641-019-00145-8.
- —, and O. Miyawaki, 2024: Fast upper-level jet stream winds get faster under climate change. *Nat. Climate Change*, **14**, 61–67, https://doi.org/10.1038/s41558-023-01884-1.
- —, and Coauthors, 2024: Emerging climate change signals in atmospheric circulation. AGU Adv., 5, e2024AV001297, https://doi.org/10.1029/2024AV001297.
- Shepherd, T. G., and C. McLandress, 2011: A robust mechanism for strengthening of the Brewer–Dobson circulation in response to climate change: Critical-layer control of subtropical wave breaking. J. Atmos. Sci., 68, 784–797, https://doi.org/10. 1175/2010JAS3608.1.
- Staten, P. W., J. Lu, K. M. Grise, S. M. Davis, and T. Birner, 2018: Re-examining tropical expansion. *Nat. Climate Change*, 8, 768–775, https://doi.org/10.1038/s41558-018-0246-2.
- Taylor, K. E., R. J. Stouffer, and G. A. Meehl, 2012: An overview of CMIP5 and the experiment design. *Bull. Amer. Meteor.* Soc., 93, 485–498, https://doi.org/10.1175/BAMS-D-11-00094.1.
- Thompson, D. W. J., and J. M. Wallace, 1998: The Arctic Oscillation signature in the wintertime geopotential height and temperature fields. *Geophys. Res. Lett.*, 25, 1297–1300, https://doi.org/10.1029/98GL00950.
- —, and —, 2000: Annular modes in the extratropical circulation. Part I: Month-to-month variability. *J. Climate*, 13, 1000–1016, https://doi.org/10.1175/1520-0442(2000)013<1000: AMITEC>2.0.CO;2.
- Totz, S., S. Petri, J. Lehmann, and D. Coumou, 2018: Regional changes in the mean position and variability of the tropical edge. *Geophys. Res. Lett.*, 45, 12076–12084, https://doi.org/10. 1029/2018GL079911.
- Vallis, G. K., P. Zurita-Gotor, C. Cairns, and J. Kidston, 2015: Response of the large-scale structure of the atmosphere to global warming. *Quart. J. Roy. Meteor. Soc.*, **141**, 1479–1501, https://doi.org/10.1002/qj.2456.
- Van Roozendael, M., and Coauthors, 2021a: Ozone Algorithm Theoretical Basis Document (ATBD), version 2.1. Copernicus Climate Change Service, accessed 2 May 2025, https://dast. copernicus-climate.eu/documents/satellite-ozone/C3S2_312b_

- Lot2_2024/C3S2_312a_Lot2_D-WP2_FDDP-PQAR_202311_O3_v3.3_final.pdf.
- —, and Coauthors, 2021b: Ozone Product User Guide and Specification (PUGS), version 2.1. Copernicus Climate Change Service, accessed 2 May 2025, https://dast.copernicus-climate.eu/documents/satellite-ozone/C3S2_312b_Lot2_2024/C3S2_312a_Lot2_D-WP2-FDDP-PUGS_202311_O3_v3.5_final.pdf.
- Virtanen, P., and Coauthors, 2020: Scipy 1.0: Fundamental algorithms for scientific computing in Python. *Nat. Methods*, 17, 261–272, https://doi.org/10.1038/s41592-019-0686-2.
- Waters, J. W., and Coauthors, 2006: The Earth observing system microwave limb sounder (EOS MLS) on the aura satellite. *IEEE Trans. Geosci. Remote Sens.*, 44, 1075–1092, https://doi. org/10.1109/TGRS.2006.873771.
- Waugh, D. W., and Coauthors, 2018: Revisiting the relationship among metrics of tropical expansion. *J. Climate*, 31, 7565– 7581, https://doi.org/10.1175/JCLI-D-18-0108.1.

- WMO, 1957: Meteorology—A three-dimensional science. Second session of the Commission for Aerology. WMO Bull., 6, 134–138.
- —, 2011: Scientific assessment of ozone depletion: 2010. Global Ozone Research and Monitoring Project Rep. 52, WMO, 442 pp.
- Woollings, T., 2016: Storm tracks, blocking, and climate change: A review. *Dynamics and Predictability of Large-Scale, High-Impact Weather and Climate Events*, J. Li et al., Eds., Cambridge University Press, 113–121, https://doi.org/10.1017/CBO9781107775541.009.
- —, M. Drouard, C. H. O'Reilly, D. M. H. Sexton, and C. McSweeney, 2023: Trends in the atmospheric jet streams are emerging in observations and could be linked to tropical warming. *Commun. Earth Environ*, 4, 125, https://doi.org/10.1038/s43247-023-00792-8.
- Zappa, G., 2019: Regional climate impacts of future changes in the mid-latitude atmospheric circulation: A storyline view. *Curr. Climate Change Rep.*, 5, 358–371, https://doi.org/10. 1007/s40641-019-00146-7.

Chapter 4

Paper III

Publication details

This manuscript has been sent to the journal "Atmospheric Chemistry and Physics" for publication and was published as preprint for peer-review and discussion.

Title: Adiabatic versus diabatic transport contributions to the

ozone budget in the northern hemispheric upper troposphere

and lower stratosphere [preprint]

Authors: Frederik Harzer, Hella Garny, Felix Ploeger,

J. Moritz Menken and Thomas Birner

DOI: https://doi.org/10.5194/egusphere-2025-2195

Author contributions

"FH conducted the analyses and prepared the first draft of the manuscript. He was supervised by HG and TB. FP provided pre-processed ERA5 reanalysis data on model levels and advice for the subsequent data processing. MM provided the EMAC model output. All authors helped to improve the manuscript." (Paper III, p. 17)

Copyright information

This work was published under the Creative Commons Attribution 4.0 license (details on this license are available at https://creativecommons.org/licenses/by/4.0/).

55





Adiabatic versus diabatic transport contributions to the ozone budget in the northern hemispheric upper troposphere and lower stratosphere

Frederik Harzer¹, Hella Garny², Felix Ploeger^{3,4}, J. Moritz Menken², and Thomas Birner^{1,2}

Correspondence: Frederik Harzer (frederik.harzer@physik.lmu.de)

Abstract. Ozone in the extratropical lowermost stratosphere (LMS) is important for the local radiative balance and contributes to the tropospheric and near-surface ozone burden via stratosphere–troposphere exchange. Here, we aim to deepen our understanding of the transport contributions to LMS ozone in the Northern Hemisphere by studying the ozone budget in isentropic coordinates, which allows for a clean distinction of adiabatic and diabatic transport contributions. This is done by analyzing 20 years of ERA5 reanalysis output on model levels and a free-running simulation using the EMAC chemistry–climate model. Our analysis confirms that the ozone tendencies in the extratropical LMS at high latitudes are dominated by diabatic mean flow advection (associated with downwelling within the Brewer–Dobson circulation) and quasi-horizontal adiabatic eddy mixing due to planetary- and medium-scale Rossby waves. These transport contributions are somewhat weaker during summer compared to winter, although seasonality is found to be weaker in the LMS compared to higher altitudes. Horizontal mean flow advection is found to be relevant near the tropopause and just above the subtropical jet core. Notably, vertical (i. e., diabatic) eddy ozone transport is found to be important near the tropopause. While the adiabatic eddy ozone fluxes in the LMS are consistent with diffusive, down-gradient eddy transport, the vertical eddy ozone transport also features up-gradient regions, which by itself would act to reinforce the background ozone gradients near the tropopause. Closer analysis reveals that this is due to long-wave radiative damping of planetary waves, which acts to dampen the down-gradient horizontal eddy transport.

15 1 Introduction

Atmospheric ozone is known to impact life on Earth by its effects, e. g., on short-wave solar radiation, air quality and surface climate (e. g. WMO, 2022). It is mainly produced through photolysis in the tropical lower stratosphere (Chapman, 1929) and globally distributed throughout the stratosphere by the Brewer–Dobson circulation (BDC; e. g., Plumb, 2002; Butchart, 2014). Stratospheric ozone is not only important for the local radiative balance, but via stratosphere–troposphere exchange of air masses also contributes to the tropospheric ozone burden (e. g. Holton et al., 1995). This stratospheric contribution to tropospheric ozone crucially depends on the amount of ozone in the lowermost stratosphere (LMS; e. g., Albers et al., 2018). Since ozone in the LMS is primarily governed by transport, a detailed understanding of the different transport contributions is

¹Meteorological Institute, Ludwig-Maximilians-Universität München, Munich, Germany

²Deutsches Zentrum für Luft- und Raumfahrt, Institut für Physik der Atmosphäre, Oberpfaffenhofen, Germany

³Institute of Climate and Energy Systems, Stratosphere (ICE-4), Forschungszentrum Jülich, Jülich, Germany

⁴Institute for Atmospheric and Environmental Research, University of Wuppertal, Wuppertal, Germany



25



critical and may ultimately also allow to consistently explain ozone trends derived from historical observations and from recent chemistry–climate simulations (e. g., Ball et al., 2019, 2020; Dietmüller et al., 2021).

Past research has shown that vertical advection by the diabatic mean flow (associated with up- and downwelling within the BDC), as well as adiabatic quasi-horizontal eddy mixing associated with dissipating Rossby waves are dominant transport contributions to lower stratospheric ozone (e. g., Plumb, 2002). At the same time, contributions by adiabatic horizontal mean flow advection and diabatic vertical eddy transport are usually considered to be less relevant. However, this picture may not be as valid near the extratropical tropopause due to the strong background gradients there (e. g., Gettelman et al., 2011) and the potential impact of smaller scale tropospheric dynamics.

In this paper, we aim to improve our knowledge on the transport contributions to LMS ozone from a tracer budget perspective in isentropic coordinates. Here, the isentropic coordinate framework allows to cleanly separate diabatic and adiabatic transport contributions and may therefore help to isolate the effects associated with the individual transport processes in the upper troposphere and lower stratosphere (UTLS). To do so, we use recent ERA5 reanalysis data as a reference of the quasi-observed atmospheric circulation and historical climate variability. Since the representation of ozone may be problematic in ERA5 due to the simplified chemistry scheme and limited ozone data assimilation, we also study a free-running chemistry-climate model (CCM) with state-of-the-art representation of ozone chemistry. We document the climatologies of ozone transport in the LMS of the Northern Hemisphere, contrasting winter and summer, and work out structural characteristics of these transport contributions as a function of horizontal scale. Note that we do not intend to provide a thorough assessment of the performance of the CCM compared to ERA5 in this study.

The structure of this paper is as follows: Section 2 describes the data and methods used in this work. In Sect. 3, we discuss the theoretical framework of the ozone budget approach and compare climatologies of the different ozone transport contributions. We then study aspects of eddy ozone transport separately and in more detail in Sect. 4. Section 5 provides the summary of our results and conclusions.

45 2 Data and methods

We use 6-hourly snapshots of ECMWF fifth generation reanalysis (ERA5) data on 137 vertical model levels with 1° horizontal resolution (Hersbach et al., 2017, 2020), which we interpolated onto isentropic levels with their vertical distance increasing with height (e. g., 39 levels between 300 K and 400 K with vertical resolution increasing from 1.25 K to 5 K). These isentropic levels were chosen to roughly match the model's actual vertical resolution based on a global mean climatology of potential temperature. We consider the time period 2000–2019 to align with the CCM simulation range (see below), which should be sufficiently long to study transport climatologies. We use updated ERA5.1 reanalysis data during 2000–2006, released by ECMWF due to substantial temperature biases in the lower stratosphere found in ERA5 for that time (Simmons et al., 2020). ERA5 is based on ECMWF's Integrated Forecasting System (IFS) version Cy41r2, which uses the linearized ozone parameterization by Cariolle and Teyssèdre (2007) and includes different monthly ozone climatologies based on external reanalysis data to be considered in the radiation parametrization (ECMWF, 2016; Hersbach et al., 2020). Davis et al. (2017, 2022) showed





that stratospheric ozone in ERA5 agrees reasonably well with observations, especially in more recent years when Aura MLS satellite measurements (Waters et al., 2006) were available for data assimilation.

Note that some variables in ERA5 are only provided as IFS forecast output, i. e., without assimilation of observational data. In particular, this holds true for the total diabatic heating rates examined in this study: these were derived from the ERA5 forecast data (variable "time-mean temperature tendency due to parametrisations", labeled "mttpm" in ERA5; cf. ECMWF, 2025), and include all contributions associated with long-wave and short-wave radiation under full-sky conditions, latent heat release, and heating due to turbulence and mixing processes. Here, the forecast temperature tendency was converted into a diabatic heating rate following Ploeger et al. (2021), including an averaging over 6-hour windows centered on each synoptic time (00, 06, 12, and 18UTC) to accurately represent 6-hourly mean heating rates. For further process analysis, diabatic heating rates have been derived similarly for full-sky and clear-sky radiative heating only, respectively.

Furthermore, we consider 5-hourly instantaneous global model output from a free-running ECHAM/MESSy Atmospheric Chemistry (EMAC) simulation (Roeckner et al., 2003, 2006; Jöckel et al., 2010) for the time period 2000–2019 with two years of spin-up. The simulation was forced by sea surface temperatures and sea ice concentrations taken from ERA5 reanalysis data and was performed with a spherical truncation T42 of the spectral dynamical core, corresponding to a quadratic Gaussian grid horizontal resolution of approx. 2.8° in latitude and longitude, and with 90 vertical hybrid sigma-pressure levels covering the atmosphere from the surface up to the mesosphere. The overall model configuration originates from a previous EMAC simulation prepared for the Chemistry–Climate Model Initiative (CCMI-2022), which itself was based on the setup used within the "Earth System Chemistry integrated Modelling" (ESCiMo) initiative (Jöckel et al., 2016) and updated to align with the new CCMI-2022 guidelines and recent submodel developments (Jöckel et al., 2024). Major differences between that setup for CCMI-2022 and the EMAC configuration used here, next to further submodel updates, refer to the additional application of the tropospheric aerosol model GMXe (Pringle et al., 2010) and the boundary conditions for ozone-depleting substances. The latter differ from the actual CCMI-2022 requirements (e. g., Plummer et al., 2021): until 2014, they are taken only from observation-based Climate Model Intercomparison Project phase 6 (CMIP6) forcing data (Meinshausen et al., 2017) and include the species CH₂Cl₂ and CHCl₃. From 2015 onwards, we apply the boundary conditions for greenhouse gases and ozone-depleting substances from the CMIP6 SSP2-4.5 scenario (Meinshausen et al., 2020).

A complete list of the EMAC submodels used in our model configuration is provided in the supplemental material of this paper (Table S1). The simulation features interactive chemistry and online computation of the radiation budget based on instantaneous tracer field values (Sander et al., 2014, 2019; Dietmüller et al., 2016). Note, however, that the total diabatic heating rates were not available in the model output and therefore had to be approximated from 5-hourly model data afterwards by computing the total derivative of the temperature field on model levels for each time step. Furthermore, although EMAC's vertical resolution is slightly lower than that of ERA5, we interpolated the EMAC model output onto the same isentropic levels as for ERA5 in order to facilitate the comparison of the individual analyses. Consequently, this led to slight vertical oversampling of the EMAC data.

Figure 1 provides an overview of the winter-mean ozone gradients in the northern hemispheric UTLS relative to climatological ozone for ERA5 and EMAC (DJF, 2000–2019). The relevance of these gradients for ozone transport through the





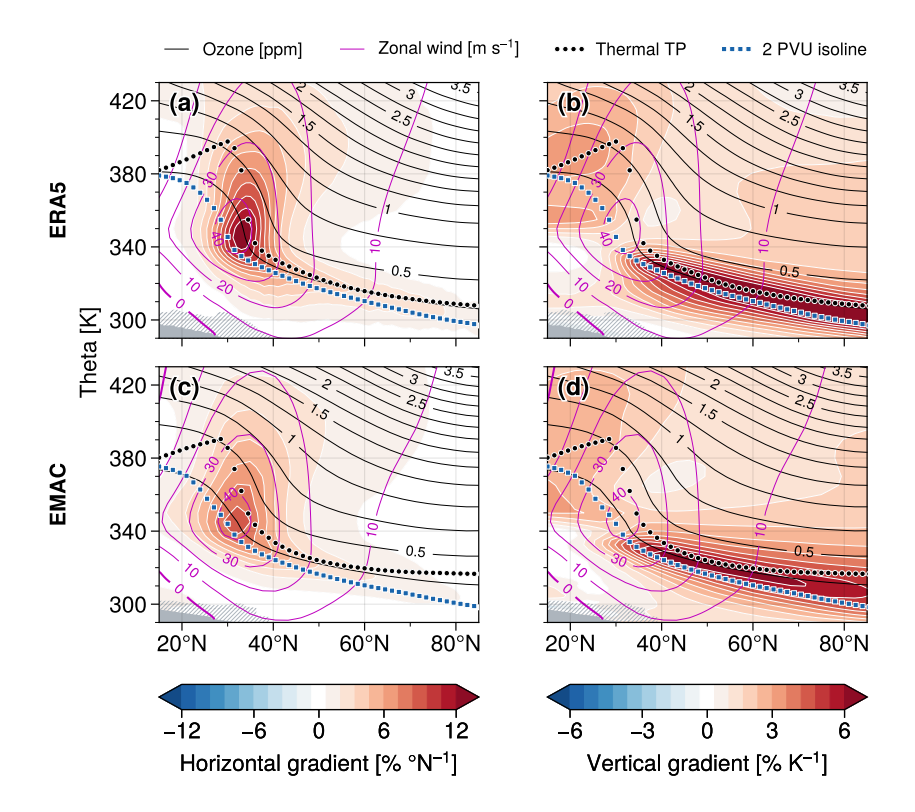


Figure 1. Winter-mean climatologies of (a) horizontal and (b) vertical zonal-mean ozone gradients (colors), respectively, as obtained from ERA5 reanalysis data (DJF, 2000–2019). (c, d) Same as in (a, b) but for the EMAC simulation. Gradient magnitudes are provided relative to the corresponding winter-mean, density-weighted ozone climatology (shown by the black contours). Violet contour lines represent climatologies of the zonal-mean zonal wind. Thermal tropopause heights following the WMO (1957) tropopause definition and 2 PVU potential vorticity isolines are shown by the thick dotted meridional profiles. Grey hatches close to the surface indicate grid points in the lower troposphere where monthly-mean data were missing for more than 40 % of the winter months considered here.

residual stratospheric circulation and eddy dynamics will be discussed in detail in subsequent sections. At this point, we note that the local maxima of both the horizontal and vertical gradients in the subtropics and along the extratropical tropopause are substantially weaker in EMAC compared to ERA5. This is likely due to the much coarser resolution in EMAC compared to in ERA5.





95 3 Climatologies of the transport contributions to the LMS ozone budget

The general expression of local changes of a given zonal-mean tracer distribution with time can be derived by combining the mass conservation and tracer continuity equations, and in isentropic spherical coordinates reads

$$\partial_t \overline{\chi}^* + \frac{\overline{v}^*}{a} \partial_\phi \overline{\chi}^* + \overline{Q}^* \partial_\theta \overline{\chi}^* = -\overline{\rho_\theta}^{-1} \left[\frac{1}{a \cos \phi} \partial_\phi \left(\overline{\hat{v}} \rho_\theta \hat{\chi} \cos \phi \right) + \partial_\theta \overline{\hat{Q}} \rho_\theta \hat{\chi} \right] + \overline{S}^*, \tag{1}$$

where $\rho_{\theta} = -g^{-1}\partial_{\theta}p$ is isentropic density, overbars (with asterisks) indicate (density-weighted) zonal averages and hat symbols denote deviations from the corresponding density-weighted zonal-mean quantities (Andrews et al., 1987; Plumb, 2002). The second and third term on the left-hand side represent advective transport by the horizontal (i. e., adiabatic in isentropic coordinates) and vertical (diabatic) mean flow, respectively. The first and second term on the right-hand side correspond to isentropic (i. e., adiabatic) and diabatic eddy transport, respectively. Finally, \overline{S}^* accounts for the effects of chemical sources and sinks of the tracer.

105 3.1 Winter-mean ozone transport

110

120

Figure 2 provides the northern hemisphere winter-mean ozone tendencies in the UTLS associated with the different transport contributions according to Eq. (1), contrasting results for ERA5 with EMAC. Overall, we find good agreement between the ERA5 and EMAC climatologies for each contribution, lending confidence to the robustness of the results. The ozone tendencies associated with vertical mean flow advection in the first row of Fig. 2 support our understanding of the stratospheric residual circulation, which transports ozone-rich air from higher altitudes into the extratropical LMS, with a tendency to accumulate ozone there throughout the winter season. These tendencies are somewhat inhomogeneous in the extratropical tropopause region in EMAC compared to ERA5 (cf. Fig. 2e vs. 2a), which may in part be due to uncertainties in off-line derived diabatic heating rates in EMAC. Furthermore, we note that these tendencies are substantially weaker at the tropopause in EMAC than in ERA5, consistent with the reduced vertical gradient magnitudes in EMAC (cf. Fig. 1b,d). We find a similar effect for the quasi-horizontal eddy transport contributions in the second row of Fig. 2, which feature a clear dipole signature centered around the extratropical tropopause with positive ozone tendencies in the subtropical upper troposphere and negative tendencies in the mid-latitude and polar LMS. These are consistent with horizontal two-way eddy mixing of ozone across positive meridional background gradients. Again, the peak tendencies near the tropopause appear to be reduced in EMAC compared to ERA5, whereas we find similar results in the lower stratosphere for altitudes higher than ~400 K.

Overall, the ozone tendencies associated with vertical transport by the mean flow and with horizontal eddy mixing illustrate that these are the most important mechanisms of stratospheric ozone transport during northern hemispheric winters. The third and fourth row of Fig. 2 suggest that the other transport contributions are relevant mostly in the subtropical UTLS and near the extratropical tropopause: panels 2c and 2g show negative tendencies due to meridional mean flow advection along the tropopause and above the STJ core. This is consistent with the upper branch of the tropospheric residual circulation acting on positive horizontal gradients of the background ozone distribution, i. e., the poleward mean flow is shifting air masses with smaller ozone mixing ratios towards higher latitudes. Vertical eddy transport causes a complex pattern of several local tendency





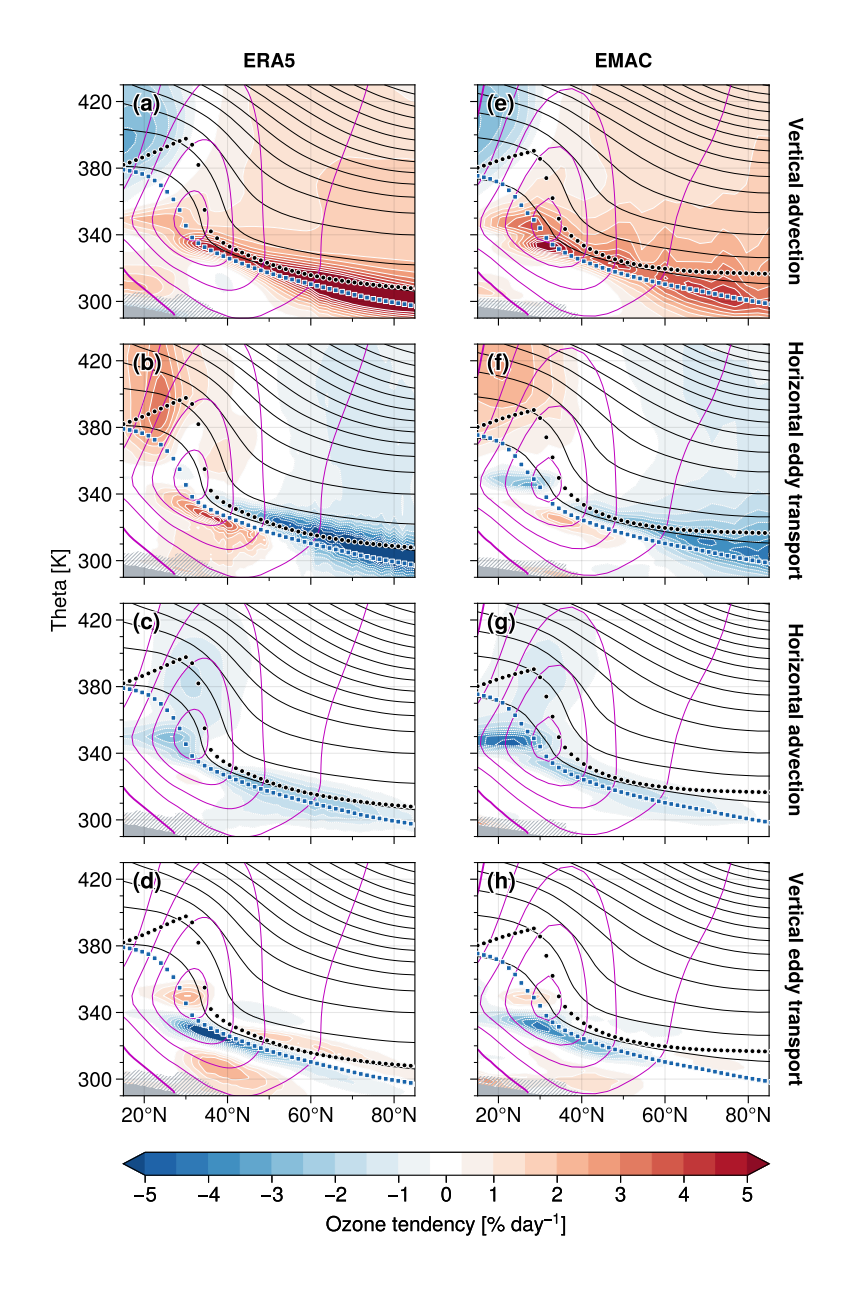


Figure 2. Ozone tendencies (colors) associated with mean flow advection and eddy transport in (**a-d**) ERA5 and (**e-h**) EMAC (DJF, 2000–2019), following the ozone budget approach from Eq. (1). Tendencies are given in units of % day⁻¹ relative to the corresponding zonal-mean ozone climatology. Other details as in Fig. 1.





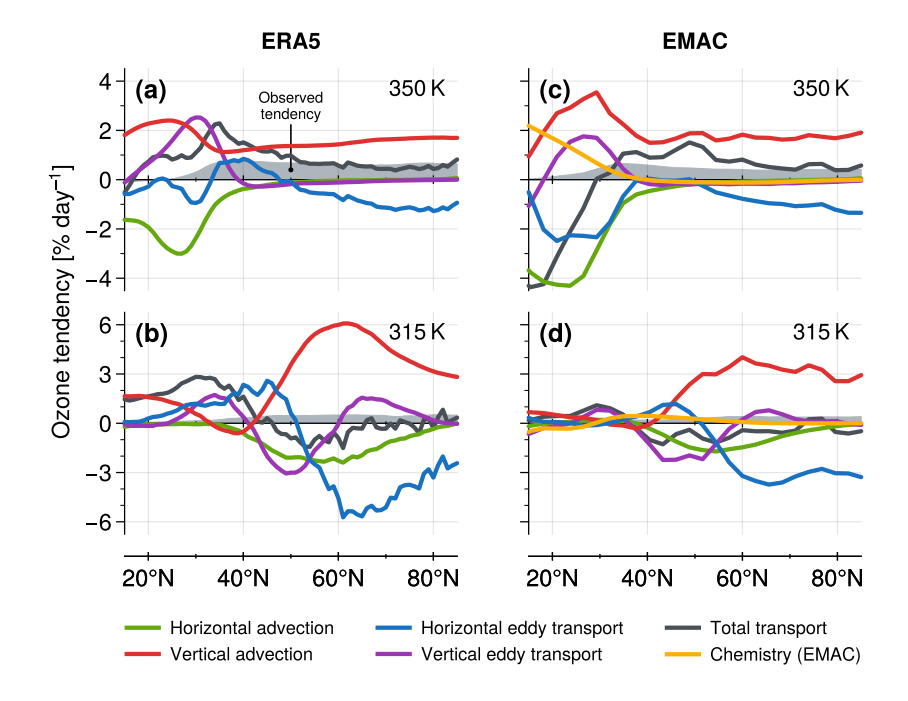


Figure 3. Meridional profiles of the ozone tendencies shown in Fig. 2 at 350 K (top row) and 315 K (bottom row). The net transport tendencies, accounting for all four transport contribution terms in Eq. (1), are shown as black lines. The tendencies due to ozone chemistry in EMAC are plotted yellow. Grey shading shows the total winter-mean tendency derived from the actual ozone distribution.

maxima and minima along the tropopause and in the upper troposphere (Fig. 2d,h). At this point, we refer to the more thorough discussion of eddy ozone transport in Sect. 4 below.

For a more quantitative comparison of the different ozone budget contributions, Fig. 3 provides meridional profiles of the climatological tendencies on two selected isentropic levels in the UTLS: 350 K, which connects the upper subtropical troposphere and lower extratropical stratosphere across the STJ core, as well as 315 K, which crosses the troposphere in the subtropics and the tropopause region in higher latitudes. For EMAC, we furthermore consider the available tendencies associated with ozone chemistry, \overline{S}^* in Eq. (1), shown by the yellow curves. Figure 3 shows that the total ozone tendency (grey shading) at 350 K in the LMS is mainly reproduced by the combined effects of vertical (diabatic) mean-flow advection and horizontal (adiabatic) eddy transport at higher latitudes (i. e., north of $\sim 60^{\circ}$ N). In contrast, for tropical to subtropical latitudes at 350 K, additional contributions by horizontal advection, vertical eddy transport and ozone chemistry become relevant. Here, the differences between ERA5 and EMAC in the subtropical upper troposphere suggest that reproducing the substantial contributions by tropospheric ozone chemistry and the complex interactions between the individual transport processes is rather challenging in that region. At 315 K, horizontal mean-flow advection and vertical eddy ozone transport contribute substantially even at extratropical latitudes, while the effects by ozone chemistry are rather small. Here, the meridional structures of the



145

160

165



different transport contributions are qualitatively similar for ERA5 and EMAC, whereas their local magnitudes are much larger for ERA5, again likely due to the stronger background ozone gradients along the tropopause there compared to EMAC.

Figure S1 in the supplement provides the ozone tendency profiles at 400 K and 800 K, illustrating the transport contributions by the shallow and deep branch of the residual BDC in the lower and middle stratosphere, respectively (e. g., Plumb, 2002; Birner and Bönisch, 2011; Baikhadzhaev et al., 2025). We find that substantial horizontal eddy transport in middle and higher latitudes is balanced mainly by vertical mean-flow advection at 400 K and ozone chemistry at 800 K, respectively, resulting in only very small total ozone tendencies during Boreal winter there. Furthermore, it is worth noting that meridional mean-flow advection removes (supplies) substantial amounts of ozone in the subtropics at 400 K (800 K), which is of potential relevance for supporting horizontal, wave-driven ozone transport by the BDC.

150 3.2 Seasonal variations of stratospheric ozone transport

Transport in the stratosphere is subject to substantial seasonal variability. In the following, we illustrate some aspects of seasonal variations of the different transport contributions to the zonal-mean ozone budget in the LMS.

Figure 4 shows the climatological ozone tendencies associated with advective transport and eddy dynamics as in Fig. 2, but now for northern hemispheric summer (June–August, 2000–2019). We find substantially reduced zonal-mean ozone gradients in the LMS compared to the winter months (black contours in Fig. 4) and reduced zonal wind speeds in the subtropical jet stream region that come along with a weaker tropopause break. The overall structures of the ozone tendencies, however, are qualitatively quite similar to those of Boreal winter (cf. Fig. 2). We note the following details in the climatologies for the summer season:

- substantial contributions by vertical advection due to the mean flow and horizontal eddy mixing in the tropopause region (of similar magnitude compared to winter, compare first and second rows of Fig. 2 and Fig. 4) as part of the shallow branch of the BDC, despite the expected strongly reduced tendencies at higher altitudes (above $\sim 360 \text{ K}$)
- strong dipole tendencies due to horizontal eddy mixing between the tropical upper troposphere and subtropical tropopause equatorward of $\sim 40^{\circ}$ N (second row), likely reflecting local Monsoon effects in the zonal-mean perspective (cf. Konopka et al., 2010; Abalos et al., 2013)
- reduced negative ozone tendencies due to meridional mean flow advection (third row) compared to winter, which is consistent with both a weaker residual tropospheric circulation and weaker horizontal ozone gradients
 - strong dipole signature in tropospheric and near-tropopause ozone tendencies due to vertical eddy transport (fourth row), indicating downward transport of stratospheric air masses with higher ozone concentrations that is even stronger compared to winter (cf. Yang et al., 2016)
- Next, in Fig. 5 we study the climatological meridional structure of the ozone transport contributions associated with mean flow advection and horizontal eddy transport as a function of time during the year at the isentrope that is located 50 K above the STJ core ($\approx 400 \text{ K}$ during Boreal winter), which is intended to follow the seasonality of the shallow branch of the BDC





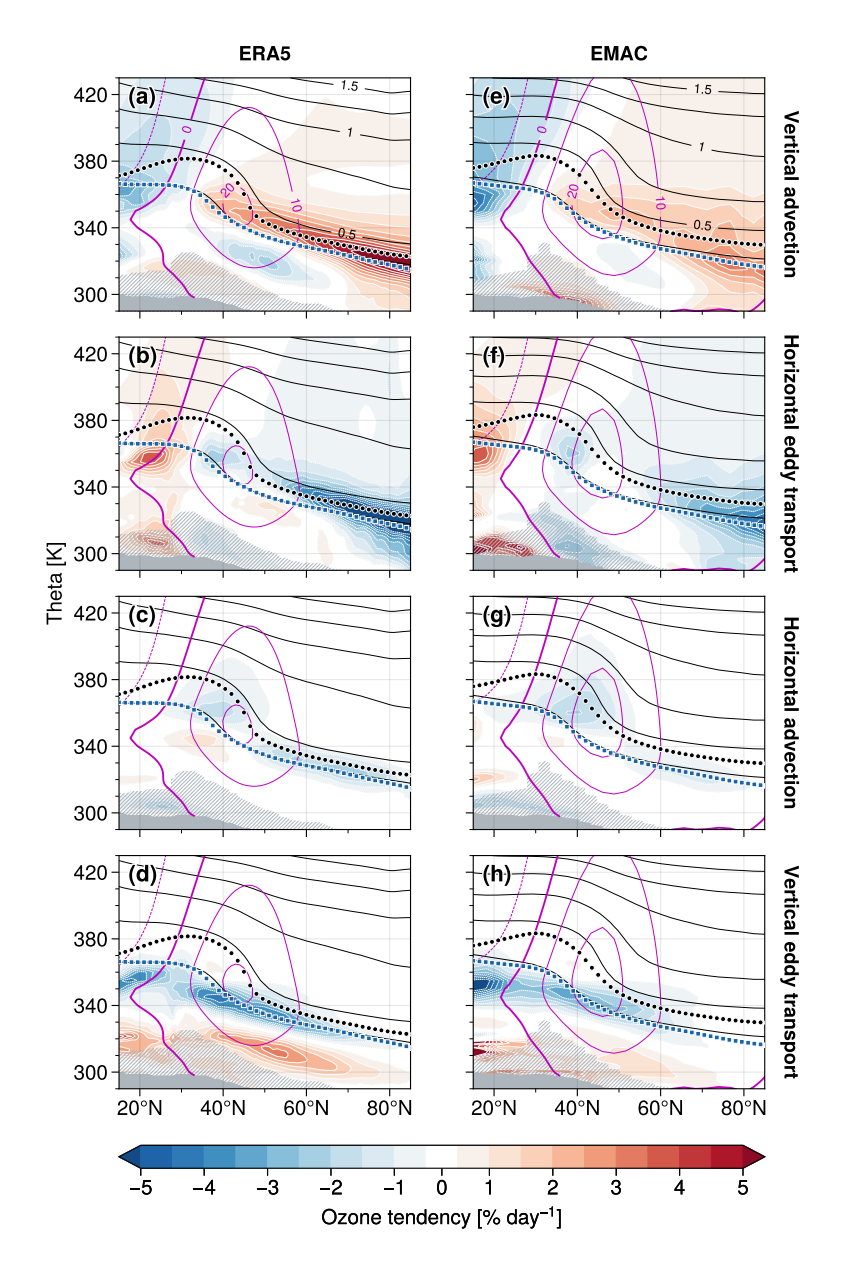


Figure 4. Same as Fig. 2 but for northern hemispheric summer (June-July-August).

in the lower stratosphere on a monthly basis (see the figure caption for more details on the computation). The results for the 800 K isentrope, tracking the seasonal cycle of the deep branch of the BDC, are available in the supplemental material. We do not consider vertical eddy mixing here since the associated contributions are rather small at these levels (cf. Fig. 3).



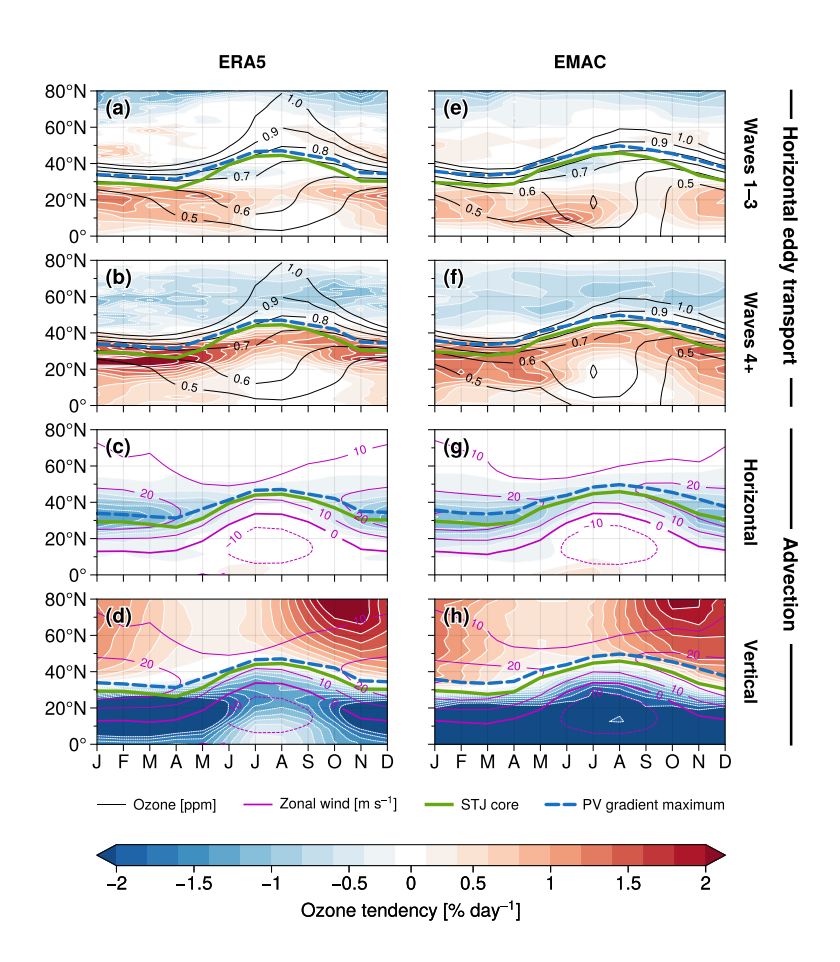


Figure 5. Climatologies of ozone tendencies (colors) associated with advection and horizontal eddy transport as a function of month during the year, each interpolated onto the isentrope 50 K above the STJ core, for ERA5 (left column) and EMAC (right column). Black contour lines in the upper two rows show the seasonal evolution of subtropical ozone (contours displayed for ozone values between 0.5 ppm and 1.0 ppm only). The violet contours provide the zonal-mean zonal wind climatologies. The green thick curves illustrate the meridional location of the STJ core, which corresponds to the maximum zonal wind shear relative to the 850 hPa zonal wind following the method by Davis and Birner (2013, 2017). The height of the STJ core is estimated from the corresponding zero-crossing of the vertical derivative (in log-*p* coordinates) of the zonal wind profile interpolated at the STJ's meridional position. The blue dashed lines show the position of the maximum meridional gradient of potential vorticity in the subtropics (derived from the corresponding zero-crossing of its meridional derivative) at the respective isentrope 50 K above the STJ.

In the upper two rows of Fig. 5, both ERA5 and EMAC show substantial equatorward eddy ozone transport across the subtropics, with only small seasonal variations. For the medium- to smaller-scale waves (wave numbers 4+), we find moderate modulations in the seasonal strength of ozone transport, with somewhat stronger transport during boreal winter and spring.



185

200

205



However, the dipole transport pattern follows the latitudinal shifting of the STJ throughout the year (green curves in Fig. 5), which is different to the transport signatures associated with planetary-scale waves (wave numbers 1–3). For the latter, we instead find slightly negative tendencies around 40°N during early summer, likely reflecting local Monsoon effects (cf. second row in Fig. 4). This is consistent with the high zonal wind speeds in the STJ region representing an effective barrier for tracer transport, as also illustrated by the time-dependent location of the meridional gradient maxima of potential vorticity (blue dashed lines in Fig. 5) that are closely aligned with the STJ core.

Panels 5c,g show negative ozone tendencies in the subtropics due to horizontal mean flow advection, which are somewhat weaker during summer. The seasonal cycle is in close correspondence with that of medium- to smaller-scale horizontal eddy transport (second row of Fig. 5), since both the residual flow and horizontal mixing are driven by wave dissipation at midlatitudes (e. g., Plumb, 2002). We found that the meridional mean flow in the lower stratosphere is slightly weaker during the summer months but continuously directed polewards throughout the whole year (not shown), suggesting rather minor seasonal changes in the dynamical drivers of transport there. Instead, the seasonality in ozone transport due to meridional advection and horizontal mixing seem to be mainly associated with seasonal variations of the strength of the STJ and, as a consequence, subtropical ozone gradients that limit the effectiveness of dynamical transport (ozone climatology shown by black contours in Fig. 5). In contrast, the substantial seasonal cycle of diabatic mean flow advection (panels 5d,h) likely is governed by the strong seasonality of large-scale planetary waves that propagate into the higher stratosphere (cf. Fig. S2 in the supplement) and that drive the deep branch of the BDC primarily during winter (Charney and Drazin, 1961; Plumb, 2002).

4 Eddy ozone transport in the UTLS

In this section, we have a closer look at the eddy contributions to the zonal-mean ozone budget in the LMS. Figure 6 provides the individual winter-mean *horizontal* eddy ozone fluxes associated with planetary waves (zonal wave numbers 1–3) and medium- to smaller-scale waves (wave numbers 4+)¹. Both ERA5 and EMAC show overall similar patterns with negative meridional ozone fluxes almost everywhere in the LMS, indicating equatorward eddy ozone transport (cf. Figs. 2 and 5), which is consistent with the well-known picture of diffusive, down-gradient eddy transport along the positive horizontal gradients of the background ozone distribution. We find the strongest ozone fluxes due to planetary-scale waves in the mid- to high latitudes along the tropopause, whereas medium- and smaller-scale wave activity acts mainly in the subtropics to mid-latitudes. However, since geometric wave lengths for a given zonal wave number decrease toward higher latitudes, we interpret the substantial negative ozone fluxes due to wave numbers 1–3 in the polar LMS also to be due to medium- and synoptic-scale wave activity.

For Boreal summer (June–August), we found somewhat weaker but still substantial horizontal eddy ozone transport in the tropopause region compared to winter (cf. Fig. S5). In the lower stratosphere, medium- to smaller scale waves contribute almost equally as during winter, whereas horizontal ozone fluxes associated with planetary waves are substantially reduced.

Figure 7 provides the winter-mean wave decompositions of the *vertical* eddy ozone flux. We find strong negative vertical ozone fluxes due to synoptic- and smaller-scale waves in the upper troposphere for both ERA5 and EMAC (Fig. 7b,d), with

¹derived from Fast Fourier Transformations (Virtanen et al., 2020) along latitude circles; cf. supplemental material for more detailed wave decompositions



220



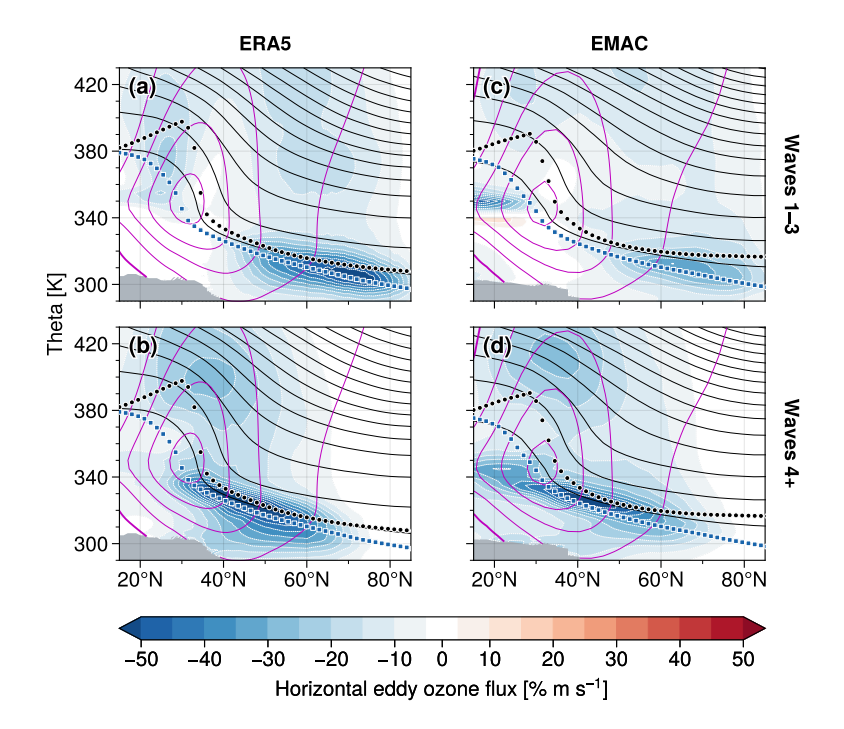


Figure 6. Horizontal eddy ozone flux (colors) associated with planetary-scale waves (top row, zonal wave numbers 1–3) and medium-to smaller-scale waves (bottom row, wave numbers 4+), as derived from ERA5 reanalyses (left column) and EMAC data (right column), respectively (winter-mean climatologies, DJF 2000–2019). Other details as in Fig. 1. A more detailed wave decomposition is provided in Fig. S3 in the supplemental material.

weaker contributions there due to planetary-scale waves (Fig. 7a,c). These downward fluxes are consistent with down-gradient ozone transport into lower altitudes. In addition, we find weak positive ozone fluxes at the high-latitude tropopause in ERA5, which are primarily due to planetary-scale waves. Furthermore, clear signatures of up-gradient ozone transport due to planetary-scale waves are evident near the STJ core for both ERA5 and EMAC. We also note small differences between ERA5 and EMAC in the lower stratosphere (above ~ 350 K). However, the overall contribution of vertical eddy ozone transport to the ozone budget turned out to be negligible in this region (recall Fig. 2).

The layered transport signatures due to vertical eddy ozone fluxes with alternating ozone tendency maxima and minima in the upper troposphere and tropopause region (cf. Fig. 2) suggest that different diabatic processes may dominate these eddy fluxes in different regions. We therefore decompose the vertical eddy ozone flux into contributions due to different diabatic processes. Figure 8 summarizes these results by showing the winter-mean vertical eddy ozone flux climatologies associated with total diabatic heating, full-sky radiation (long-wave and short-wave) and non-radiative effects (total diabatic heating rates minus full-sky contributions), respectively. It reveals that the complex structure of the total vertical eddy ozone flux arises due to a





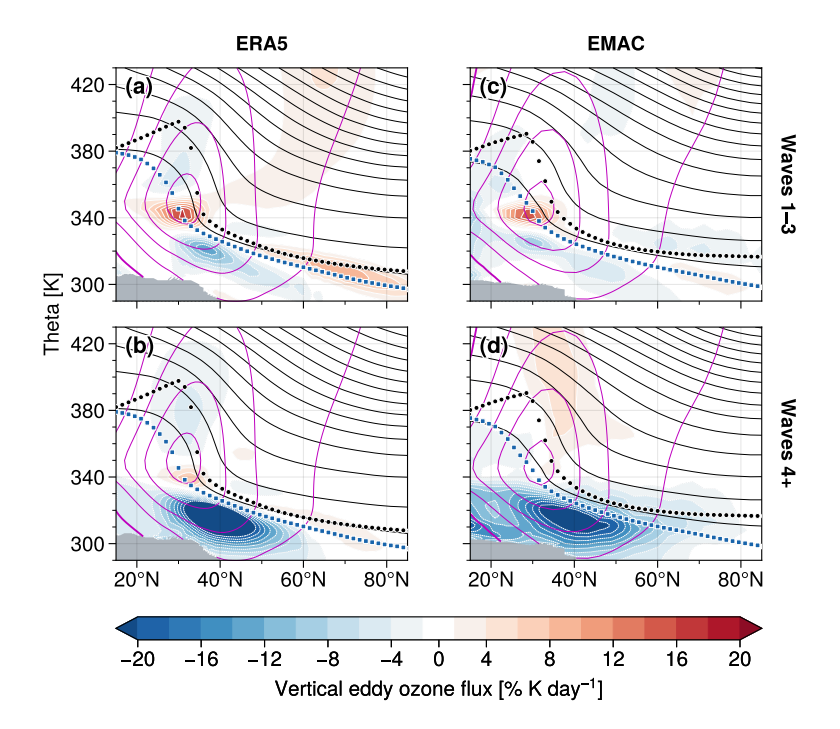


Figure 7. Same as in Fig. 6 but for the vertical eddy ozone flux. See Fig. S4 in the supplement for a more detailed wave decomposition.

superposition of simpler structures due to radiative and non-radiative processes. Radiation predominantly causes positive (upgradient) vertical eddy ozone fluxes, which tend to maximize along the extratropical tropopause (Fig. 8b,e). This is consistent for both ERA5 and EMAC, lending support to the robustness of this result. Closer inspection reveals that this is primarily due to clear-sky radiation associated with planetary-scale waves, i. e., due to processes that we expect to be well-represented in both data sets. Contributions by cloud radiative effects are small for both ERA5 and EMAC (not shown).

Other (non-radiative) diabatic processes cause predominantly negative (down-gradient) vertical eddy ozone fluxes, which tend to maximize in the upper troposphere (Fig. 8c,f). These include latent heating and vertical diffusion, with the former likely playing a stronger role in the upper troposphere and the latter near and above the tropopause.

Strikingly, the tropopause-level positive vertical eddy ozone fluxes due to radiation would by themselves act to sharpen the pre-existing strong ozone gradients in this region (by transporting ozone from where it is low, just below the tropopause, to where it is high, just above the tropopause). Since they are dominated by clear-sky radiation, we consider simple Newtonian radiative damping as a mechanism giving rise to these positive vertical eddy ozone fluxes as follows (e. g., Andrews et al., 1987):

$$Q_{cs}' \simeq -\alpha \theta' = \alpha p' \, \partial_p \overline{\theta} = -\alpha p' \left(g \overline{\rho_\theta} \right)^{-1} \,, \tag{2}$$





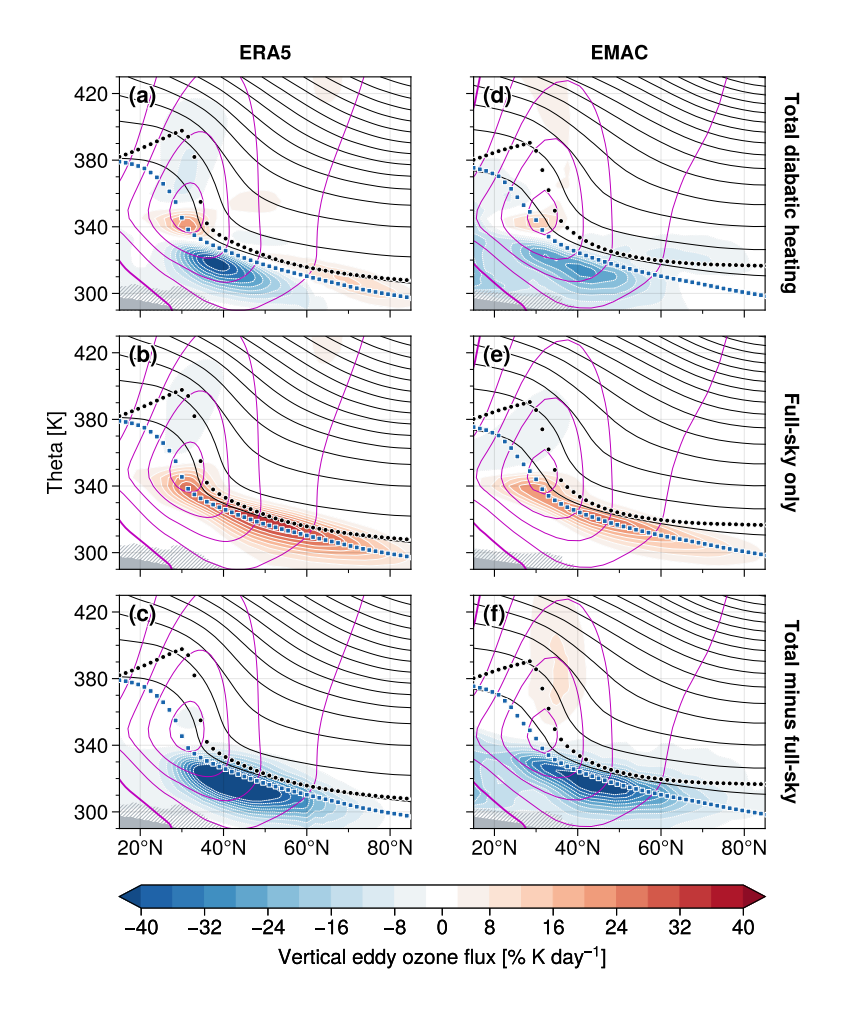


Figure 8. Contributions to the vertical eddy ozone flux associated with full-sky radiation and non-radiative effects, respectively, as obtained from (**a–c**) ERA5 and (**d–f**) EMAC. Other details as in Fig. 7.

where α is a radiative damping rate. This relation shows that upward displaced isentropes (p' < 0) result in clear-sky radiative heating, $Q'_{cs} > 0$, and downward displaced isentropes (p' > 0) result in clear-sky radiative cooling, $Q'_{cs} < 0$ (in each case acting against the vertical displacement). Figure 9 illustrates that within Rossby waves, these displacement anomalies are coupled to corresponding ozone anomalies that arise due to horizontal advection as part of the dynamics of the Rossby wave: negative ozone anomalies appear within high-pressure (anticyclonic) regions and positive anomalies appear within low-pressure (cyclonic) regions. That is, Q'_{cs} and ozone are positively correlated and the resulting covariance (the vertical eddy ozone flux in isentropic coordinates) is positive (up-gradient).



255



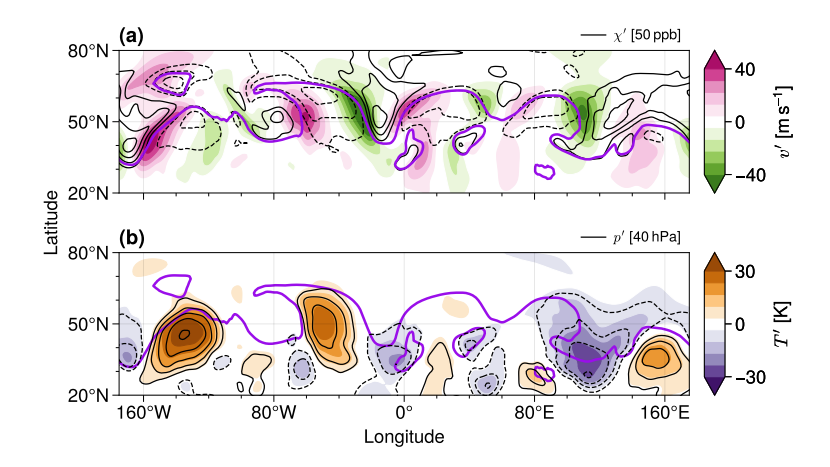


Figure 9. Example snapshots for November 28, 2008, to illustrate coupled horizontal and vertical ozone transport due to Rossby waves. (a) Zonal deviations of the meridional wind, $v' \equiv v - \overline{v}$ (color coding) and ozone (black contours with 50 ppb contour interval) at 315 K. (b) Same as in (a) but for temperature (colors) and pressure (contour interval is 40 hPa). The violet thick curve each shows the 2 PVU potential vorticity isoline. Solid (dashed) black contour lines indicate positive (negative) values, where zero contours have been omitted. The data fields have been smoothed by a 5° rolling average along longitude and latitude. ERA5 data at 315 K as obtained from EMCWF's ERA5 catalogue (Hersbach et al., 2017).

For a subsequent analysis with monthly-mean EMAC model output, we compared the clear-sky vertical eddy ozone fluxes with the relaxation approach according to Eq. (2),

$$\overline{\hat{Q}_{cs}\rho_{\theta}\hat{\chi}} \simeq -\alpha \overline{\hat{\theta}\rho_{\theta}\hat{\chi}} = -\alpha g^{-1} \overline{\hat{p}\hat{\chi}}^*, \tag{3}$$

providing evidence that long-wave radiative damping indeed can explain most parts of the up-gradient ozone flux signatures along the tropopause under clear-sky conditions with a typical relaxation rate $\alpha^{-1} \sim 1$ week (not shown). The weak positive ozone fluxes associated with cloud radiative effects at the tropopause (not shown) can likely be explained in a similar way by considering cloud-top long-wave cooling that is linked to Rossby wave dynamics in the mid-latitudes. We furthermore investigated a passive, linear Age of Air tracer in EMAC, where we found similar up-gradient vertical eddy fluxes along the tropopause (not shown), suggesting that short-wave ozone-radiation feedback rather plays a minor role in causing this feature.

Finally we note that for Boreal summer (June–August), the down-gradient vertical eddy ozone fluxes in the upper troposphere associated with non-radiative effects turned out to be substantially stronger than during winter (cf. Fig. S6 in the supplemental material). In contrast, the up-gradient vertical eddy fluxes under full-sky conditions in the tropopause region are much weaker, likely due to the reduced vertical gradients of ozone and potential temperature across the tropopause. The total contribution of vertical eddy transport to the UTLS ozone budget during summer is therefore mostly governed by down-gradient ozone transport (cf. fourth row in Fig. 4).



270

275

285

290



5 Summary and conclusions

In this paper, we studied different aspects of the zonal-mean ozone budget of the northern hemispheric lowermost stratosphere (LMS). Our comparison of winter-mean ozone transport climatologies based on 20 years of ERA5 reanalysis data and EMAC climate model output confirmed the expected important contributions by quasi-horizontal adiabatic eddy mixing and diabatic downward advection by the residual stratospheric circulation. These two contributions together well reproduce the total winter-mean ozone tendencies in the upper extratropical LMS. However, near the tropopause and the subtropical jet core the effects of horizontal mean flow advection and vertical eddy ozone transport become relevant. We noted differences in the actual magnitudes of the individual transport contributions and ozone background gradients between ERA5 and EMAC, which may be associated with the model's intrinsic resolution, parameterization schemes and approximations that govern each model's dynamical transport characteristics, as well as numerical diffusion that may have been partly corrected for by data assimilation only in the reanalyses.

Our analysis furthermore showed that meridional eddy ozone transport in the upper LMS (i. e., the shallow branch of the Brewer–Dobson circulation, BDC) is mainly governed by medium- to smaller-scale waves and is strong throughout the whole year due to continuous dynamical wave driving. This is in contrast with poleward ozone transport in the higher stratosphere (as part of the deep branch of the BDC) that is mostly driven by planetary-scale waves and shows strong seasonality with strongly reduced horizontal eddy transport during summer. It is worth noting that wave-driven meridional mean flow advection contributes significantly in the subtropical lower stratosphere (across the upper flank of the subtropical jet) and therefore seems to be clearly part of the shallow branch of the BDC.

The winter-mean climatology of the horizontal eddy ozone flux supports the concept of diffusive, down-gradient eddy transport in the UTLS, acting to reduce the underlying ozone background gradients. This is not the case, however, for vertical eddy ozone transport, especially near the tropopause, where the corresponding ozone flux climatologies clearly indicate upward (up-gradient) transport, which by itself would act to sharpen the pre-existing positive vertical ozone gradients at the tropopause. We found these upward eddy ozone fluxes to arise primarily due to radiative damping within planetary-scale Rossby waves. Since these Rossby waves are at the same time responsible for the down-gradient horizontal eddy fluxes, which are stronger in magnitude, these radiatively-damped vertical fluxes should be viewed as effectively reducing the horizontal fluxes.

Significant vertical eddy ozone fluxes are also found due to latent heating in the upper troposphere, and to a lesser degree due to vertical diffusion near the tropopause, leading to down-gradient vertical ozone transport. Cloud-radiative effects, which usually come along with substantial uncertainties in general circulation models, and ozone—radiation feedback turned out to be less important in the analyzed models. For northern hemispheric summer, we found much weaker signatures of up-gradient vertical ozone fluxes, which is probably in part due to the weaker vertical gradients of ozone across the tropopause during that time. Consequently, vertical eddy ozone transport during summer is dominated by down-gradient transport in the upper troposphere through synoptic- and small-scale waves. In general, these findings suggest that our picture of eddy ozone transport in the tropopause region should include both isentropic, quasi-horizontal eddy mixing as well as the coupled diabatic effects associated with Rossby wave dynamics that can contribute substantially to the local ozone budget.

https://doi.org/10.5194/egusphere-2025-2195 Preprint. Discussion started: 2 June 2025 © Author(s) 2025. CC BY 4.0 License.



305



Code and data availability. ERA5 reanalysis data on model levels can be downloaded at https://apps.ecmwf.int/data-catalogues/era5/?class= ea. EMAC model output and code for processing the data used in this study are available from the authors upon request. This paper contains modified Copernicus Climate Change Service information 2025. Neither the European Commission nor ECMWF is responsible for any use that may be made of the Copernicus information or data it contains.

Author contributions. FH conducted the analyses and prepared the first draft of the manuscript. He was supervised by HG and TB. FP provided pre-processed ERA5 reanalysis data on model levels and advice for the subsequent data processing. MM provided the EMAC model output. All authors helped to improve the manuscript.

300 Competing interests. The authors declare that they have no conflict of interest.

Acknowledgements. We thank P. Conrat Fuentes (LMU Munich) for his work on Python code for computing thermal tropopause heights, which was partially used within this study. We furthermore thank P. Jöckel (DLR) for his support in updating and implementing the EMAC model setup. We acknowledge the usage of the Python programming language and several extensions included therein, in particular, among others, the software packages xarray (Hoyer and Hamman, 2017) and PyTropD (Adam et al., 2018; Ming, 2022). The figures in this paper have been produced using Matplotlib (Hunter, 2007) and ProPlot (Davis, 2021). This work was funded by the Deutsche Forschungsgemeinschaft (DFG, German Research Foundation) – TRR 301 – Project-ID 428312742. We acknowledge the computing time on the JUWELS supercomputer at the Jülich Supercomputing Centre (JSC), which was granted under the VSR Project-ID "CLAMS-ESM", and technical support by the JSC staff. This work used resources of the Deutsches Klimarechenzentrum (DKRZ) granted by its Scientific Steering Committee (WLA) under Project-ID "bd1305".





- Abalos, M., Ploeger, F., Konopka, P., Randel, W. J., and Serrano, E.: Ozone seasonality above the tropical tropopause: reconciling the Eulerian and Lagrangian perspectives of transport processes, Atmos. Chem. Phys., 13, 10787–10794, https://doi.org/10.5194/acp-13-10787-2013, 2013
- Adam, O., Grise, K. M., Staten, P., Simpson, I. R., Davis, S. M., Davis, N. A., Waugh, D. W., Birner, T., and Ming, A.: The TropD software package (v1): standardized methods for calculating tropical-width diagnostics, Geosci. Model Dev., 11, 4339–4357, https://doi.org/10.5194/gmd-11-4339-2018, 2018.
 - Albers, J. R., Perlwitz, J., Butler, A. H., Birner, T., Kiladis, G. N., Lawrence, Z. D., Manney, G. L., Langford, A. O., and Dias, J.: Mechanisms governing interannual variability of stratosphere-to-troposphere ozone transport, J. Geophys. Res.-Atmos., 123, 234–260, https://doi.org/10.1002/2017JD026890, 2018.
- 320 Andrews, D. G., Holton, J. R., and Leovy, C. B.: Middle atmosphere dynamics, vol. 40 of *International Geophysics*, Academic Press, 1987.
 Baikhadzhaev, R., Ploeger, F., Preusse, P., Ern, M., and Birner, T.: A dynamical separation of deep and shallow branches in the stratospheric circulation, EGUsphere [preprint], https://doi.org/10.5194/egusphere-2024-4088, 2025.
 - Ball, W. T., Alsing, J., Staehelin, J., Davis, S. M., Froidevaux, L., and Peter, T.: Stratospheric ozone trends for 1985–2018: sensitivity to recent large variability, Atmos. Chem. Phys., 19, 12731–12748, https://doi.org/10.5194/acp-19-12731-2019, 2019.
- Ball, W. T., Chiodo, G., Abalos, M., Alsing, J., and Stenke, A.: Inconsistencies between chemistry-climate models and observed lower stratospheric ozone trends since 1998, Atmos. Chem. Phys., 20, 9737–9752, https://doi.org/10.5194/acp-20-9737-2020, 2020.
 - Birner, T. and Bönisch, H.: Residual circulation trajectories and transit times into the extratropical lowermost stratosphere, Atmos. Chem. Phys., 11, 817–827, https://doi.org/10.5194/acp-11-817-2011, 2011.
 - Butchart, N.: The Brewer-Dobson circulation, Rev. Geophys., 52, 157-184, https://doi.org/10.1002/2013RG000448, 2014.
- Cariolle, D. and Teyssèdre, H.: A revised linear ozone photochemistry parameterization for use in transport and general circulation models: multi-annual simulations, Atmos. Chem. Phys., 7, 2183–2196, https://doi.org/10.5194/acp-7-2183-2007, 2007.
 - Chapman, S.: A theory of upper-atmospheric ozone, Mem. R. Meteor. Soc., 3, 103-125, 1929.
 - Charney, J. G. and Drazin, P. G.: Propagation of planetary-scale disturbances from the lower into the upper atmosphere, J. Geophys. Res., 66, 83–109, https://doi.org/10.1029/JZ066i001p00083, 1961.
- 335 Davis, L. L. B.: ProPlot, https://doi.org/10.5281/zenodo.3873878, 2021.
 - Davis, N. and Birner, T.: On the Discrepancies in Tropical Belt Expansion between Reanalyses and Climate Models and among Tropical Belt Width Metrics, J. Climate, 30, 1211–1231, https://doi.org/10.1175/JCLI-D-16-0371.1, 2017.
 - Davis, N. A. and Birner, T.: Seasonal to multidecadal variability of the width of the tropical belt, J. Geophys. Res.-Atmos., 118, 7773–7787, https://doi.org/10.1002/jgrd.50610, 2013.
- Davis, S. M., Hegglin, M. I., Fujiwara, M., Dragani, R., Harada, Y., Kobayashi, C., Long, C., Manney, G. L., Nash, E. R., Potter, G. L., Tegtmeier, S., Wang, T., Wargan, K., and Wright, J. S.: Assessment of upper tropospheric and stratospheric water vapor and ozone in reanalyses as part of S-RIP, Atmos. Chem. Phys., 17, 12743–12778, https://doi.org/10.5194/acp-17-12743-2017, 2017.
 - Davis, S. M., Hegglin, M. I., Dragani, R., Fujiwara, M., Harada, Y., Kobayashi, C., Long, C., Manney, G. L., Nash, E. R., Potter, G. L., Tegtmeier, S., Wang, T., Wargan, K., and Wright, J. S.: Overview of ozone and water vapour, in: SPARC Reanalysis Intercomparison
- Project (S-RIP) Final Report, edited by Fujiwara, M., Manney, G. L., Gray, L. J., and Wright, J. S., pp. 123–164, SPARC Report No. 10, WCRP-17/2020, https://doi.org/10.17874/800dee57d13, 2022.

https://doi.org/10.5194/egusphere-2025-2195 Preprint. Discussion started: 2 June 2025 © Author(s) 2025. CC BY 4.0 License.



380



- Dietmüller, S., Jöckel, P., Tost, H., Kunze, M., Gellhorn, C., Brinkop, S., Frömming, C., Ponater, M., Steil, B., Lauer, A., and Hendricks, J.: A new radiation infrastructure for the Modular Earth Submodel System (MESSy, based on version 2.51), Geosci. Model Dev., 9, 2209–2222, https://doi.org/10.5194/gmd-9-2209-2016, 2016.
- Dietmüller, S., Garny, H., Eichinger, R., and Ball, W. T.: Analysis of recent lower-stratospheric ozone trends in chemistry climate models, Atmos. Chem. Phys., 21, 6811–6837, https://doi.org/10.5194/acp-21-6811-2021, 2021.
 - ECMWF: Part IV: physical processes, in: IFS documentation Cy41r2, ECMWF, https://doi.org/10.21957/tr5rv27xu, 2016.
 - ECMWF: Parameter Database, https://codes.ecmwf.int/grib/param-db/235005/ (last access: 10 February 2025), 2025.
- Gettelman, A., Hoor, P., Pan, L. L., Randel, W. J., Hegglin, M. I., and Birner, T.: The extratropical upper troposphere and lower stratosphere, Rev. Geophys., 49, https://doi.org/10.1029/2011RG000355, 2011.
 - Hersbach, H., Bell, B., Berrisford, P., Hirahara, S., Horányi, A., Muñoz-Sabater, J., Nicolas, J., Peubey, C., Radu, R., Schepers, D., Simmons, A., Soci, C., Abdalla, S., Abellan, X., Balsamo, G., Bechtold, P., Biavati, G., Bidlot, J., Bonavita, M., De Chiara, G., Dahlgren, P., Dee, D., Diamantakis, M., Dragani, R., Flemming, J., Forbes, R., Fuentes, M., Geer, A., Haimberger, L., Healy, S., Hogan, R. J., Hólm, E., Janisková, M., Keeley, S., Laloyaux, P., Lopez, P., Lupu, C., Radnoti, G., de Rosnay, P., Rozum, I., Vamborg, F., Villaume, S., and Thépaut, J.-N.: Complete ERA5 global atmospheric reanalysis, Copernicus Climate Change Service (C3S) Data Store (CDS),
- S., and Thépaut, J.-N.: Complete ERA5 global atmospheric reanalysis, Copernicus Climate Change Service (C3S) Data Store (CDS), https://doi.org/10.24381/cds.143582cf, 2017.
 - Hersbach, H., Bell, B., Berrisford, P., Hirahara, S., Horányi, A., Muñoz-Sabater, J., Nicolas, J., Peubey, C., Radu, R., Schepers, D., Simmons, A., Soci, C., Abdalla, S., Abellan, X., Balsamo, G., Bechtold, P., Biavati, G., Bidlot, J., Bonavita, M., De Chiara, G., Dahlgren, P., Dee, D., Diamantakis, M., Dragani, R., Flemming, J., Forbes, R., Fuentes, M., Geer, A., Haimberger, L., Healy, S., Hogan, R. J., Hólm, E., Janisková, M., Keeley, S., Laloyaux, P., Lopez, P., Lupu, C., Radnoti, G., de Rosnay, P., Rozum, I., Vamborg, F., Villaume, S., and Thépaut,
- Janisková, M., Keeley, S., Laloyaux, P., Lopez, P., Lupu, C., Radnoti, G., de Rosnay, P., Rozum, I., Vamborg, F., Villaume, S., and Thépaut J.-N.: The ERA5 global reanalysis, Q. J. Roy. Meteor. Soc., 146, 1999–2049, https://doi.org/10.1002/qj.3803, 2020.
 - Holton, J. R., Haynes, P. H., McIntyre, M. E., Douglass, A. R., Rood, R. B., and Pfister, L.: Stratosphere-troposphere exchange, Rev. Geophys., 33, 403–439, https://doi.org/10.1029/95RG02097, 1995.
 - Hoyer, S. and Hamman, J.: xarray: N-D labeled arrays and datasets in Python, J. Open Res. Softw., 5, https://doi.org/10.5334/jors.148, 2017.
- 370 Hunter, J. D.: Matplotlib: a 2D graphics environment, Comput. Sci. Eng., 9, 90–95, https://doi.org/10.1109/MCSE.2007.55, 2007.
 - Jöckel, P., Kerkweg, A., Pozzer, A., Sander, R., Tost, H., Riede, H., Baumgaertner, A., Gromov, S., and Kern, B.: Development cycle 2 of the Modular Earth Submodel System (MESSy2), Geosci. Model Dev., 3, 717–752, https://doi.org/10.5194/gmd-3-717-2010, 2010.
 - Jöckel, P., Tost, H., Pozzer, A., Kunze, M., Kirner, O., Brenninkmeijer, C. A. M., Brinkop, S., Cai, D. S., Dyroff, C., Eckstein, J., Frank, F., Garny, H., Gottschaldt, K.-D., Graf, P., Grewe, V., Kerkweg, A., Kern, B., Matthes, S., Mertens, M., Meul, S., Neumaier, M., Nützel, M.,
- Oberländer-Hayn, S., Ruhnke, R., Runde, T., Sander, R., Scharffe, D., , and Zahn, A.: Earth System Chemistry integrated Modelling (ES-CiMo) with the Modular Earth Submodel System (MESSy) version 2.51, Geosci. Model Dev., 9, 1153–1200, https://doi.org/10.5194/gmd-9-1153-2016, 2016.
 - Jöckel, P., Brinkop, S., Graf, P., Eichinger, R., Garny, H., Mertens, M., Nützel, M., Pozzer, A., Tost, H., and the MESSy Consortium: RD1: EMAC CCMI-2022 free running hindcast simulation 1950-2019, World Data Center for Climate (WDCC) at DKRZ, https://doi.org/10.26050/WDCC/ESCiMo2_RD1, 2024.
 - Konopka, P., Grooß, J.-U., Günther, G., Ploeger, F., Pommrich, R., Müller, R., and Livesey, N.: Annual cycle of ozone at and above the tropical tropopause: observations versus simulations with the Chemical Lagrangian Model of the Stratosphere (CLaMS), Atmos. Chem. Phys., 10, 121–132, https://doi.org/10.5194/acp-10-121-2010, 2010.



390

395

400

410

415



- Meinshausen, M., Vogel, E., Nauels, A., Lorbacher, K., Meinshausen, N., Etheridge, D. M., Fraser, P. J., Montzka, S. A., Rayner, P. J.,
 Trudinger, C. M., Krummel, P. B., Beyerle, U., Canadell, J. G., Daniel, J. S., Enting, I. G., Law, R. M., Lunder, C. R., O'Doherty, S.,
 Prinn, R. G., Reimann, S., Rubino, M., Velders, G. J. M., Vollmer, M. K., Wang, R. H. J., and Weiss, R.: Historical greenhouse gas concentrations for climate modelling (CMIP6), Geosci. Model Dev., 10, 2057–2116, https://doi.org/10.5194/gmd-10-2057-2017, 2017.
 - Meinshausen, M., Nicholls, Z. R. J., Lewis, J., Gidden, M. J., Vogel, E., Freund, M., Beyerle, U., Gessner, C., Nauels, A., Bauer, N., Canadell, J. G., Daniel, J. S., John, A., Krummel, P. B., Luderer, G., Meinshausen, N., Montzka, S. A., Rayner, P. J., Reimann, S., Smith, S. J., van den Berg, M., Velders, G. J. M., Vollmer, M. K., and Wang, R. H. J.: The shared socio-economic pathway (SSP) greenhouse gas

concentrations and their extensions to 2500, Geosci. Model Dev., 13, 3571-3605, https://doi.org/10.5194/gmd-13-3571-2020, 2020.

- Ming, A.: PyTropD version 2.12, GitHub, accessed 4 March 2025, https://github.com/TropD/pytropd, 2022.
- Ploeger, F., Diallo, M., Charlesworth, E., Konopka, P., Legras, B., Laube, J. C., Grooß, J.-U., Günther, G., Engel, A., and Riese, M.: The stratospheric Brewer–Dobson circulation inferred from age of air in the ERA5 reanalysis, Atmos. Chem. Phys., 21, 8393–8412, https://doi.org/10.5194/acp-21-8393-2021, 2021.
- Plumb, R. A.: Stratospheric transport, J. Meteorol. Soc. Jpn. Ser. II, 80, 793-809, https://doi.org/10.2151/jmsj.80.793, 2002.
- Plummer, D., Nagashima, T., Tilmes, S., Archibald, A., Chiodo, G., Fadnavis, S., Garny, H., Josse, B., Kim, J., Lamarque, J.-F., Morgenstern, O., Murray, L., Orbe, C., Tai, A., Chipperfield, M., Funke, B., Juckes, M., Kinnison, D., Kunze, M., Luo, B., Matthes, K., Newman, P. A., Pascoe, C., and Peter, T.: CCMI-2022: a new set of Chemistry-Climate Model Initiative (CCMI) community simulations to update the assessment of models and support upcoming ozone assessment activities, in: SPARC Newsletter No. 57, July 2021, pp. 22–30, available at https://www.aparc-climate.org/publications/newsletter/, 2021.
- Pringle, K. J., Tost, H., Message, S., Steil, B., Giannadaki, D., Nenes, A., Fountoukis, C., Stier, P., Vignati, E., and Lelieveld, J.: Description and evaluation of GMXe: a new aerosol submodel for global simulations (v1), Geosci. Model Dev., 3, 391–412, https://doi.org/10.5194/gmd-3-391-2010, 2010.
- 405 Roeckner, E., Bäuml, G., Bonaventura, L., Brokopf, R., Esch, M., Giorgetta, M., Hagemann, S., Kirchner, I., Kornblueh, L., Manzini, E., Rhodin, A., Schlese, U., Schulzweida, U., and Tompkins, A.: The atmospheric general circulation model ECHAM5. Part I: Model description, https://doi.org/10.17617/2.995269, Max Planck Institute for Meteorology, Report No. 349, 2003.
 - Roeckner, E., Brokopf, R., Esch, M., Giorgetta, M., Hagemann, S., Kornblueh, L., Manzini, E., Schlese, U., and Schulzweida, U.: Sensitivity of simulated climate to horizontal and vertical resolution in the ECHAM5 atmosphere model, J. Climate, 19, 3771–3791, https://doi.org/10.1175/JCLI3824.1, 2006.
 - Sander, R., Jöckel, P., Kirner, O., Kunert, A. T., Landgraf, J., and Pozzer, A.: The photolysis module JVAL-14, compatible with the MESSy standard, and the JVal PreProcessor (JVPP), Geosci. Model Dev., 7, 2653–2662, https://doi.org/10.5194/gmd-7-2653-2014, 2014.
 - Sander, R., Baumgaertner, A., Cabrera-Perez, D., Frank, F., Gromov, S., Grooß, J.-U., Harder, H., Huijnen, V., Jöckel, P., Karydis, V. A., Niemeyer, K. E., Pozzer, A., Riede, H., Schultz, M. G., Taraborrelli, D., and Tauer, S.: The community atmospheric chemistry box model CAABA/MECCA-4.0, Geosci. Model Dev., 12, 1365–1385, https://doi.org/10.5194/gmd-12-1365-2019, 2019.
 - Simmons, A., Soci, C., Nicolas, J., Bell, B., Berrisford, P., Dragani, R., Flemming, J., Haimberger, L., Healy, S., Hersbach, H., Horányi, A., Inness, A., Muñoz-Sabater, J., Radu, R., and Schepers, D.: Global stratospheric temperature bias and other stratospheric aspects of ERA5 and ERA5.1, vol. 859 of *ECMWF Technical Memoranda*, https://doi.org/10.21957/rcxqfmg0, 2020.
- Virtanen, P., Gommers, R., Oliphant, T. E., Haberland, M., Reddy, T., Cournapeau, D., Burovski, E., Peterson, P., Weckesser, W., Bright,

 J., van der Walt, S. J., Brett, M., Wilson, J., Millman, K. J., Mayorov, N., Nelson, A. R. J., Jones, E., Kern, R., Larson, E., Carey, C. J.,

 Polat, İ., Feng, Y., Moore, E. W., VanderPlas, J., Laxalde, D., Perktold, J., Cimrman, R., Henriksen, I., Quintero, E. A., Harris, C. R.,

https://doi.org/10.5194/egusphere-2025-2195 Preprint. Discussion started: 2 June 2025 © Author(s) 2025. CC BY 4.0 License.





- Archibald, A. M., Ribeiro, A. H., Pedregosa, F., van Mulbregt, P., and SciPy 1.0 Contributors: SciPy 1.0: fundamental algorithms for scientific computing in Python, Nat. Methods, 17, 261–272, https://doi.org/10.1038/s41592-019-0686-2, 2020.
- Waters, J. W., Froidevaux, L., Harwood, R. S., Jarnot, R. F., Pickett, H. M., Read, W. G., Siegel, P. H., Cofield, R. E., Filipiak, M. J., Flower,
 D. A., Holden, J. R., Lau, G. K., Livesey, N. J., Manney, G. L., Pumphrey, H. C., Santee, M. L., Wu, D. L., Cuddy, D. T., Lay, R. R.,
 Loo, M. S., Perun, V. S., Schwartz, M. J., Stek, P. C., Thurstans, R. P., Boyles, M. A., Chandra, K. M., Chavez, M. C., Chen, G.-S.,
 Chudasama, B. V., Dodge, R., Fuller, R. A., Girard, M. A., Jiang, J. H., Jiang, Y., Knosp, B. W., LaBelle, R. C., Lam, J. C., Lee, K. A.,
 Miller, D., Oswald, J. E., Patel, N. C., Pukala, D. M., Quintero, O., Scaff, D. M., Van Snyder, W., Tope, M. C., Wagner, P. A., and Walch,
 M. J.: The Earth observing system microwave limb sounder (EOS MLS) on the aura satellite, IEEE T. Geosci. Remote, 44, 1075–1092,
 https://doi.org/10.1109/TGRS.2006.873771, 2006.
 - WMO: Meteorology a three-dimensional science. Second session of the Commission for Aerology, WMO Bulletin, 6, 134–138, available online at https://library.wmo.int/idurl/4/42003, 1957.
 - WMO: Scientific assessment of ozone depletion: 2022. GAW Report No. 278, Geneva, Switzerland, 2022.
- Yang, H., Chen, G., Tang, Q., and Hess, P.: Quantifying isentropic stratosphere-troposphere exchange of ozone, J. Geophys. Res.-Atmos., 121, 3372–3387, https://doi.org/10.1002/2015JD024180, 2016.

Chapter 5

Discussion

Paper I

Key question:

Which are the dominant dynamical drivers of ozone variability in the extratropical stratosphere during winter and how do they affect LMS ozone?

The paper presented in Chapter 2 in this thesis considered the fundamental connections between year-to-year variability of stratospheric ozone in the middle to high latitudes and winter-mean fluctuations of the strength of the stratospheric polar vortex. From this perspective, the analyses focused on the intrinsic, i.e., mostly natural, variations of the atmospheric system and on the substantial ozone co-variability associated with large-scale transport anomalies. The usage of a temperature-based index time series provided a welldefined indicator of polar vortex strength, which featured outstanding robustness across the datasets used and can easily be derived from available observational data. Studying the winter-mean co-variability with the polar vortex is essential for understanding the general role of stratospheric ozone in our present climate, since the anomalies of polar vortex strength are known to be part of the dominant mode of atmospheric variability during northern hemispheric winter (e.g., Thompson and Wallace, 2000; Thompson et al., 2003). The paper emphasized the clear similarities between the resulting pattern of ozone co-variability associated with polar vortex strength and the structure of general wintermean ozone variability in the latitude-height plane, providing strong evidence that the dominant mode of atmospheric variability is also clearly reflected by year-by-year ozone variability. This was confirmed by the variance of polar stratospheric partial-column ozone that indeed was shown to be mostly explained by co-variability with the polar vortex.

Overall, the characteristic pattern of polar vortex—ozone co-variability in the latitude—height plane emerged from both reanalysis data as well as ozone satellite measurements and turned out to illustrate the ozone transport mechanisms involved in a quite intuitive manner. The lowermost stratosphere (LMS) was shown to be influenced by different, in parts counteracting, transport mechanisms, including quasi-horizontal eddy mixing in the mid- and high-latitudes, diabatic mean flow advection through the residual circulation in higher altitudes as well as strongly coupled, adiabatic tropopause variability. This complexity of ozone transport in the LMS suggested deeper insights by a more thorough analysis of the local ozone budget, as done in paper III in Chapter 4. It is worth noting, however, that first-order conclusions on the transport mechanisms involved could be drawn not only from a conventional ozone budget analysis, but also from a by-eye comparison of polar vortex—ozone co-variability in pressure and potential temperature coordinates.

The patterns of polar vortex—ozone co-variability explored in Chapter 2 have been derived by pointwise least-squares linear regressions across the latitude—height plane based on interannual anomaly time series diagnosing lower-stratospheric temperature variability. Evaluating these linear regression maps therefore neither requires high computational efforts nor extensive post-processing of reanalysis or model output typically provided by the forecast centers or climate modeling groups, respectively. The regression maps may therefore also be applied for assessing different reanalysis products or general circulation models, providing a tool for quick first-order estimates on ozone transport and circulation characteristics featured by the individual models. First steps towards this potential application were presented in the studies by Desille (2022, internship report) and Von Heydebrand (2022, Bachelor thesis), which directly emerged from the research for this thesis and have been co-advised by the author. In the following, the concept is briefly illustrated using climate model data from the Chemistry—Climate Model Initiative (CCMI; Eyring et al., 2013; Plummer et al., 2021)¹.

The regression maps in Fig. 5.1 visualize polar vortex—ozone co-variability during northern hemispheric winter (December-January-February) similar as in Chapter 2, but now based on ensemble-mean 1979–2009 data from the latest generation of the CCMI experiments (CCMI-2022). This figure allows to compare the zonal-mean patterns of ozone variability for two different climate runs REF-D1 and REF-D2 in the left and right panels for each individual model, respectively. For both model runs, the setup of greenhouse gas forcings

¹ Post-processed CCMI data produced and kindly provided by Dr. Sean Davis (NOAA). Labeling of the CCMI models considered in this chapter mostly follows Morgenstern et al. (2017) and CCMI (2025).

² Computation of tropopause heights throughout this chapter is based on the PyTropD package (Adam et al., 2018; Ming, 2022) and Python code by P. Conrat Fuentes (LMU Munich).

and ozone-depleting substances in the historical time period considered here is based on observational records and therefore is mostly equivalent (cf. Plummer et al., 2021). However, sea-surface temperatures (SSTs) and sea-ice concentrations (SICs) are prescribed in REF-D1 but not in REF-D2 (ibid.). In principal, the main features of the characteristic pattern of polar vortex—ozone co-variability discussed in paper I are quite well reproduced by most of the models presented in Fig. 5.1 and for both REF-D1 as well as REF-D2.

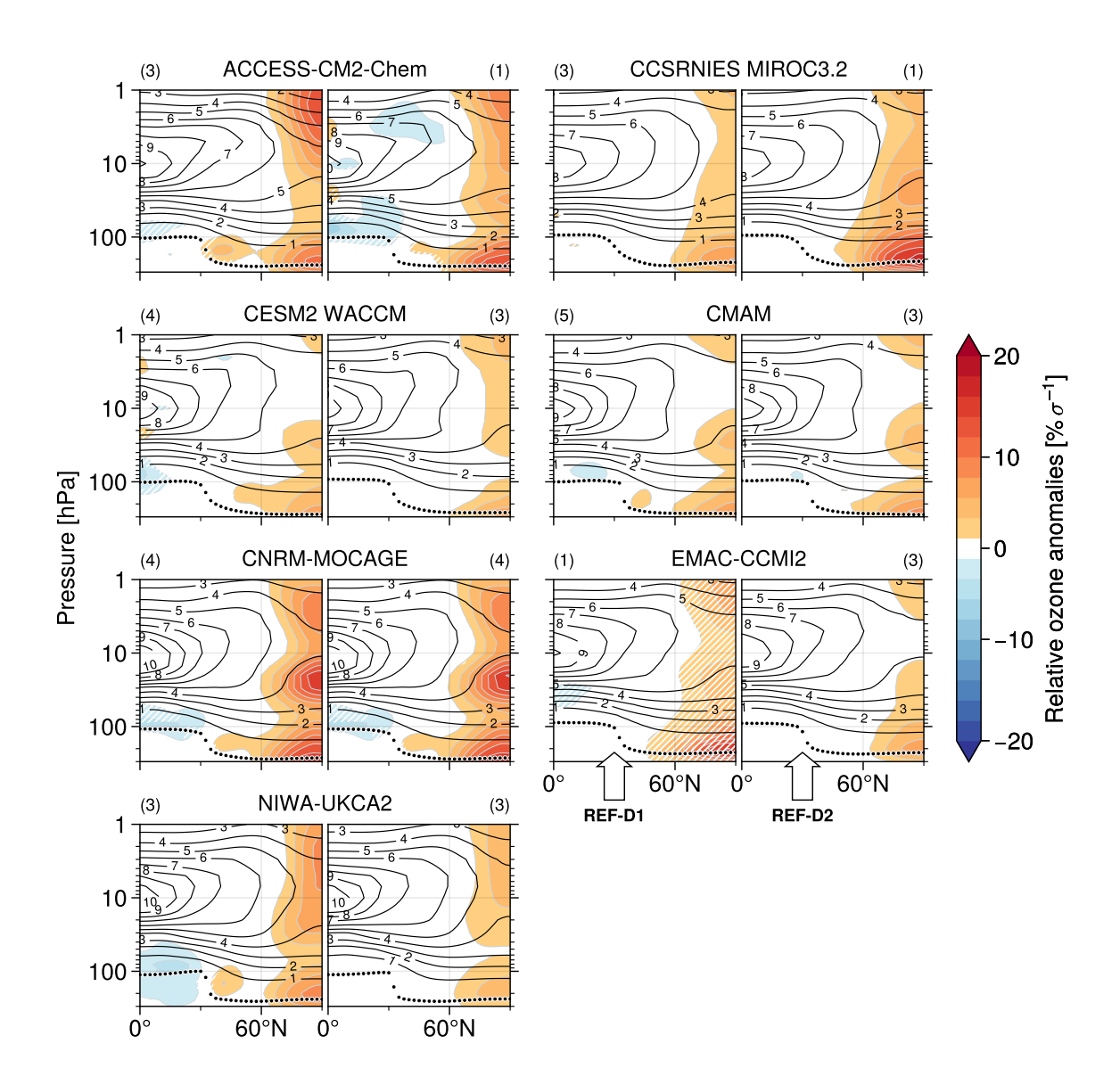


Figure 5.1: Interannual zonal-mean ozone anomalies regressed on polar-cap-averaged temperature at 100 hPa ("T100 index", as in Fig. 4 of Chapter 2) for winter-mean (DJF) 1979–2009 model output from the CCMI-2022 REF-D1 (left panels) and REF-D2 runs (right panels). Ozone co-variability (color coding) is provided relative to the corresponding climatology (shown by black contour lines in units of ppmv). The thick dotted lines show winter-mean WMO (1957) tropopause profiles². The number of ensemble members used to compute ensemble-mean data is given in parenthesis for each regression map.

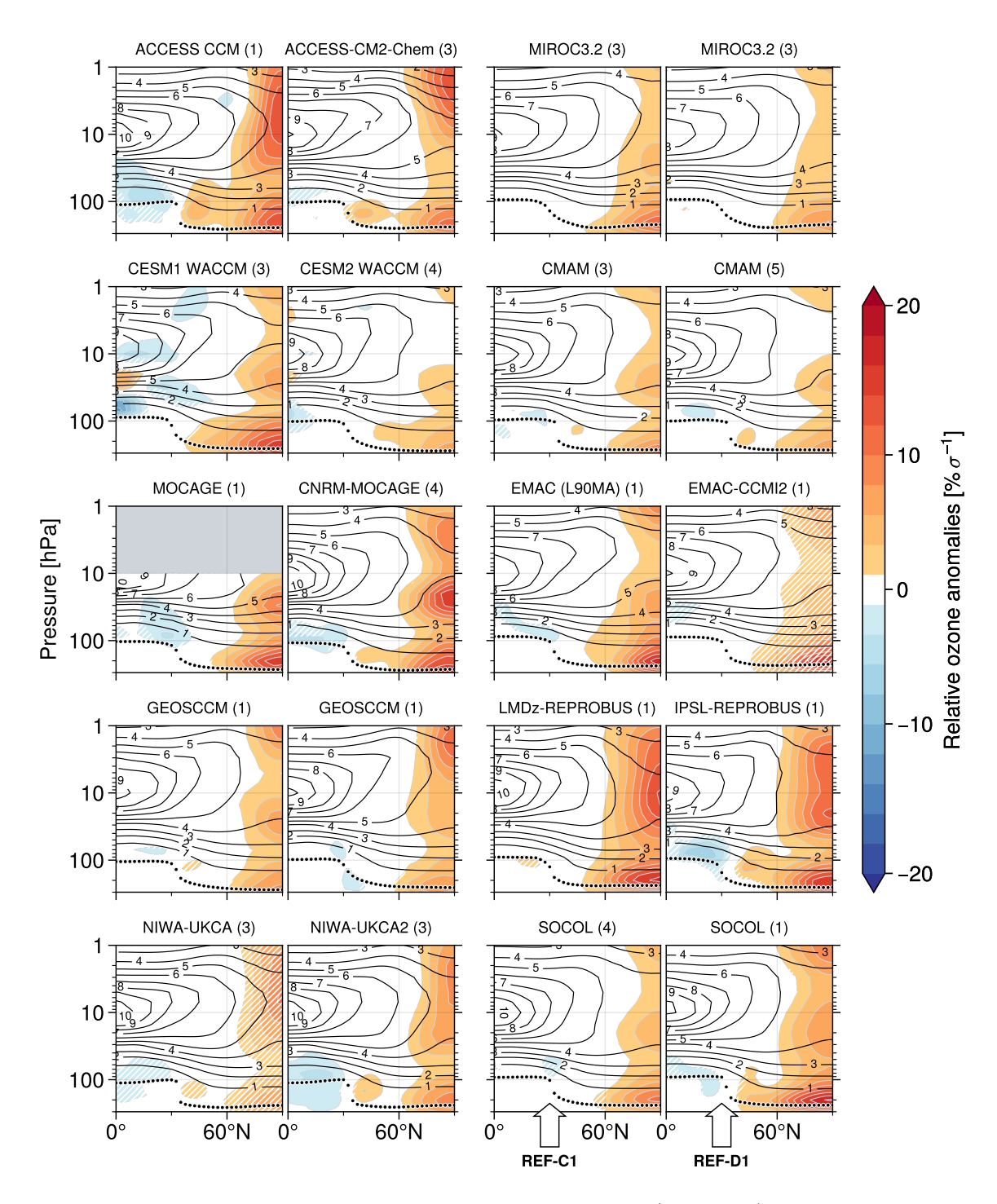


Figure 5.2: Same as Fig. 5.1 but now for CCMI-1 REF-C1 (left panels) and CCMI-2022 REF-D1 (right panels). REF-D1 data was missing for GEOSCCM for January 2008.

It is interesting to note, however, that some models show remarkably weak co-variability (e.g., CESM2 WACCM and CMAM) compared to others that feature quite strongly pronounced patterns of variability (e.g., ACCESS-CM2-Chem and CNRM-MOCAGE). The differences in handling the SSTs and SICs between the REF-D1 and REF-D2 runs may induce additional changes in stratospheric transport and ozone variability, which then

result in different patterns of ozone co-variability: comparing the results for REF-D1 and REF-D2 for the individual models in Fig. 5.1, differences are evident in the magnitude of co-variability in the polar upper stratosphere (e. g., ACCESS-CM2-Chem, EMAC-CCMI2 and NIWA-UKCA2), at the polar tropopause (e. g., CCSRNIES MIROC3.2 and EMAC-CCMI2) and in the LMS in the mid-latitudes (e. g., ACCESS-CM2-Chem, CESM2 WACCM and NIWA-UKCA2). Following the findings reported in paper I, this suggests variations of wave-driven polar vortex dynamics, the stratospheric residual circulation and quasi-adiabatic eddy mixing in the lower stratosphere, which then modulated both transport-related ozone co-variability as well as the climatological ozone distribution.

The regression maps of ozone co-variability associated with changes of the polar vortex can also be used to compare different generations of chemistry-climate models. This is shown in Fig. 5.2, comparing the historical runs REF-C1 and REF-D1 of CCMI phase 1 (CCMI-1) and the subsequent phase 2 (CCMI-2022), respectively, for Boreal winter during 1979–2009. Both runs use prescribed historical SSTs and SICs as well as an observation-based forcing setup, which were extended for CCMI-2022 (cf. Eyring et al., 2013; Plummer et al., 2021). Similar as before, Fig. 5.2 shows differences in the local strength of ozone co-variability between REF-C1 and REF-D1, which, among the updates of the underlying scenarios, may hint at structural changes across model generations in the setup of some of the CCMI models involved, which influenced the model's dynamical characteristics and, as a consequence, ozone transport and interannual variability.

Paper II

Key question:

How can we exploit the structural features of the LMS ozone distribution to track circulation variability?

Chapter 3 presented a detailed evaluation on whether and how properties of the subtropical zonal-mean ozone gradients can serve as useful diagnostics for jet stream variability in the subtropics in both hemispheres. This study focused on the equatorward flank of the extratropical LMS, which is marked by the thermal tropopause break, continuously strong zonal wind speeds in the jet stream region and a substantial increase of ozone concentrations in the LMS above the tropopause compared to the tropical upper troposphere. Here, subtropical jet stream variability is typically measured by variations of the underlying zonal wind field. However, since wind speed measurements are rather sparse in that region, this approach is often applied to globally resolved reanalysis data or general

circulation model output only, which then usually comes along with significant uncertainties due to the models' intrinsic limitations. The validation by observational data has turned out to be crucial for robust findings on jet stream variability and historical trends, which therefore motivates to also follow a more indirect procedure and extract additional information from observation-based ozone co-variability. This assumes that the coupling between the subtropical jet streams and the local ozone gradients is mediated mostly dynamically, in particular by meridional ozone transport through wave-induced, quasi-horizontal mixing of air masses in the LMS. This is illustrated as an outlook beyond paper III further below in this chapter. Paper II in Chapter 3 discussed various ozone metrics intended to allow a broad application with different datasets, including total-column ozone, and provided evidence that historical jet stream trends indeed can be constrained by ozone measurements already at this point in time. The uncertainties of this approach likely can be further reduced in the future when extended ozone records may become available. The different ozone metrics were shown to yield consistent results and correlate well with the strength and latitudinal location of the subtropical jet stream in both hemispheres, respectively, i. e., they align with the two leading modes of variability (e.g., Lorenz and Hartmann, 2001, 2003). Here, the information on circulation variability were extracted from the unique and well-pronounced gradients of LMS ozone in the subtropics, while the strong vertical gradients along the tropopause at higher latitudes have not been investigated in this paper. However, combining the results from paper I on the significant co-variability of the polar tropopause with the polar vortex, the associated ozone gradient changes there may allow to construct other suitable observation-based circulation metrics, e.g., of the stratospheric residual circulation (cf. Birner, 2024).

Paper III

Key question:

What are the relevant transport contributions to the LMS ozone budget?

The paper included in Chapter 4 aims to provide a classification of ozone transport in the northern hemispheric, extratropical LMS, in particular by investigating the qualitative structures of the individual transport contributions as well as their quantitative significance as a function of time during the year (with a focus on Boreal winter), altitude, latitudinal location and eddy zonal wavenumber where appropriate. The analysis exploits the features of both modern ERA5 reanalysis data as well as a state-of-the-art EMAC climate simulation to also estimate the robustness of small-scale structures of ozone transport especially in the upper troposphere and lower stratosphere. This approach helped

to reveal the importance of vertical (diabatic) eddy ozone transport associated with longwave radiative damping in the tropopause region, which turned out to strongly impact the dominant equatorward (adiabatic) eddy mixing in the LMS. This adds a new point to the current understanding of lower-stratospheric transport, since here diabatic, i.e. secondary, eddy effects have been shown to become relevant in the tropopause region and should not be neglected against the first-order, adiabatic wave driving, as usually done as reasonable approximation in the middle to higher stratosphere. With that, this study also illustrates that LMS ozone is influenced not only by mid-latitude wave activity and large-scale stratospheric transport, but also by radiative effects and smaller-scale tropospheric dynamics at lower altitudes. The sensitivity to each model's individual setup and parameterizations, among others, may also help explain differences in the climatological distribution of stratospheric ozone and in the magnitudes of the ozone gradients along the tropopause between reanalysis and simulation data found in Chapter 4. Ultimately, this raises the question about the causal relationship between ozone transport and the background ozone distribution, which, assuming ozone to represent a passive tracer in the LMS, in equilibrium both to some extent should reflect the characteristic features of the dynamical system under consideration – either for the real or a modeled atmosphere.

In the following, the question on the intrinsic connection between ozone transport and the ozone background gradients will be qualitatively addressed, focusing on the example of horizontal eddy mixing across the core of the subtropical jet stream in the Northern Hemisphere. For that, data from the ERA5 reanalyses and the EMAC simulation for the time range 2000–2019 are used as described in Chapter 4. Furthermore, the instantaneous horizontal ozone gradients at the tropopause near the subtropical jet are averaged within 30°N to 40°N and $340\,\text{K}$ to $380\,\text{K}$ to obtain an index time series of subtropical ozone gradient variability. Figure 5.3 then shows the linear regression maps of the interannual, winter-mean fields (December-January-February) of the zonal-mean zonal wind, modified potential vorticity (Lait, 1994) and diabatic heating regressed on this ozone gradient index for the northern hemispheric upper troposphere and lower stratosphere. The results for both ERA5 and EMAC provide evidence that seasonal fluctuations of the ozone gradient magnitudes are associated with an Annular-Mode-like pattern of atmospheric variability, which typically features the strengthening of the subtropical jet stream, equatorward shifting of the mid-latitude jet stream in the troposphere and deceleration of the stratospheric polar vortex (cf. panels 5.3a and d; e.g., Harzer, 2021). This is consistent with the response of potential vorticity in the lowermost to middle stratosphere (panels 5.3b and e) suggesting substantial anomalous wave dissipation, albeit here some differences occurred between ERA5 and EMAC. For subsequent research, it may be worth to have a closer look, e.g., at each model's wave propagation characteristics to understand these differ-

ences together with the reduced tropospheric wind response in EMAC (cf. panel 5.3d). The anomalous diabatic heating in the tropical lower stratosphere and increased diabatic cooling in the polar stratosphere in panels 5.3(c) and (f) likely are associated with the wave-induced strengthening of the residual Brewer–Dobson circulation. The tropospheric response of the diabatic heating is again less clear between ERA5 and EMAC, but likely is also caused by circulation changes due to anomalous wave forcing in lower altitudes.

Figure 5.3 overall showed the connection between subtropical ozone gradient anomalies and large-scale dynamical variability, where the latter suggests substantial changes of ozone transport in the subtropics. In particular, increased subtropical ozone gradients are associated with a stronger subtropical jet stream according to panels 5.3(a) and (d), which should lead to reduced horizontal eddy mixing across the jet acting as transport barrier as discussed in Chapter 3. The details on the causal relationship between these anomalies of subtropical ozone gradients and eddy transport can be extracted from linear

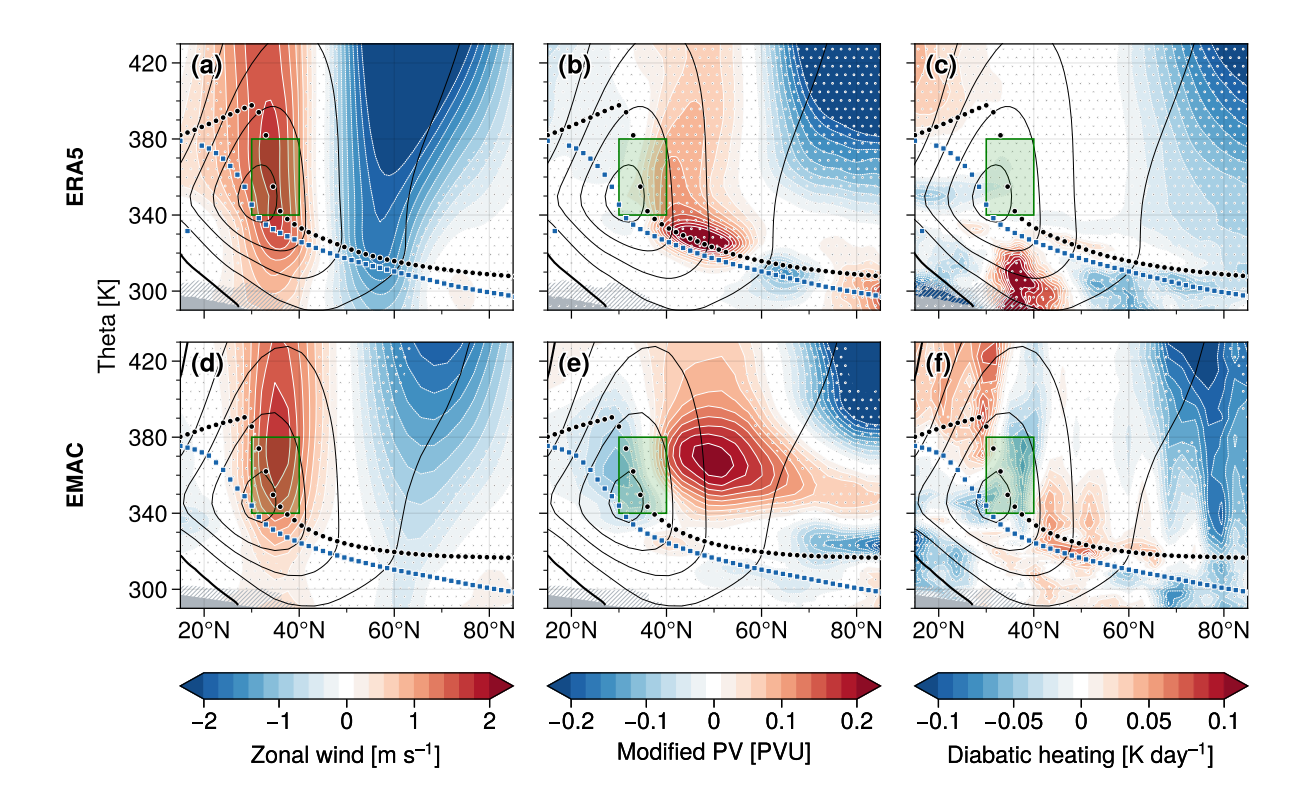


Figure 5.3: Regression maps of winter-mean (DJF 2000–2019) anomalies of zonal-mean zonal wind, modified potential vorticity and diabatic heating, regressed on the strength of the subtropical horizontal ozone gradients averaged between 30°N to 40°N and 340 K to 380 K (green boxes) for ERA5 (top row) and EMAC data (bottom row) used in Chapter 4. The stippling indicates where the linear regressions are not statistically significant at the 95 % level. The thick black dotted lines show the winter-mean WMO (1957) tropopause. 2-PVU isolines are provided by the thick blue lines. The thin black contours display the zonal-mean zonal wind climatology with 10 m s⁻¹ contour intervals.

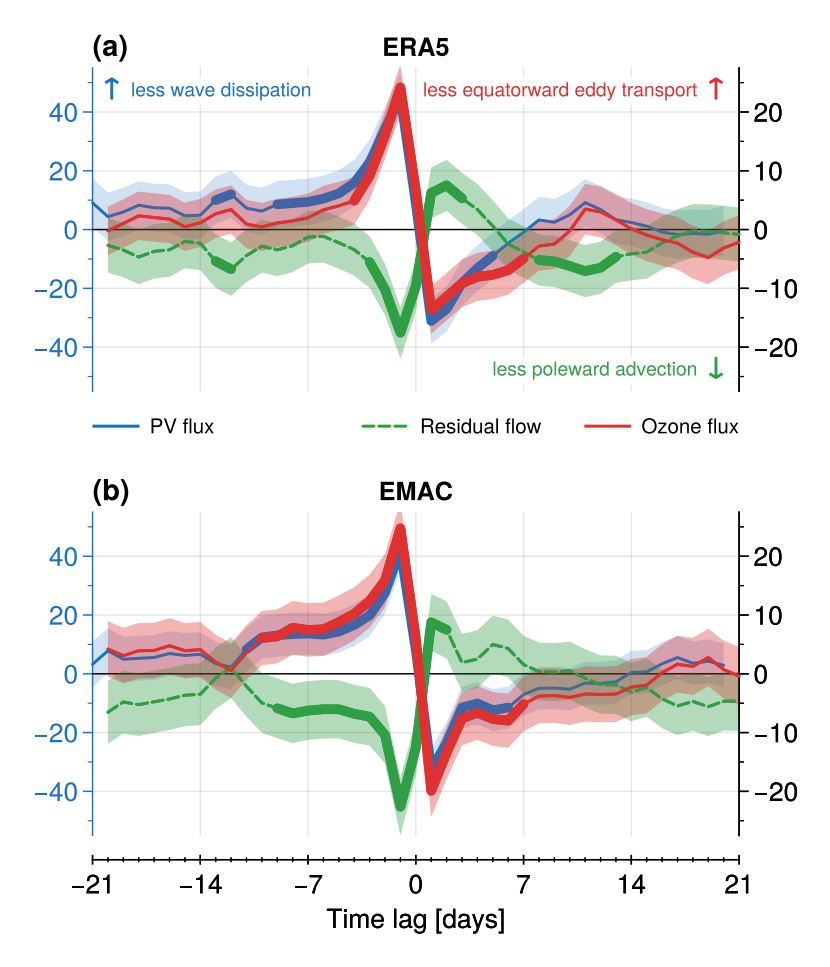


Figure 5.4: Linear regressions of daily-mean meridional potential vorticity (PV) fluxes, residual horizontal mean flow and meridional ozone fluxes on the strength of the subtropical horizontal ozone gradients, each averaged across the subtropical jet stream region between $30^{\circ}N$ to $40^{\circ}N$ and $340\,\mathrm{K}$ to $380\,\mathrm{K}$ (ERA5 and EMAC data as in paper III in Chapter 4, November–March, 2000-2019). Regression coefficients are given per index standard deviation in units of percent relative to the climatology in the subtropical jet stream region and as function of lag time between the regression time series, where positive lag times indicate that the predictands succeed the ozone gradient index (and vice versa for negative lag times). The color shadings provide the $95\,\%$ confidence intervals.

regressions based on daily data, which are provided in Fig. 5.4 (November–March, 2000–2019). Here, daily time series are computed by averaging the meridional eddy fluxes of potential vorticity (PV) and ozone, $\overline{\hat{v}\rho_{\theta}\hat{q}}/\overline{\rho_{\theta}}$ and $\overline{\hat{v}\rho_{\theta}\hat{\chi}}/\overline{\rho_{\theta}}$, respectively, as well as the residual horizontal mean flow \overline{v}^* (notation as in Chapter 4) between 30°N to 40°N and 340 K and 380 K as before (cf. green boxes in Fig. 5.3). Similarly, the subtropical ozone gradient index introduced above is now calculated on a daily basis. Figure 5.4 then displays the linear regression coefficients as a function of the lag between the predictands and this ozone gradient index, where positive lag times indicate that the responses succeed the index anomalies and vice versa for negative lag times. The three colored labels at the upper panel's vertical axes may help to interpret these responses relative to climatology.

The results obtained from ERA5 and EMAC are mostly similar and suggest the following mechanism:

- Reduced wave dissipation in the subtropics (as indicated by anomalously weak equatorward PV fluxes there, cf. blue curves in Fig. 5.3 at negative lag times) is associated with strengthening of the subtropical jet stream and, as a consequence, of the subtropical transport barrier.
- Simultaneously, this reduced wave activity leads to a weakening of the equatorward eddy ozone transport across the jet core (red curves in Fig. 5.3) and anomalously low poleward advection of ozone by the wave-driven residual mean flow (green curves) at negative lag times.
- As a result, due to this reduced cross-tropopause exchange of ozone, the horizontal ozone gradients in the subtropics become stronger several days later (i. e., at lag time zero).
- After that, for positive lag times, Fig. 5.4 clearly shows strong responses of opposite sign for all three predictands, which are substantially weaker than the anomalies for negative lag times, however. These may then represent feedbacks to the increased gradients of PV and ozone that lead to more effective cross-tropopause transport for a given amount of wave driving and ultimately support the re-balancing of the system (cf. Lorenz and Hartmann, 2003).

In conclusion, Fig. 5.4 showed that fluctuations of the subtropical gradients of the background ozone distribution are statistically preceded by synoptic events of anomalous wave activity, possibly of tropospheric origin, and corresponding changes of wave-induced ozone transport in the LMS. In addition, ozone gradient variations seem to feed back to the effectiveness of the individual transport processes, illustrating the essential physical mechanism of natural climate variability and the formation of mean states.

- Adam, O. et al. (2018). "The TropD software package (v1): standardized methods for calculating tropical-width diagnostics". In: *Geosci. Model Dev.* 11, pp. 4339–4357. DOI: 10.5194/gmd-11-4339-2018.
- Albers, J. R. et al. (2018). "Mechanisms governing interannual variability of stratosphere-to-troposphere ozone transport". In: *J. Geophys. Res.-Atmos.* 123, pp. 234–260. DOI: 10.1002/2017JD026890.
- Andrews, D. G. et al. (1983). "Eliassen-Palm Diagnostics of Wave-Mean Flow Interaction in the GFDL 'SKYHI' General Circulation Model". In: *J. Atmos. Sci.* 40, pp. 2768–2784. DOI: 10.1175/1520-0469(1983)040<2768:ETWATM>2.0.CO;2.
- Ball, W. T. et al. (2020). "Inconsistencies between chemistry-climate models and observed lower stratospheric ozone trends since 1998". In: *Atmos. Chem. Phys.* 20, pp. 9737–9752. DOI: 10.5194/acp-20-9737-2020.
- Benito-Barca, S. et al. (2025). "Recent Lower Stratospheric Ozone Trends in CCMI-2022 Models: Role of Natural Variability and Transport". In: *J. Geophys. Res.-Atmos.* 130. DOI: 10.1029/2024JD042412.
- Birner, T. (2024). "A subjective view on open issues in our understanding of the Brewer-Dobson circulation". Talk on March 14, 2024 at the TP-Challenges International Conference, Johannes Gutenberg University Mainz.
- Birner, T. and H. Bönisch (2011). "Residual circulation trajectories and transit times into the extratropical lowermost stratosphere". In: *Atmos. Chem. Phys.* 11, pp. 817–827. DOI: 10.5194/acp-11-817-2011.
- Bönisch, H. et al. (2011). "On the structural changes in the Brewer-Dobson circulation after 2000". In: Atmos. Chem. Phys. 11, pp. 3937–3948. DOI: 10.5194/acp-11-3937-2011.
- Brewer, A. W. (1949). "Evidence for a world circulation provided by the measurements of helium and water vapour distribution in the stratosphere". In: Q. J. Roy. Meteor. Soc. 75, pp. 351–363. DOI: 10.1002/qj.49707532603.

Butchart, N. (2014). "The Brewer-Dobson circulation". In: *Rev. Geophys.* 52, pp. 157–184. DOI: 10.1002/2013RG000448.

- CAMS (2022). Copernicus: Unusually persistent Antarctic ozone holes in 2020-2022. Copernicus Atmosphere Monitoring Service (CAMS), December 15, 2022. URL: https://atmosphere.copernicus.eu/copernicus-unusually-persistent-antarctic-ozone-holes-2020-2022 (visited on July 22, 2025).
- CAMS (2024). Copernicus: High temperatures trigger seasonal ozone pollution across Europe. Copernicus Atmosphere Monitoring Service (CAMS), July 30, 2024. URL: https://atmosphere.copernicus.eu/copernicus-high-temperatures-trigger-seasonal-ozone-pollution-across-europe (visited on July 22, 2025).
- CAMS (2025). CAMS monitors unusually low Arctic ozone levels during 2025. Copernicus Atmosphere Monitoring Service (CAMS), March 18, 2025. URL: https://atmosphere.copernicus.eu/cams-monitors-unusually-low-arctic-ozone-levels-during-2025 (visited on July 22, 2025).
- CCMI (2025). CCMI-2022 Data Archive. URL: https://blogs.reading.ac.uk/ccmi/ccmi-2022_archive/ (visited on July 22, 2025).
- Chapman, S. (1929). "A theory of upper-atmospheric ozone". In: Mem. R. Meteor. Soc. 3, pp. 103–125.
- Charney, J. G. and P. G. Drazin (1961). "Propagation of planetary-scale disturbances from the lower into the upper atmosphere". In: *J. Geophys. Res.* 66, pp. 83–109. DOI: 10.1029/JZ066i001p00083.
- Chiodo, G. et al. (2018). "The Response of the Ozone Layer to Quadrupled CO₂ Concentrations". In: *J. Climate* 31, pp. 3893–3907. DOI: 10.1175/JCLI-D-17-0492.1.
- Chiodo, G. and L. M. Polvani (2019). "The Response of the Ozone Layer to Quadrupled CO₂ Concentrations: Implications for Climate". In: *J. Climate* 32, pp. 7629–7642. DOI: 10.1175/JCLI-D-19-0086.1.
- Davis, L. L. B. (2021). *ProPlot.* DOI: 10.5281/zenodo.3873878.
- Desille, Y. (2022). "Atmospheric Dynamics and Climate Variability from Reanalyses". Internship Report. Ludwig-Maximilians-Universität München, Faculty of Physics, Munich, Germany.
- Dietmüller, S. et al. (2014). "Interactive ozone induces a negative feedback in CO₂-driven climate change simulations". In: *J. Geophys. Res.-Atmos.* 119, pp. 1796–1805. DOI: 10.1002/2013JD020575.
- Dietmüller, S. et al. (2021). "Analysis of recent lower-stratospheric ozone trends in chemistry climate models". In: *Atmos. Chem. Phys.* 21, pp. 6811–6837. DOI: 10.5194/acp-21-6811-2021.

Dobson, G. M. B. et al. (1929). "Measurements of the amount of ozone in the Earth's atmosphere and its relation to other geophysical conditions. – Part III". In: *P. R. Soc.* A 122, pp. 456–486. DOI: 10.1098/rspa.1929.0034.

- ESA (2023). Ozone hole goes large again. European Space Agency (ESA), October 4, 2023. URL: https://www.esa.int/Applications/Observing_the_Earth/Copernicus/Sentinel-5P/Ozone_hole_goes_large_again (visited on July 22, 2025).
- Eyring, V. et al. (2013). "Overview of IGAC/SPARC Chemistry-Climate Model Initiative (CCMI) community simulations in support of upcoming ozone and climate assessments". In: SPARC Newsletter No. 40, pp. 48-66. URL: https://www.aparc-climate.org/publications/newsletter/.
- Gettelman, A. et al. (2011). "The extratropical upper troposphere and lower stratosphere". In: *Rev. Geophys.* 49. DOI: 10.1029/2011RG000355.
- Harris, C. R. et al. (2020). "Array programming with NumPy". In: *Nature* 585, pp. 357–362. DOI: 10.1038/s41586-020-2649-2.
- Harzer, F. (2021). "Aspects of Climate Variability associated with Atmospheric Angular Momentum Transport". Master thesis. Ludwig-Maximilians-Universität München, Faculty of Physics, Munich, Germany.
- Haynes, P. H. et al. (1991). "On the 'Downward Control' of extratropical diabatic circulations by eddy-induced mean zonal forces". In: *J. Atmos. Sci.* 48, pp. 651–678. DOI: 10.1175/1520-0469(1991)048<0651:0TC0ED>2.0.C0;2.
- Holton, J. R. et al. (1995). "Stratosphere-troposphere exchange". In: *Rev. Geophys.* 33, pp. 403–439. DOI: 10.1029/95RG02097.
- Hoyer, S. and J. Hamman (2017). "xarray: N-D labeled Arrays and Datasets in Python". In: J. Open Res. Softw. 5. DOI: 10.5334/jors.148.
- Hufnagl, L. et al. (2023). "Stratospheric Ozone Changes Damp the CO₂-Induced Acceleration of the Brewer–Dobson Circulation". In: *J. Climate* 36, pp. 3305–3320. DOI: 10.1175/JCLI-D-22-0512.1.
- Hunter, J. D. (2007). "Matplotlib: A 2D Graphics Environment". In: *Comput. Sci. Eng.* 9, pp. 90–95. DOI: 10.1109/MCSE.2007.55.
- IFA (2025). Ozone. Institute for Occupational Safety and Health (IFA) of the German Social Accident Insurance. URL: https://gestis.dguv.de/data?name=004040&lang=en (visited on July 22, 2025).
- Lait, L. R. (1994). "An alternative form for potential vorticity". In: *J. Atmos. Sci.* 51, pp. 1754–1759. DOI: 10.1175/1520-0469(1994)051<1754:AAFFPV>2.0.CO; 2.
- Leith, C. E. (1975). "Climate Response and Fluctuation Dissipation". In: *J. Atmos. Sci.* 32, pp. 2022–2026. DOI: 10.1175/1520-0469(1975)032<2022:CRAFD>2.0.CO;2.

Lorenz, D. J. and D. L. Hartmann (2001). "Eddy–Zonal Flow Feedback in the Southern Hemisphere". In: *J. Atmos. Sci.* 58, pp. 3312–3327. DOI: 10.1175/1520-0469(2001) 058<3312:EZFFIT>2.0.C0; 2.

- Lorenz, D. J. and D. L. Hartmann (2003). "Eddy-Zonal Flow Feedback in the Northern Hemisphere Winter". In: *J. Climate* 16, pp. 1212–1227. DOI: 10.1175/1520-0442(2003)16<1212:EFFITN>2.0.CO;2.
- Mak, M. (2012). Atmospheric Dynamics. Cambridge University Press. DOI: 10.1017/CB09780511762031.
- Match, A. et al. (2025). "Protection without poison: why tropical ozone maximizes in the interior of the atmosphere". In: *Atmos. Chem. Phys.* 25, pp. 4349–4366. DOI: 10.5194/acp-25-4349-2025.
- Ming, A. (2022). PyTropD version 2.12. URL: https://github.com/TropD/pytropd.
- Morgenstern, O. et al. (2017). "Review of the global models used within phase 1 of the Chemistry-Climate Model Initiative (CCMI)". In: *Geosci. Model Dev.* 10, pp. 639–671. DOI: 10.5194/gmd-10-639-2017.
- NOAA (2020). Spring 2020 brings rare ozone "hole" to the Arctic. National Oceanic and Atmospheric Administration (NOAA) Climate.gov, April 21, 2020. URL: https://www.climate.gov/news-features/event-tracker/spring-2020-brings-rare-ozone-%E2%80%9Chole%E2%80%9D-arctic (visited on July 22, 2025).
- NOAA (2024). 2024 Antarctic ozone hole ranks 7th-smallest since recovery began. National Oceanic and Atmospheric Administration, October 30, 2024. URL: https://www.noaa.gov/news-release/2024-antarctic-ozone-hole-ranks-7th-smallest-since-recovery-began (visited on July 22, 2025).
- Nowack, P. J. et al. (2015). "A large ozone-circulation feedback and its implications for global warming assessments". In: *Nat. Clim. Change* 5, pp. 41–45. DOI: 10.1038/nclimate2451.
- Plumb, R. A. (2002). "Stratospheric transport". In: *J. Meteorol. Soc. Jpn. Ser. II* 80, pp. 793–809. DOI: 10.2151/jmsj.80.793.
- Plummer, D. et al. (2021). "CCMI-2022: A new set of Chemistry-Climate Model Initiative (CCMI) Community Simulations to Update the Assessment of Models and Support Upcoming Ozone Assessment Activities". In: SPARC Newsletter No. 57, pp. 22–30. URL: https://www.aparc-climate.org/publications/newsletter/.
- Rocklin, M. (2015). "Dask: Parallel Computation with Blocked algorithms and Task Scheduling". In: *SciPy Proceedings*, pp. 126–132. DOI: 10.25080/Majora-7b98e3ed-013.
- Salawitch, R. J. et al. (2023). Twenty Questions and Answers About the Ozone Layer: 2022 Update. Scientific Assessment of Ozone Depletion: 2022. World Meteorological

Organization, Geneva, Switzerland. URL: https://csl.noaa.gov/assessments/ozone/2022/downloads/twentyquestions.pdf.

- Thompson, D. W. J. et al. (2003). "Atmospheric Processes Governing the Northern Hemisphere Annular Mode/North Atlantic Oscillation". In: *The North Atlantic Oscillation: Climatic Significance and Environmental Impact.* Ed. by J. W. Hurrell et al. Vol. 134. Geophysical Monograph Series. American Geophysical Union, pp. 81–112. DOI: 10.1029/134GM05.
- Thompson, D. W. J. and J. M. Wallace (2000). "Annular Modes in the Extratropical Circulation. Part I: Month-to-Month Variability". In: *J. Climate* 13, pp. 1000–1016. DOI: 10.1175/1520-0442(2000)013<1000:AMITEC>2.0.CO;2.
- UNEP (2019). The Ozone Treaties. Ozone Secretariat of the United Nations Environment Programme. URL: https://ozone.unep.org/treaties/montreal-protocol (visited on July 22, 2025).
- UNEP (2023). Ozone layer recovery is on track, helping avoid global warming by 0.5°C. Press release, January 9, 2023. URL: https://www.unep.org/news-and-stories/press-release/ozone-layer-recovery-track-helping-avoid-global-warming-05degc (visited on July 22, 2025).
- Virtanen, P. et al. (2020). "SciPy 1.0: fundamental algorithms for scientific computing in Python". In: *Nat. Methods* 17, pp. 261–272. DOI: 10.1038/s41592-019-0686-2.
- Von Heydebrand, H. (2022). "Interannual Ozone Variability in the Northern Hemisphere from Coupled Chemistry-Climate Models". Bachelor thesis. Ludwig-Maximilians-Universität München, Faculty of Physics, Munich, Germany.
- WMO (1957). "Meteorology a three-dimensional science. Second session of the Commission for Aerology". In: WMO Bulletin 6, pp. 134–138.

Acknowledgments

First, I would like to thank Prof. Thomas Birner for the great opportunity to conduct a research project on exciting and fundamental questions in atmospheric physics. I wish to thank my two supervisors and mentors, Prof. Thomas Birner and Dr. Hella Garny, for their continuous support and advice, many in-depth discussions, new ideas, helpful suggestions and for their guidance during the last years.

Furthermore, I would like to thank my research collaborators, co-authors and the reviewers for their important contributions. I thank my colleagues from DFG's Collaborative Research Center 301, "The tropopause region in a changing atmosphere" (TPChange), for their helpful feedback, suggestions and motivating discussions. I very much appreciated many inspiring meetings and the broad range of activities for Early Career Researchers within the TPChange network. A big thanks also to all members of Prof. Birner's research group at LMU Munich and to my colleagues at the Meteorological Institute Munich for their support.

I would like to acknowledge the contributions by the many developers and members of the open-source community. The results of this thesis were obtained using the Python programming language together with various software extensions, e.g., among others, NumPy (Harris et al., 2020), SciPy (Virtanen et al., 2020), xarray (Hoyer and Hamman, 2017), dask (Rocklin, 2015), Matplotlib (Hunter, 2007) and ProPlot (Davis, 2021). Similarly, I would like to thank all the reanalysis data centers, climate model developers, measurement experts, members of the scientific community and colleagues for providing the data that the research for this project is based on.